Ida Wadseng

$IrNi_x$ Core-Shell Nanocatalysts for the Oxygen Evolution Reaction

Master's thesis in Chemistry
Supervisor: Svein Sunde, Karina Mathisen & Fatemeh Poureshghi
September 2019

Master's thesis

NTNU
Norwegian University of Science and Technology
Faculty of Natural Sciences
Department of Materials Science and Engineering

NTNU
Norwegian University of
Science and Technology

Ida Wadseng

$IrNi_x$ Core-Shell Nanocatalysts for the Oxygen Evolution Reaction

Master's thesis in Chemistry
Supervisor: Svein Sunde, Karina Mathisen & Fatemeh Poureshghi
September 2019

Norwegian University of Science and Technology
Faculty of Natural Sciences
Department of Materials Science and Engineering

NTNU
Norwegian University of
Science and Technology

Abstract

This thesis investigates different aspects regarding iridium oxide based electrocatalysts for the oxygen evolution reaction (OER), for usage in proton exchange membrane (PEM) water electrolysers. With today's ever growing demand for green energy, the production of hydrogen has never been more important. A major drawback for PEM electrolysers is the harsh acidic environment, sluggish rate of OER, requiring expensive catalysts. Bimetallic nanocatalysts with core-shell structures are of great interest because of advanced chemical and/or mechanical properties, and together with their large surface area they are able to achieve a higher catalytic activity per mass catalyst.

Thus, our aim for this thesis is to synthesise bimetallic core-shell nanocatalysts by colloidal metallic salt reduction, with the expensive iridium metal as the shell and crude metal nickel as the core. Two different one-pot synthesis procedures are used: a successive reduction procedure of nickel and iridium, and a co-reduction procedure followed by electrochemical dealloying. We investigate the effect of varying the nickel to iridium precursor molar ratio, in order to control the growth and achieve thermodynamic controlled core-shell structures, and we investigate the resulting changes in catalytic activity for OER. Furthermore, we will observe the effect of iridium growth by adding more of the capping agent tri-n-octylphophine (TOP), and the effect on the OER activity.

In this thesis we successfully synthesised core-shell nanoparticles from both iridium nickel synthesis routines, with a mass catalytic activity typically at $1.98\,\mathrm{A\,g_{Ir}^{-1}}$ at η =250 mV. Yielding a lower mass activity than today's best performing catalysts in the literature (our catalysts had a ten times higher surface area). By reducing the amount of iridium to nickel precursor, we were also able to achieve core-shell by co-reductive synthesis routine without dealloying. The particles synthesised by successive reduction followed a trend: OER mass activity increased with reduction of iridium to nickel precursor. This trend was not followed by the co-successive synthesised and we concluded, that this routine is harder to control to form segregated core-shell structures. Addition of TOP seemed to inhibit growth of iridium.

Sammendrag

Dette masterprosjektet undersøker flere aspekter av iridium baserte elektrokatalysatorer for okygenutviklingsreaksjonen (OER), i proton bytte membraner (PEM) for vannelektrolyse. Med dagens økende fokus på grønn energi, har det aldri vært et så stort behov for produksjon av hydrogen som det er i dag. En stor ulempe med PEM elektrolysøren er lav pH og treg reaksjonshastighet for OER, som krever dyre katalysatorer. Bimetalliske nanokatalysatoerer med kjerne-skall strukturer er derfor interessante å studere på grunn av deres forbedrede kjemiske og/eller mekaniske egenskaper. Med dette, sammen med stort overflateareal per volum for partiklene, er det mulig å oppnå høyere aktivitet per masse katalysator.

Målet med dette prosjektet er derfor å syntetisere bimetalliske kjerne-skall nanokatalysatorer ved kolloidal reduksjon av metalliske salter, med det dyre metallet iridium i skall-formasjon, og det billige metallet nikkel som kjerne. To forskjellige "alt-i-ett"-synteser blir brukt: en stegvis reduksjonsprosedyre av nikkel og iridium, og en co-reduksjonsprosedyre etterfulgt av elektrokjemisk avlegering. Vi undersøker effekten av å variere det molare forholdet mellom nikkel og iridium forløpere, i et forsøk på å kontrollere vekst og oppnå termodynamisk kontrollerte kjerne-skall strukturerer, og vi undersøker de resulterende endringene i katalytisk aktivitet for OER. I tillegg observerer vi effekten av iridiumvekst ved tilsats av surfaktanten tri-n-oktylfosfin (TOP), og effekten det har på OER aktivitet.

I dette prosjektet klarte vi å syntetisere kjerne-skall strukturene via begge syntesemetodene, med en typisk massebestemt aktivitet på $1.98\,\mathrm{A\,g_{Ir}^{-1}}$ ved $\eta = 250\,\mathrm{mV}$. Dette resulterte i en lavere massebestemt aktivitet med de sammenliknede standard rapporterte katalysatoerene (våre prøver var ti ganger så store). Ved å redusere mengde iridium mot nikkel så vi en trend i den stegvis-reduserte syntesen: massespesifikk aktivitet for OER økte. Denne trenden gjaldt ikke for co-reduserte syntesen, og vi konkluderte med at denne metoden er vanskeligere å kontrollere for syntese av segregerte kjerne-skallstrukturer. Tilsats av TOP så ut til å inhibere opptaket av iridium.

Acknowledgements

First of all, I would like to give my sincere gratitude to my supervisor, Professor Svein Sunde, for his excellent guidance and support in this project. Your pedagogical skills and enthusiasm have been invaluable for my work on this thesis, and a sincere thank you for all the discussions along the way, both on- and off-topic.

I would also express my gratitude to my co-supervisors, Associate Professor Karina Mathisen and PhD-candidate Fatemeh Poureshghi, with a special thanks to Fatemeh for willingly guiding and assisting me with the practical laboratory work.

Furthermore, I would like to thank the technical staff from Department of Material Science and Engineering for their assistance and support. With a special thanks to Senior Engineer Mathilde Isabelle Barriet at NTNU's nanolab for helping me with the Schlenk line set-up. I am also grateful for Post Doc. Maidhily Manikandan and PhD-candidate Kristian Thorbjørnsen's assistance and for helpful discussions.

I would also like to acknowledge support from the Research Council of Norway through the Norwegian Center for Transmission Electron Microscopy, NORTEM (197405/F50).

Finally, I would like to thank my family and friends that have been supporting me and pushing me throughout this work; with a deepest appreciation and gratitude to my mother, sister and partner Simon Birger Byremo Solberg.

Contents

1 Introduction

For the past two decades the interest in hydrogen as an energy carrier has increased eminently, as there is an ever increasing demand of green energy. Hydrogen is a environmentally friendly and non-toxic gas, with the highest gravimetric energy density of all known fuels of $143\,\mathrm{MJ\,kg^{-2}}$ (HHV).[1,2] However, as hydrogen can not be found abundantly in its molecular form naturally, it is not considered a primary energy source but as an energy carrier. Therefore, hydrogen must be generated before it can used as an energy source.[2]

One way to generate high purity hydrogen is by water electrolysis; a non-spontaneous electrochemical process, where water vapour($H_2O(g)$) is converted into hydrogen ($H_2(g)$) and oxygen ($O_2(g)$), made possible by applying a electric potential over the system. This process is typically carried out by an electrolyser, such as the commercial alkaline or proton exchange membrane (PEM) electrolyser. The first PEM electrolyser was made in 1960s by General Electrics, in order to overcome the many shortcomings of the alkaline electrolyser.[3] As a result of the PEM's compact system design, it is able to operate at much higher pressures, thus increasing cell performance and current densities. They also have a higher response rate and are able to yield purer hydrogen due to lower crossover rate throughout the compact electrolyte polymer membrane.[3]

Nonetheless, PEM-electrolysers have significant disadvantages, which have lead to only 4 % of the global hydrogen production being generated by electrolysis.[4] Due to the acidic corrosive environment, PEM-electrolysers have short stack lifetime ($<20\,000\,\mathrm{h}$) and demand electrocatalysts with high corrosion stability, while simultaneously being structurally stable at potentials up to $+1.8\,\mathrm{V/RHE}$. This is why such catalysts usually contain stable, but expensive, noble metals such as platinum (Pt), ruthenium (Ru) and/or iridium (Ir).[5]

In an acidic environment, the oxygen evolution reaction (OER) suffers from a sluggish reaction rat. This is one of the major drawbacks for PEM-electrolysers. As the OER consist of multiple steps, the overpotential is at $1.60\,\mathrm{V}$, while the equilibrium potential is at $1.23\,\mathrm{V}$.[6] Electrocatalysis is the study on how to enhance catalytic activity of electrochemical reactions. To increase the efficiency of an electrochemical cell, and consequently the electrolyser, reducing the system's overpotential is crucial. Study of elec-

trocatalysts is therefore important, as the overpotential is dependent on the nature of the electrode material.[7] Rutile metal oxide catalysts show better oxygen-evolving properties than their respective metal catalyst.[6] Transition metal oxides of rutile structure, such as ruthenium(II)oxide (RuO_2), iridium(II)oxide (IrO_2) and titanium(II)oxide (TiO_2) show the highest activity for OER in acidic media, and are therefore of great interest. Of those three RuO_2 shows the highest activity, with IrO_2 next in line. However, as RuO_2 has a lower stability than IrO_2, IrO_2 is in the long run more suitable as an electrocatalyst for OER.[8]

If the intention is to increase green production of hydrogen through electrolysis and make it a more commercially friendly process, then price is also of great concern. In order to increase the efficiency (lowering the overpotential) of the metal oxide catalyst for OER, and limit the scarce noble metal content (hence reduce price), synthesising mesoporous or nanosized catalysts is of great interest.[5] Advantages of nanostructured electrocatalysts (at least one dimension below 100×10^{-9} nm) are that large portions of the particles' atoms are surface atoms, giving large surface areas and active sites compared to the volume of the particles. Thus, reducing the amount of needed catalyst. Bimetallic nanoparticles, consist of two different metals with usually improved physical and/or chemical properties. An example of alternation in properties are seen in bimetallic core-shell structures, consisting of a metal at the surface and a transition metal as a core. A change in catalytic activity happens due to near surface strain effects, and change in d-band overlap between two different metals, induced by their lattice mismatches.[9]

Nanocatalysts with core-shell structures have lately been reported with higher catalytic activity for OER than previous benchmarked rutile structured IrO_2 and RhO_2.[5] Such architectures of electrocatalysts for OER are therefore of great interest.

1.1 Motivation

The aim of this thesis is to attempt to lower the noble metal content of iridium by synthesising bimetallic core-shell nano-structures, with crude metal nickel as core metal, by two different one-pot, metal colloidal synthesis methods. The first one is a two step, successive reduction of core and shell metals. Subsequently, the catalysts will be activated by electrochemical oxidation, resulting in a final $IrNi@IrO_2$ structure. The second synthesis routine will

consist of a one-step co-reduction of the precursors, which thereafter will be selectively segregated by electrochemically dealloying and oxidised. Hopefully also achieving a IrNi@IrO_2 structure.

Further on, based on Xia et al.'s[10] general understandings on how to control growth of colloidal metal nanocatalysts under vacuum, we will observe how this understanding applies to our bimetallic system, and what structural effects changing the molar ratios between precursors has. This will be done for both syntheses, and we will compare both results with each other. Other than the structural effects, we will be especially looking for how the molar ratios of iridium and nickel precursors will affect the catalytic activity for OER. We want to investigate the viability of Nong et al.'s[5] results; by reducing ratio of iridium precursor to nickel precursor a thinner shell will be formed, thus increasing the specific mass activity. The viability will be tested with a much simpler three component system, consisting of only the weak reducing and stabilising agent oleylamine (OAm), and the two metal precursors. With no capping and stabilising agents than OAm, of the bimetallic nanoparticles.

In the end we will see how reducing the amount of capping agent tri-n-octylphosphine (TOP) will affect the final structures of the particles and their activities. TOP is known to favour thermodynamic growth of nickel and is able to reduce the particle size noticeably by bonding strongly to the nickel surface.[10,11] We will therefore investigate if this induces better growth of iridium, or if TOP will inhibit the iridium because of steric hindrances and strongly bonded TOP-molecules on the nickel surface. To prevent possible full blockage of shell growth, we will keep a low molar ratio of TOP to OAm. The ratio will also be varied to see if there is any observable trends with varying amounts of TOP added.

2 Theory

The first part of theory will give gives a general introduction to the thermodynamics and kinetics of electrochemistry. Thereafter, theory about water electrolysis in acidic environment, and the technology used in this process will be presented. We will focus on the oxygen evolution reaction (OER), this topic will be covered in more detail compared to the hydrogen evolution reaction (HER).

Thereafter, general, as well as more specific, theory used to understand and interpret information regarding the syntheses done throughout this thesis, will be given in this chapter. Covering general nucleation and growth theory, and more specific theory about bimetallic systems.

2.1 Electrochemcial Thermodynamics and Kinetics

Electrochemistry is a branch of chemistry that studies how coupling effects between mass and charge transport in a system affect each other. Species that contribute directly to the chemical reactions, by changing their oxidation state, are called electroactive species.[12] Reactions, including changes in oxidation states, are called redox reactions. A general redox reaction can be seen in Eq. (1).

$$\mathrm{oO} + \mathrm{ne}^- \rightleftharpoons \mathrm{rR} \tag{1}$$

Capital letter "O" denotes oxidative state (more positively charged) and "R" is the reduced state. Lower case letters denote the respective species' stoichiometric value, and ne^- as n-amounts of electrons transferred per oxidised species. Due to Pauling's principle of electroneutrality, exchange of charge between two species must always give a net charge of zero, and a stable system.[13].

When the amount of electricity passed is proportional to the number of moles produced or consumed in an electrode reaction, the process is called a faradaic process.[13] However, processes such as adsorption/desorption can alter the potential by changing the electrode structure and electrolyte concentration without the charge-transfer reaction. This is called a nonfaradaic process. Both faradaic and nonfaradaic processes are governed by Faraday's law. When investigating electrode reactions faradaic current is usually the primary interest.[12]

The standard electrochemical potential, E^0, for a reaction can be expressed (Eq. (2)) by the change in standard Gibbs free energy, ΔG^0.

$$E^0 = \frac{\Delta G^0}{nF} = \frac{\Delta H^0 - T\Delta S^0}{nF} \tag{2}$$

Where F is the Faraday constant, n are the amount of transferred electrons in Eq. (1), ΔH^0 and ΔS^0 are the change in standard enthalpy and entropy, respectively, and T is the absolute temperature. The reversible potential, E_{rev}, i.e. the operational potential, for Eq. (1) can be expressed by the Nernst equation, Eq. (3). The expression yields under steady state:

$$E_{rev} = E^0 - \frac{RT}{nF} ln \frac{a_R^r}{a_O^o} \tag{3}$$

Where a_R and a_O are the activities of the reduced and oxidised species, respectively. Under reversible conditions E_{rev} is the minimum necessary cell voltage needed to reverse the spontaneous redox reaction, i.e. to achieve electrolysis, and is then equal to the cell voltage, E_{cell}. Under irreversible conditions, however, the voltage needed to reverse the reaction is greater than the minimum value. The excess voltage is named the overpotential, η. The cell voltage, E_{cell}, now becomes:

$$E_{cell} = E_{rev} + \sum_i \eta_i + jR_{cell} + jR_{circuit} \tag{4}$$

Where jR_{cell} and $jR_{circuit}$ are the ohmic overpotentials, and R_{cell} and $R_{circuit}$ are the resistances of the ionic conductor and the electronic conductor, respectively. The overpotentials are dependent on the net current density, j, and the ohmic overpotential is dependent on the electrode shape, size and morphology.[13,14] The sum of overpotentials, $\sum_i \eta_i$, can be expressed as:

$$\sum_i \eta_i = \eta_a + \eta_c = |\eta_{act,a}| + |\eta_{conc,a}| + |\eta_{act,c}| + |\eta_{conc,c}| \tag{5}$$

Where $\eta_{act,a}$ and $\eta_{act,c}$ are the activation overpotential at the anode (a) and the cathode (c), respectively. Slow reaction kinetics and charge-transfer limitations at the electrodes give rise to the activation overpotentials. η_{conc} is the concentration overpotential, and it is defined by the transport limitations (diffusion rates) between the electrodes and the electrolyte.[6]

Electrocatalytic reactions are combinations of several elementary reaction steps, in which the total reaction rate is determined by the rate determining step (rds), i.e. the slowest step.[13] These reactions are the main reason for the

overpotential, i.e. the deviation from theoretical standard potential,E^0.[6] The electrocatalytic activity and reaction mechanism for e.g. OER, can be found empirically by the anodic polarisation curves (plot j as a function of E) by Tafel analysis. Tafel analysis is carried out by acquiring the Tafel slope and using the Butler-Volmer equation to express the different parameters that control the relation between potential and current density of the slope.[15] The Tafel slope is expressed by Eq (6):

$$\eta = a + b\log(|j|) \tag{6}$$

Where η is the overpotential, i.e. the potential difference between the measured electrode potential, E, and E^0 ($\eta = E - E^0$), j is the current density and b is the Tafel slope. Furthermore, from the current density j, the overpotential can be expressed by the Butler-Volmer equation[15]:

$$j = j_0 \exp\left\{\frac{(1-\alpha)nF\eta}{RT}\right\} - \exp\left\{\frac{-\alpha nF\eta}{RT}\right\} \tag{7}$$

The first term describes the anodic current density, j_a, the second term is the cathodic current density, j_c, F is the Faraday constant, R the gas constant and T the temperature. The transfer coefficient, α, is usually equal to $\approx$0.5 for multi-step mechanisms in acidic environments, and n is stoichiometric number of transferred electrons in the rate determining step (rds).[13,15,16] The rate of the rds is indicated by the exchange current j_0, and j_0 is dependent on concentration (activity) of the electroactive specie and temperature.[13,16] At high cathodic overpotential, η_c, the contribution from the currents will be $j_c >> j_a$, and Eq. (7) can be simplified to:

$$j = j_c = -j_o \exp\left\{\frac{-\alpha nF\eta}{RT}\right\} \tag{8}$$

At high anodic overpotential, η_a, for a current: $j_c << j_a$, the anodic current can be expressed as:

$$j = j_a = j_o \exp\left\{\frac{(1-\alpha)nF\eta}{RT}\right\} \tag{9}$$

From Eqs. (8) and (9), the corresponding cathodic and anodic Tafel expressions can be derived, respectively (cf. Eq. (6)):

$$\eta_c = 2.303\left\{\frac{RT}{\alpha nF}\right\}\log_{10} j_0 - 2.303\left\{\frac{RT}{\alpha nF}\right\}\log_{10} j_a \tag{10}$$

$$\eta_a = -2.303\left\{\frac{RT}{(1-\alpha)nF}\right\}\log_{10} j_0 - 2.303\left\{\frac{RT}{(1-\alpha)nF}\right\}\log_{10} |j_c| \tag{11}$$

Taking OER as an example, the cathodic current can be excluded as a contribution for the anodic overvoltage. The Tafel expression for OER will therefore be equal to Eq. 11. The first term in Eq. 11 is equal to a in Eq. (6), and the second term is equal to $b\log(j_a)$. Empirically this expression can be found by doing linear sweep voltammetry (LSV), by plotting E as a function of $\log(|j|)$.

2.2 Electrochemical Methods

2.2.1 Normalising Electrochemical Measurements

Normalisation of electrocatalytical measurements is important for the comparison of catalytic activity between two different electrodes. Other than current density per mass of catalyst and per geometrical area; normalisation with respect to charge is important especially for porous and rough surfaces, as some of the active sites may be partially or fully blocked. Blocked active sites result in a deviation between the accessible, real catalytic surface from the geometrical one.[14]

To measure accessible active sites that are able to exchange protons with the solution, separation of the active and inactive surface must be done. As stated by Ardizzone *et al.*[17], the total surface charge, q_T^*, is equal to the sum of the inner and less accessible surface, q_i^*, and the easily accessible surface q_s^*, and is given by Eq. (12):

$$q_T^* = q_i^* + q_s^* \tag{12}$$

The outer surface charge q_s^*, can be found by integrating cyclic voltammograms (CV) with varied sweep rates (ν), and plotting the resulting charge, q^*, as a function of $1/\sqrt{\nu}$. By extrapolating this curve to infinity ($\nu \to \infty$) the outer surface charge is found. Total surface charge q_T^* is found by plotting $1/q*$ as a function of $\sqrt{\nu}$ and extrapolating the curve to zero sweep rate ($\nu \to 0$). Both plots should result in straight lines. After finding the outer and total surface, the inner surface q_i^*, can be found by rearranging Eq. (12).

The dependency of charge on sweep rate is related to the diffusion of reactants to the electrodes.[13,17,18] The dependency is also due to Faradaic processes such as adsorption/desorption and charging of the double layer.[19] Different values for the charge activity can therefore indicate differences in surface

morphology.[18] The electrochemically active surface area (ECSA) is an important feature, as nanocatalysts might have up to 1000 times greater active area compared to the geometrical one. With q_s^* and normalised polarisation curves with regards to mass catalyst and charge, ECSA at a given potential can be found. Other methods are e.g. finding area by Brunauer–Emmett–Teller (BET) analysis and dividing it by the q_s^* found in the hydrogen region in a CV. This value is for Ir equal to $218\,\mu C\,cm^{-2}$.[18]

2.2.2 Electrochemical Dealloying

Electrochemical deallyoing is a corrosion process where metals are selectively separated from each other in an alloy.[7,20] Such a process can be applied as a post treatment and synthesis method for catalysts to reconstruct the particles' architecture, and possibly improve the catalytic activity and stability.[9,21] This change can be from for example homogeneously mixed bimetallic alloy NPs into core-shell structured NPs. The dealloying process includes chemisorption of carbon monoxide (CO) by covalent bonding, which can work as a capping agent and reduce surface area, while metals are segregated during electrochemical cycling (CV). Because chemisorption might happen at specific facets, the final form of the particles will deviate from the predicted morphology and Wullf-shape[10]. The electrochemical dealloying process is size dependent, where leaching of the structures through for example Kirkendall effect can form pores and rough surfaces.[9,20,22] These effects are increased with increasing particle surface area.[22]

2.3 PEM Water Electrolysis

The proton exchange membrane electrolyser, or PEM electrolyser for short, consists of several stacked membrane-electrode assemblies that are connected by current collectors. The gas diffusion layers transport water (reactant) and the produced gases. They must be stable through out the whole operation. The solid proton exchange membrane (PEM) and its fluid content act as the electrolyte.[23] General operating principle for a single PEM-cell is shown in Fig. 1:

Frequently used membranes consist of perfluorosulfonic acid polymer, Nafion®. Because Nafion®is in solid form, it is possible to make thin films of the electrolyte. This leads to lower Ohmic losses, and makes the PEM fuel cells

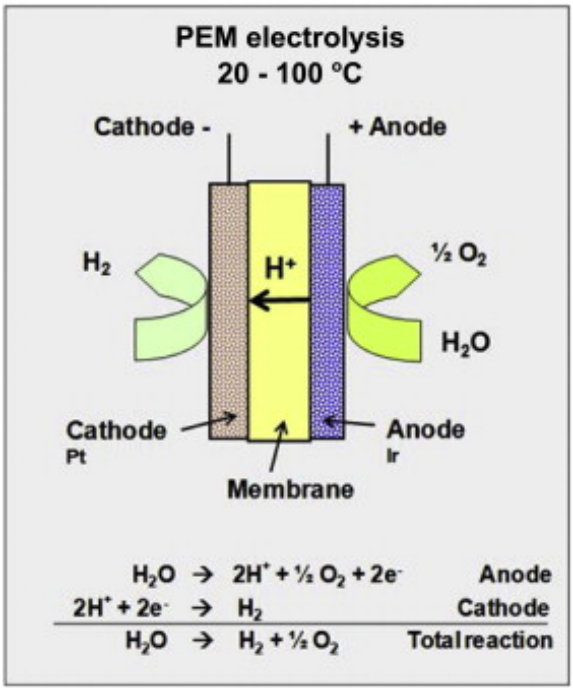

Figure 1: Schematic overview of operating principle for PEM electrolyser. Reprinted with permission from Carmo *et al.*[3]. Copyright©2013 Hydrogen Energy Publications, LLC.

able to reach a current density above $2\,\mathrm{A\,cm^{-2}}$.[23] Due to the thin solid membrane and the small fluid content in the membrane matrix, a higher stability is also achieved. Thus the electrolyser can operate at much higher pressures (150 bar), which gives the high crossover rate and much purer products[3] Furthermore, because of the thin membranes the PEM electrolyser can achieve more compact form than the alkaline electrolyser, and is more resilient against fluctuating currents. This makes PEM electrolysers (in theory) excellent for usage in the grid.

Still, the main drawback of the PEM electrolyser is the limited choice of anodic electrocatalysts. With a working condition at around pH$\sim$2 the anodic catalyst material consists of either Rh, Pt and/or Ir.[3] Thus leaving the membrane alone responsible for 24 % of the overall cost. Pt is most common used cathodic catalyst.[23] In an acidic environment the water-splitting reaction is described as:[6]

$$\mathrm{H_2O} \rightarrow \frac{1}{2}\mathrm{O_2} + \mathrm{H_2} \tag{13}$$

With the half-reactions equal to:[24]

$$2\,H^+ + 2\,e^- \rightarrow H_2 \tag{14}$$

$$2\,H_2O \rightarrow O_2 + 4\,H^+ + 4\,e^- \tag{15}$$

The first half-reaction Eq. 14 is the hydrogen evolution reaction (HER), and the second Eq. 15, is the oxygen evolution reaction (OER). Both reactions will be described in the two next following sections.

2.3.1 Hydrogen Evolution Reaction (HER)

Choosing a catalyst for the hydrogen evolution reaction (HER) depends on what type of electrolyser that is going to be used. For an alkaline electrolyser crude metals such as Ni and Co can be used, in the form of their oxides or halides. Today's benchmarked HER catalyst for PEM electrolysis is highly dispersed carbon supported Pt. There has been slightly increased interest in Pd based catalysts as well.[23]

There have been proposed different reaction mechanism steps for HER (half reaction Eq. 14), and for Pt surfaces in acidic solution the mechanism is:[7]

$$M + H_3O^+ + e^- \rightarrow M{-}H_{ads} + H_2O(l) \tag{16}$$

$$2\,M{-}H_{ads} \rightarrow 2\,M + H_2(g) \tag{17}$$

The first step Eq. (16), is fast discharge, and the following is a recombination step, which is the rds, in Eq. (17). Standard potential (E^0) for HER in acidic solution is defined as 0.0 V.

2.3.2 Oxygen Evolution Reaction (OER)

The standard potential (E^0) for OER in acidic solution is equal to 1.23 V, and is described by the anodic half reaction, previously stated in Eq. 15 in Section 2.3. Compared to HER, OER is slow due to sluggish multi-step elemental reaction mechanisms, confined to the electrode surface. Mechanism steps that include electron transfer influence the total overpotential, in which the rate determining step (rds) determines maximum value of η. Under acidic conditions and by assuming $\alpha = 0.5$, the different mechanisms steps for OER

are proposed to be:[6,25]

$$2\,H_2O(l) \underset{k_{-1}}{\overset{k_1}{\rightleftharpoons}} HO_{ad} + H^+(aq) + e^- \qquad \infty\,mV \qquad (18)$$

$$OH_{ad} \underset{k_{-2}}{\overset{k_2}{\rightleftharpoons}} O_{ad} + H^+(aq) + e^- \qquad 118.3\,mV \qquad (19)$$

$$O_{ad} + H_2O(l) \underset{k_{-3}}{\overset{k_3}{\rightleftharpoons}} OOH_{ad} + H^+(aq) + e^- \qquad 59.1\,mV \qquad (20)$$

$$OOH_{ad} \underset{k_{-4}}{\overset{k_4}{\rightleftharpoons}} (O_2)_{ad} + H^+(aq) + e^- \qquad 39.4\,mV \qquad (21)$$

$$(O_2)_{ad} \underset{k_{-5}}{\overset{k_5}{\rightleftharpoons}} O_2(g) \qquad 29.6\,mV \qquad (22)$$

The rate constants are denoted k_i and the subscript "ad" denotes an adsorbed species. Each mechanism step, Eqs. (18)-(22), can be related to a potential value per dec of the Tafel slope.[24,25] Rutile structured IrO_2 is known to have a Tafel slope around 40-60 $mV\,dec^{-1}$, and the proposed mechanism for the rds is equal to Eq. 20; where the OOH_{ad}-adsorbate is formed.[6,26]

Ruthenium oxides (RhO_2) also have the same rds and lie around the same value for Tafel. Despite that, RhO_2 still has a greater activity for OER with a lower overpotential than IrO_2. This is due to the fact that comparing Tafel slope with reaction mechanisms only takes thermodynamic considerations of the mechanisms. Activity of electrocatalysts is also determined by bond strength between adsorbed species and the surface of the catalyst, and the stability of the adsorbate.[6] Because IrO_2 bonds too strongly to adsorbed species compared to slightly weakly bonded RhO_2, RhO_2 ends up with a higher activity than IrO_2. The number of active sites is also important, thus a greater surface area may be necessary to increase the activity further.[27]

Relation between activity and binding energy can be described by a volcano plot. The volcano plot gives a linear relation between adsorbed species and metallic adsorbate and their binding energy, leaving a shape similar to a "volcano". Fig. 2 shows volcano plots, where horizontal dashed line represents E^0 (theoretical standard potential), and the difference from that line in y-direction, is equal to η. From the figure it can be seen that rutile structured RuO_2 has the highest activity for OER by being closest to E^0, i.e. the lowest overpotential, compared to IrO_2. For rutile structured IrO_2 the facet that yields the highest activity is {110}.

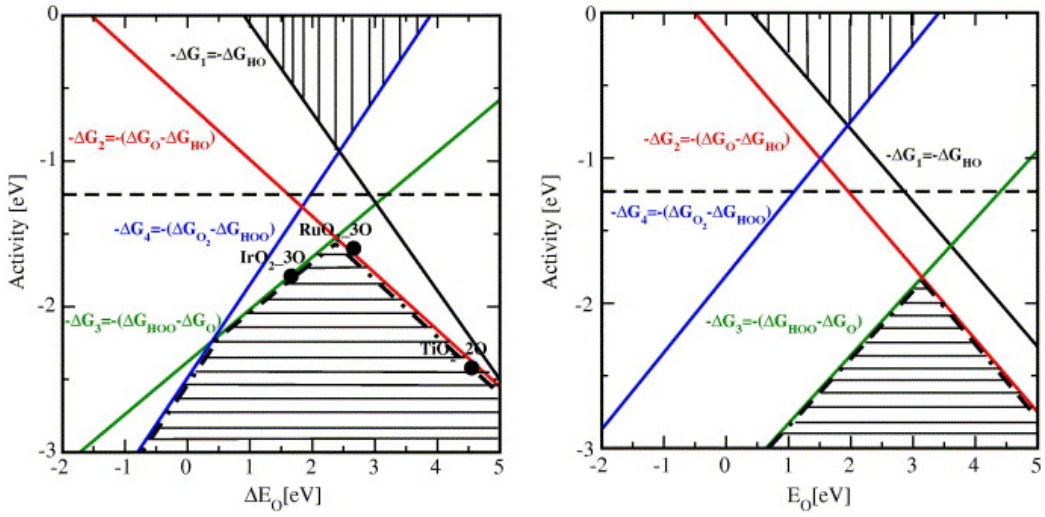

Figure 2: Volcano plot of RhO_2, IrO_2 and TiO_2. Showing the relation between theoretical activity for the four charge transferring steps (mechanisms) for OER, and the binding energies for the adsorbates at the respective metal surface. This figure is taken with permission from Rossmeisl *et al.*.[6] Copyright©2006 Elsevier B.V. All rights reserved.

2.4 Synthesis of Colloidal Metallic Nanoparticles

Nanotechnology is the study of how to fabricate, design and utilise nanomaterials; i.e. materials with at least one dimension on the nanoscale (below 100 nm). One nanometer (nm) is equal to 1×10^{-9} m. Nanomaterials (NMs) are divided into three categories, depending on how many spatial dimensions that are below 100 nm. Zero-dimensional (0D) NMs are either NPs or quantum dots, and all spatial dimensions are below 100 nm. Following the same logic, one-dimensional (1D) and two-dimensional (2D) materials will therefore have only 2 dimensions and 1 dimension below this threshold, while three-dimensional (3D) NMs have no spatial dimensions below 100 nm.[28]

There are two main approaches for designing NMs, referred to as the top-down and the bottom-up approach. Top-down approach (TD) builds NMs and NPs by starting out with a bulk material and tuning it down to nanoscale size. This is done by physical or lithographic methods. Attrition and milling are examples of two physical methods. Lithography by etching is a TD-approach where nanostructures are formed chemically by manipulating and breaking down structures with acid, alkaline solutions etc.[28] Bottom-up approach (BU) is the opposite of the TD-approach. As the name implies, NPs

and NMs are grown from seeds (nuclei) to particles and finally a final product.[28] Nuclei are typically referred to as seeds. The BU-approach consists of numerous different methods, such as colloidal-chemical synthesis, seed mediated growth by thermal reduction, template-based electrochemical synthesis, sol-gel synthesis, hydrolysis etc.[29] BU-approach is easier to control than the TD-approach especially for designing small 0D and 1D NPs and NMs, as it is easier to control different parameters and observe their impact on the system.[28]

Synthesising metal nanoparticles (MNPs) and their respective metal oxide nanoparticles (MONPs) is typically done by the BU-approach. In which MNPs are often formed by thermal reduction in colloidal dispersions, and MONPs by hydrolysis or by oxidising the already formed MNPs. While BU is a better approach than TD for building 0D NPs, controlling morphology and size distribution is still difficult. Because of this, designing MNPs, and especially those with more complicated structures (bimetallic NPs, core-shell structures) are thus still called "Mix and try approaches".[10,29,30]

2.4.1 Homogeneous and Heterogeneous Nucleation

Synthesising metallic 0D NPs is possible by thermal reduction of respective dissolved metal salts in either a aqueous or non-aqueous solution, together with a reducing agent and one or more stabilising agents. To nucleate and grow particles, one must first obtain supersaturated conditions (SS) for the reduced metal (ions), such that nucleation is possible. The process is named homogeneous nucleation, as stable seeds are formed spontaneously in the mother-phase (e.g. solvent). Heterogeneous nucleation occurs when nuclei are formed on a substrate of a different phase than the mother-phase, for instance seed-mediated growth.

Based on classical nucleation theory (CNT), at metastable SS-condition the system will always try to reduce total Gibbs free energy of the system (ΔG). For a general particle with a given geometry, ΔG, can be described as:

$$\begin{aligned} \Delta G &= -V|\Delta G_V| + \Delta G_s \\ &= -V|\Delta G_V| + A\gamma \end{aligned} \tag{23}$$

The first part of Eq. (23) represents the absolute value of volume free energy, ΔG_V, multiplied with the particle's volume, V. This term is always negative. By increasing the volume of a particle, the particle stabilises. The second

term is the surface free energy, ΔG_s, and is equal to area, A, of the particle multiplied its surface tension, γ. ΔG_s gives positive change in ΔG, as making a new interface demands energy.[28] The term ΔG_V can also be described as the affinity per unit volume, which is equal to difference in volume chemical potential, $\Delta\mu_V$:

$$\Delta G_V = \Delta\mu_V = \frac{k_B T(\ln(a/a^*)^V)}{V_m} = \frac{k_B T \ln S^V}{V_m} \tag{24}$$

Where k_B is the Boltzmann constant, T is the absolute temperature, V_m is the molar volume, S is the degree of SS, a is total activity of the active species, and a^* is the critical activity. The total activity is defined as $a = c * \gamma$, where γ is the activity coefficient. Some of the main driving forces of nucleation are therefore concentration, c, temperature, T, and surface tension, γ.[28,31]

Homogeneous nucleation

For a primary homogeneous reaction, the maximum value of the total free energy (ΔG^*_{hom}) is equal to the activation energy barrier which needs to be overcome for nucleation to occur. For instance, using Eq. (23) with the volume and surface area for spherical shaped particles, V and A, gives:

$$\Delta G = \frac{4}{3}\pi r^3 \Delta G_V + 4\pi r^2 \gamma \tag{25}$$

To find ΔG^*_{hom}, one can see that ΔG is dependent on the radius. This means that ΔG^*_{hom} is dependent on a critical radius with $r > r^*$ to achieve formation of stable nuclei. ΔG^*_{hom} and r^* can be found by solving Eq. (25) for $d\Delta G/dr = 0$, giving Eqs. (26) and (27), respectively:

$$\Delta G^*_{hom} = \frac{16\pi\gamma}{3(|\Delta G_V|)^2} \tag{26}$$

$$r^* = \frac{-2\gamma}{|\Delta G_V|} = \frac{2\gamma V_m}{|k_B T \ln S|} \tag{27}$$

where r^* is the smallest achievable radius of a stable nucleus. Below this value it will dissolve, increase the concentration, and reducing ΔG.[31] Growth occurs simultaneously as nucleation, and as long as the concentration stays above the critical concentration (ΔG^*_{hom}) both processes will compete with each other. When the concentration goes below this threshold, but the system is still in SS-condition, only growth will happen because $r < r^*$. A

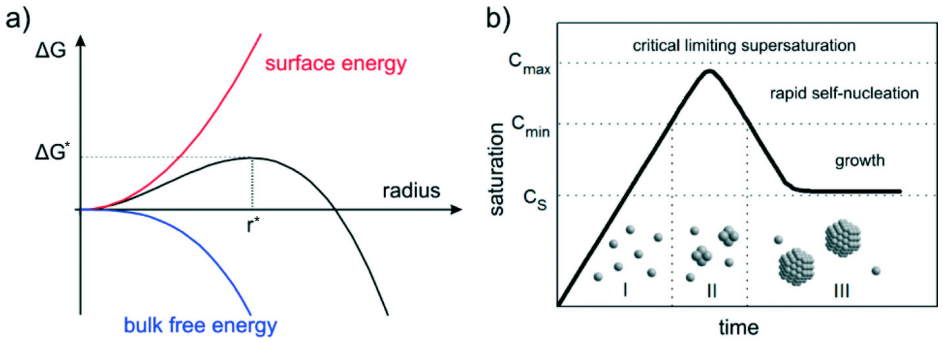

Figure 3: Schematic illustration of a) Nucleation and its dependence of ΔG versus the nuclei radius. With bulk free energy equal to volume free energy, ΔG_V. Red line is the surface free energy, ΔG_s. The critical free energy and radius is given by, ΔG^* and r^*. b) Shows different stages of nucleation and growth, and the relation between these processes with concentration and time. (Adapted with minor changes and permission from Ref.[30] Copyright © 1995 Published by Elsevier B.V..

schematic illustration of the relation between nucleation and growth can be seen in Fig. 3a.

In Fig. 3b the different stages of nucleation and growth are presented schematically in terms of solute concentration as a function of time. In intervals I and II SS-conditions are met and both nucleation and growth occur. In the very beginning of I nucleation is favoured, while in II both processes will compete. In interval III, growth is the only process happening, as $\Delta G < \Delta G^*$. With nuclei present different growth processes may occur.[28]

Heterogeneous nucleation

Heterogeneous nucleation demands less energy to happen than homogeneous nucleation because of an already existing surface to nucleate on. This process can be described by:

$$\Delta G^*_{het} = \phi \Delta G^*_{hom} \tag{28}$$

Where the variable ϕ is the wetting factor, which is dependent on the contact angle, θ, between the nucleus and the surface of the foreign substrate. The wetting factor is defined as:

$$\phi = \frac{(2 + cos\theta)(1 - cos\theta)^2}{4} \tag{29}$$

Good wetting results in a favourable nucleus-surface interaction, and occurs if $\phi < 1$ and $\theta < 90°$. Poor interaction happens with angles above 90°, however nucleation might occur. An angle of $\theta = 180°$ results in $\phi = 1$, thus nucleation does not happen.[31] Control of nucleation processes is important for the final morphology of the particles, as nucleation may have a large impact on the later growth processes. These growth modes can also be described by Young's equation.[28]

2.4.2 Thermodynamic and Kinetic Controlled Growth

The difference between thermodynamic and kinetic products is that thermodynamic favoured products have higher activation energy, E_a, but achieve the largest reduction of ΔG (lowest local minima). The result is a more stable final product. The relation between reaction rate r, and E_a can be expressed by the Arrhenius equation:

$$r = Ae^{-E_a/RT} \tag{30}$$

With A as pre-exponential factor that depends on collisions between particles, R as the universal gas constant and T as the absolute temperature. The easiest way to adjust between thermodynamic and kinetic growth mechanisms is by changing the temperature. Meaning, lowering the solution temperature favours kinetic products, while high solution temperature favours thermodynamic products.[28] On the other hand, there are other factors that depends on temperature, such as the surface tension (γ), diffusion etc.

For thermodynamic controlled growth, only the final products are in focus. The shapes of the thermodynamic products are called an "equilibrium state", which give the highest possible surface area (SA) and thus lowest possible ΔG.[10] Kinetic and thermodynamic growth are distinguished by the ratio between volume of atoms deposited (V_{depo}) at the surface and the volume of atoms diffusing (V_{diff}) to the surface. With $V_{depo}/V_{diff} << 1$ thermodynamic growth is favoured, whilst $V_{depo}/V_{diff} >> 1$ gives kinetic control. Values close to unity lead to competition between both processes.[10,31] For kinetic growth, the ratio means that there is a high influx of seeds to the surface, which gives the possibility of placing themselves at sites which have lower activation barriers. Kinetic growth of MNPs means that kinks, corners and edges are favoured instead of crystal faces of the particles. At rapid and uncontrolled growth dendrites may start to form. Leaving indistinctive and branched structures.[28]

Other important factors that can be tuned to change between the two types of products and control certain growth mechanisms are for example: pressure, stoichiometry, altering surface adsorption of chemical species by adding capping and/or stabilising agents, reaction time, addition rate of precursors, pH etc.[10]

Growth Mechanisms

General growth mechanisms for synthesising (metal) NPs are coalescence, Ostwald ripening, digestive ripening and agglomeeration. Coalescence is the process of smaller particles merging into bigger particles.[30] Ostwald ripening happens due to change of solubility of the growing particles, where bigger particles grows in expense of smaller particles. Digestive ripening is the opposite of this mechanism, where bigger particles redissolves into smaller particles.[31] For syntheses of MNPs below 500 K Ostwald ripening is unlikely to occur, as most metals have melting points above 500 K. In syntheses at high temperatures, such as thermal colloidal reduction reactions, Ostwald ripening is more likely to occur.[30]

Agglomeration is an effect of the high surface energy γ, of NPs. Due to small distances between NPs in the highly SS system, the attractive Van der Waals forces between the particles and Brownian motions gives a high possibility of agglomeration. This reduces the surface tension and SA. By stabilising the particles with a capping and/or stabilising agent unwanted growth can be prevented.[28,30]

Capping and stabilising Agent

Capping agents will chemisorb at specific crystal facets and prevent further deposition of atoms on unwanted facets.[10] The favoured facets grow as the capping agent exhibits a lower specific surface energy and therefore stabilise the particle, increasing the growth on facets not occupied by the capping agent. Facets that include the capping agents grow at a much lower rate due to the inhibiting nature of the capping agent by hindering access to the facet. Different types of capping agents exist such as different gas molecules O_2, CO etc., ions (Br^-) and organic molecules (PVP = polyvinylpyrrolidone, PVA = polyvinyl alcohol, micelles, tri-phenyl phosphine (TOP)).[28]

Some problems regarding capping agents and thermodynamic control is the fact that there have not been reported any capping agents which favour high-index sites. Facets with low coordination numbers and high density are often sites with the best catalytic performance.[10] They might also have some limitations for certain facets and particle size. Furthermore, removing the capping agent from particle surfaces can be troublesome, as they may be too strongly bonded to the particle. This can ruin the surface and in worst case degrade/reduce activity of the catalysts.[9] Capping agents can serve as stabilising agents, and stabilising agents can work as a capping agents.

Particle size is not necessarily only defined by the thermodynamic control, but also the colloidal stability. In other words the final size of particles depends heavily on how well the particles are stabilised.[30] To stabilise the particles a steric, electrostatic or electrosteric stabiliser can be used. A steric stabiliser usually consists of big, bulky molecules that adsorb at the particle surface and restrict the motions of the particle and prevent deposition at the surface. These can consist of capping agents or polymers such as PVP, Oleylamine (OAm), tri-phenyl phosphine (TOP) etc.[30] Some steric stabilisers simultaneously also serve as an electrostatic stabiliser, as they counter Van der Waals forces between the particles by repulse it with opposite Coulomb forces at the particle surface (electric double-layer). Such stabilisers are called electrosteric stabilisers, and an example is OAm.[28]

Altering the solvent's pH is a good way to increase/decrease the electrostatic stabilisation of a colloidal solution, by increasing/decreasing amount of positive or negative charges. However, for MNPs synthesis the pH is important because some metals are prone to oxidation, such as Ni. Change in polarity might therefore be a better option, to also prevent unwanted oxidation. Other factors to consider when choosing a stabilising and/or capping agent are how strongly chemisorbed the additives are at the particles surface. The capping agent may inhibit further growth, or deactivate the catalyst due to difficulties of removing the additives. As the adsorbed additive might block the active sites for the catalysis. Nevertheless, poor stabilisation results in bigger particles, broader size distribution and poor control of morphology.[30]

Reducing agent

Synthesising MNPs is usually done by reduction of metal precursors in a colloidal dispersion. There will therefore be a competition between the rate of reduction and the nucleation process. A strong reducing agent gives a high

rate of reduction, and thus a high value of V_{diff} due to the formation of a lot of seeds in a short amount of time. This gives a broad size distribution due to higher possibility and rate of coalescence.[30] The kinetically formed particles will therefore have a broad size distribution and fairly large particles compared to the thermodynamic counterpart.[30,31] Yet, sometimes a strong reducing agent is necessary to achieve reduction of precursors, especially if the system has a low maximum temperature.

Which mechanism dominates and what type of reducing agent that should be used varies between synthesis routes. In practice, choosing a reducing agent is done through a "mix and match" approach.[10,30] One strong reducing agent that is often used for colloidal colloidal reduction is $NaBH_4$. Other examples are sodium citrate, OAm, CO, hydrogen peroxide H_2O_2.[28]

Thermodynamic and kinetic control for Metallic Nanoparticles

Metal nanoparticles (MNPs) and their respective metal oxide nanoparticles (MONPs) do not favour spherical geometry as their equilibrium shape. This is because of their crystal structures which have facets with different surface energies (γ), resulting in growth at different rates for the various facets (anisotropic growth). Gibbs-Wulffs theorem can predict the equilibrium crystal shape by the fact that the system tries to achieve lowest ΔG as possible[29]. Growth at preferred crystal planes: those with lowest surface energies ($\gamma_{\{hkl\}}$, $\{hkl\}$ = Miller indices) at a given constant volume[32].

Deviation from spherical geometry alters a nanocatalyst's properties. Therefore, it is important to control the growth process, as catalytic selectivity and activity may be more or less active at certain facets.[5,29,33] One example that has been reported by Stamencovic *et al.* was that the activity for the bimetallic alloy nanocatalyst Pr_3Ni with an octahedral shape and {111} facets achieved over 50 times higher activity for ORR than cubic ones with {100} facets.[10,34]

To obtain a different morphology the growth rate must be controlled. Metals with face centred cubic (fcc) crystal structures such as Pt, Ir and Ni (Ni favours fcc at T >240 °C)[35], favour low crystallographic indexes in order of: $\gamma_{\{111\}} < \gamma_{\{100\}} < \gamma_{\{110\}}$. For these metals, if synthesised in vacuum, either octahedral or tetrahedral shapes with {111} facets can be expected based on that they yield lowest possible γ.[10,29] Nevertheless, both shapes give a higher value for ΔG_s (Eq. (27)) compared to a cubic shaped particles of {100}. As

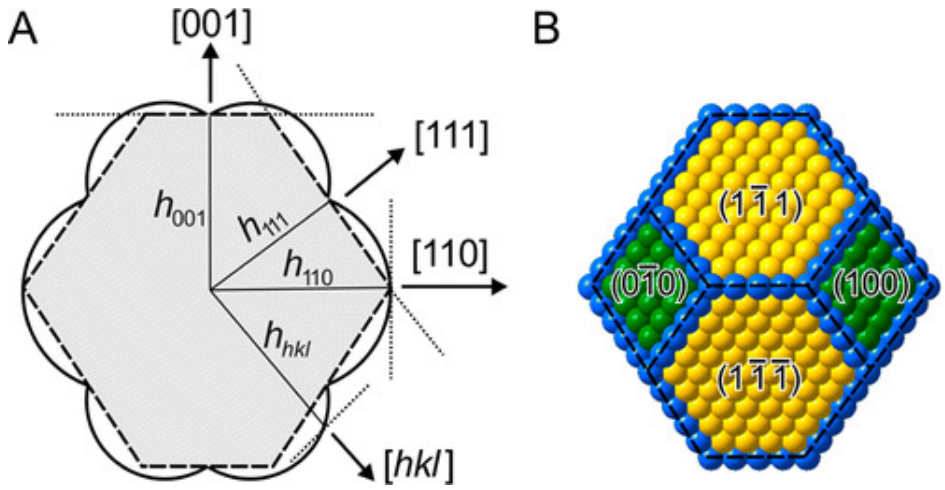

Figure 4: a) Derived with Wullf theorem a 2D polar-plot of ΔG_s for different directions in $[1\bar{1}0]$ plane. b) 3D atomic model of "hybrid" shape in a). Figure taken with permission from Xia *et al.*.[10]Copyright©2015, American Chemical Society

a result, the equilibrium shape of fcc structured NPs will be a "hybrid" form of those three shapes and two facets. An illustration of this "hybrid" shape can be seen in Fig. 4.

Ratios of the different areas in Fig. 4b will slightly vary for different metals. The "hybrid" shape shown in the figure is called a trunoctahedron and is the closest to a spherical shaped particle that can be achieved. This shape gives the lowest possible ΔG and highest possible SA for particles synthesised under vacuum and thermodynamic favoured growth. For very small nanosized particles the thermodynamic favourable form will be a octahedron because of vanishing {100} surface.[29]

Thermodynamic Shape for Rutile Structured IrO_2

The facet with highest activity for rutile structured IrO_2 is the {110} surface. This facet is dominating under thermodynamic controlled conditions during synthesis, when anisotropic growth favours direction [112] and [001]. The resulting shape is rod-like or needle-like shapes.[27]

2.5 Bimetallic Core-Shell Nanoparticles

Catalysts and electrocatalysts that consist of two or more different metals often exhibit better chemical and physical properties than catalysts of one metal.[36] With more than one type of metal, morphology and stability of surfaces are important. Especially so because post-synthesis work (such as dealloying and annealing) and harsh environmental effects (pH) can alter both electronic and chemical surface properties of the catalyst drastically.[37,38] Bimetallic NPs are usually formed by either co-reduction or successive reduction of metallic salts in colloidal dispersion. Co-reduction is a one-step reduction of precursors which are added together in one-go, whilst successive reduction is a two-step synthesis route where the precursors are added at a different times during the synthesis.[39]

Arrangement of atoms in bimetallic NPs depends on the differences in for instance diffusion rates, solubilities of the two metal species, surface energies γ, and vapour pressure. There are three main configurations of bimetallic NPs, which can be seen in Fig. 5. The different configurations presented in the figure are a) cluster-cluster formation, b) an alloy; randomly stacked atoms and c) core-shell structure (CS): A typical route to obtain CS structures is

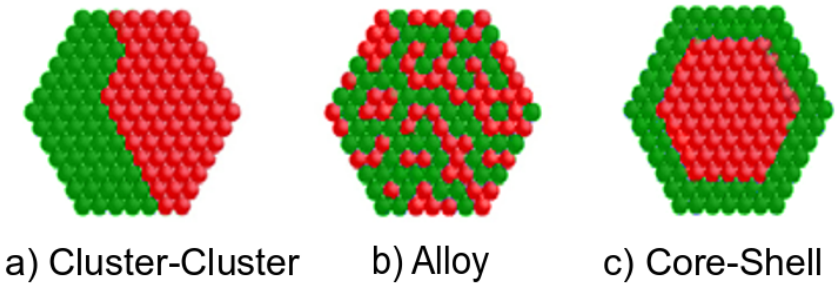

Figure 5: Three main simple configurations for bimetallic NPs, with green as atoms of metal 1, and red as metal 2. The configurations are a) cluster-cluster, b) alloy and c) core-shell.

by successive synthesis with seed mediated growth by thermal reduction. In this case the metals should have a big difference in electronegativity, as the core metal works as an "electron mediating" catalyst for reduction of the shell metal.[39] To avoid replacement reactions between core and shell, electronegativity of the shell should be lower than the core. For a system with Ni and Ir, some replacement might happen as the Pauling electronegativity are 1.91 and 2.2, respectively.[40]

The nature of core (substrate) and deposit shell (solute) depends also on the chemical bond and the strength of it between them, such as electronegativity. This decides in what degree they will interact. While the lattice mismatch decides the spacial variation between the interaction.[40] For well favoured growth of shell, there should be strong interaction between substrate and deposit with low lattice mismatch. Lattice mismatch for bimetallic and core-shell fcc structures should not exceed a value greater than 5 % to achieve heteroepitaxial growth.[9,40] Heteroepitaxial growth is the growth of solute on substrate by different types of materials.[28] Eq. (31) can be used to calculate the theoretical percentage lattice mismatch for bimetallic CS-NPs[9]:

$$\frac{(\text{core}_\text{a} - \text{shell}_\text{a})}{(\text{core}_\text{a} + \text{shell}_\text{a})/2} * 100\% \tag{31}$$

Where core_a and shell_a denotes bulk lattice constant for core and shell metal. Lattice mismatch between Ir and Ni is calculated to be 8.55 %.[9] However, there have been reported CS structures which go above this value, such as AuCu CS nanocatalysts with a mismatch of 11.4 %.[40] Furthermore, there has also been reported by Nong *et al.*[5] CS structures of NiIr. Depending on affinity amidst the metals, wetting angle θ, between substrate and deposit, and lattice mismatch, the formation of the next monolayer can grow in three different modes. These are called for Volmer-Weber growth (Island), Frank-van der Merwe growth (layer) and Stranski-Krastanove growth (island-layer), and are presented in Fig. 6[28]:

Island growth occurs when the deposited seeds have a greater affinity to each other than to the substrate, and are poorly wetted, $\theta > 180°$ (Eq. (29)). Layer growth is the most sought after growth mechanism, as this mode achieves growth of one and one monolayer at a time. This mechanism happens when the deposited metal has a higher affinity to the substrate, and $\theta < 90°$. The last mechanism is an intermediate combination of island and layer growth, and often introduces stress into the structure[28]. Strain occurs especially at the interface between the two metals, and structure dislocations are often introduced with this to partially relax the strain. Presence of strain in particles caused by mismatch can give deviation from equilibrium shape.[9]

Difference in surface energies, γ, between the two metals can have a noticeable effect on the outer surface, both for an alloy and for a CS structure. If there is a large difference, the metal with the lowest γ, which is usually the most noble metal, tends to segregate to the surface.[36,42] Segregation energy depends on surface energies of the transition metals and their crystal structures.[43] It can indicate and predict bimetallic core-shell compatibility and stability. Ruban

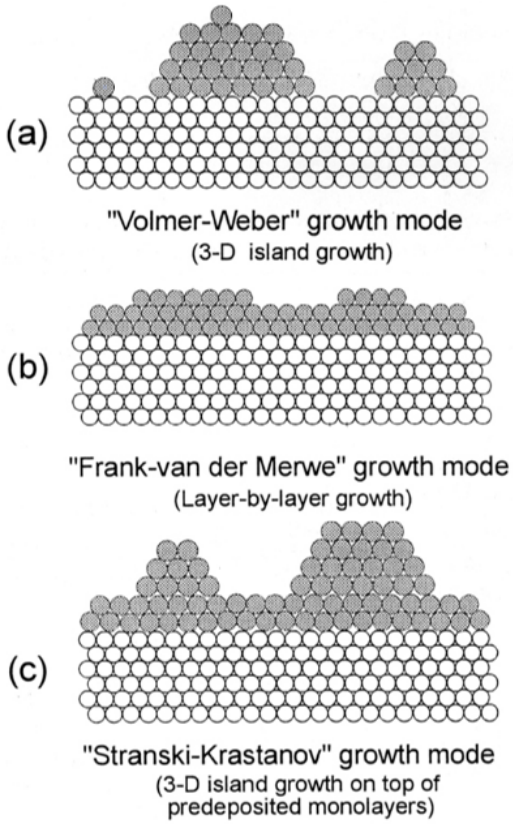

Figure 6: Schematic illustration of the three different growth modes of layer (film) growth. a) is Volmer-Weber growth (Island), b) Frank-van der Merwe growth (layer) and c) is Stranski-Krastanove growth (island-layer), a combination of layer and island growth. The figure is reprinted with some modifications, with permission from Lorenz *et al.*[41]. Copyright © 1995 Published by Elsevier B.V..

et al.[43] gave an an overview of different transition metals up to 5d and their theoretical compatibility with each other. A CS structure with Ni as core and Ir as shell is predicted to achieve a relative good stability with moderate antisegregation. It can therefore be expected that Ir, even with the highest value of γ will segregate to the surface.

Shell thickness contributes to the catalytic activity, as well as mass activity.[44] Achieving wanted shell thickness depends on the ratio between the core and shell precursors because of change in diffusion rates and thus growth mechanisms.

Hollow Nanoparticles - Kirkendall Effect

A great difference in diffusion rates between two metals in a bimetallic NP can lead to the formation of porous or hollow structures. This effect is called the Kirkendall effect.[45] It is a nonequlibrium interdiffusion effect between atoms and vacancies, that arises at phase interfaces such as particle surface or at grain boundaries. For a CS structure Kirkendall effect is predicted to happen at the grain boundaries between the two metals, and at the surface of the particle, as a coupled diffusion-reaction effect.[46] For alloys the effect occurs at places with highest concentration of structural impurities and strain.[9]

During the reduction of shell metal for CS, and $V_{depo}/V_{diff} >> 1$ together with high temperature, the diffusion rates of deposits are increased.[9] Firstly, the shell particles of CS-NP diffuse to the surface, are reduced and deposited at the surface (diffusion-reaction). The result is deformation and void formation at the surface. To counter the increase in vacancy defects, core particles diffuse outwards. Secondly, at the grain boundaries between the metals a cluster of structural effects occurs, with formation of voids. These vacancies will diffuse further inwards ("sink"), thus increasing the flux of core atoms outwards, causing a mix of both metals in the shell and an almost hollow to fully hollow core.[46]

For bimetals with high lattice mismatch, above 5 %, a greater concentration of vacancies are formed.[40,45] With an increase in interdiffusion rates defects are increased, causing inhibition or prevention of epitaxial growth. It is therefore important to control the growth mechanism for systems with large values of mismatch. Layer growth for bulk materials is highly unlikely at mismatch greater than 5 %. This is not the case for NPs because the particles can relax the inner stress and reduce γ by edge dislocations, coalescence, Ostwald ripening and other growth mechanisms.

2.5.1 Oleylamine in Metallic Nanoparticle Synthesis

Oleylamine (OAm, cis-1-Amino-9-octadecene) is a large and bulky primary alkylamine that is widely used in colloidal metallic NPs syntheses.[35,47] It is a weak reducing agent that also can function as a capping agent and solvent. With its high boiling point at ∼350 °C it can also work as a reducing agent for noble metals salts at high-temperatures.[47] The fact that OAm is a weak reducing agent gives opportunities to design nanoparticles by having more

control over the rate of reactions. Too strong reducing agents such as $NaBH_4$ lowers the control for possible NP-designs, and they have great amount of residual impurities.[11,28] For example, the final morphology, size and degree of monodisperse particles can be altered by the ratio between precursors and OAm.[48] Another advantage of using OAm is the low cost compared to other pure primary alkyl amines, however, there are concerns regarding purity compared to other alkyl amines and reproducibility when using OAm for synthesis.[35]

For transition metals, and especially late transition metals, the functional $-NH_2$-group bonds weakly to the surface, and at high temperatures the $-NH_2$-group can be detach from the surface. Syntheses including these metals, such as Ni, might therefore be prone to agglomeration and yield polydisperse particles.[11,47] Synthesising Ni particles with OAm should not exceed a reaction time of 2 h due to increased possibility for agglomeration.[49] Furthermore, at high-temperature syntheses e.g. $>240\,^{\circ}C$ hcp phase of Ni is favoured, compared to the fcc phase.[11,35]

2.5.2 Tri-n-octylphosphine in Nanoparticle Synthesis

Tri-n-octylphosphine (TOP) functions as a capping agent for MNPs syntheses. It is often used as capping agent for size control of magnetic materials such as Fe, Co and Ni, as TOP has strong affinity to transition metal surfaces.[11] Adding TOP may give impurities, or increase the amount of impurities such as phosphines and carbon.[49] Metals that are prone to oxidation, such as Ni, can be oxidised by TOP.[49]

3 Characterisation Methods

Knowledge about catalyst structure and morphology is crucial for understanding its chemistry[50]. This section shortly describes different instrumentation- and characterisation methods used in this project. The description includes what the instrument does and what kind of information it provides that is important regarding the results in this thesis.

3.1 Cyclic Voltammetry (CV)

Cyclic Voltammetry (CV) is a powerful qualitative- and a quantitative electroanalytical method, that monitors different chemical processes that involves transfer of electrons. It provides important in-situ information about an electrochemical system by giving correlated information of surface compositions, their characteristic activities and potentials. Furthermore, CV can be utilised as synthesis method as well, such as dealloying, in presence of CO-gas; With the possibility to monitor compositional changes at the surface of sample during the process.[20] Characterisation of oxide electrodes is best performed by CV.[7] One of the greatest advantages of CV are the high sensitivity and the methodological simplicity.

Experimental design for a three-electrode system consist of a working, counter and reference electrode that are separated from each other and immersed in an liquid electrolyte. The reference electrode has a known potential with a known redox couple, such as reversible hydrogen electrode (RHE). RHE consists of the reaction between hydrogen gas and sulphuric acid (hydrogen evolution reaction, HER), that is set to have a potential to $E^0 = 0.0V$.[51] Platinum is often used as a counter electrode, that is used to complete the circuit and supply electrons to the system. The working electrode consist of the material that shall be examined. By applying a potential over the system that corresponds to electroactive window, i.e. when redox reaction between the reference and working electrode occurs, a corresponding current response (per electrode area) of transferred electrons is given. The potential and current responses are measured between the working and the reference electrode. Current response at a given potential is specific for a given specie. A potentiostat applies the potential and read and visualise this correlating response between the potential and current density, over the measured time.[13]

A voltammogram gives the correlation between E vs. j. To obtain a cyclic

voltammogram the potential is ramped back and forth between a set initial and maximum potential window and is measured over a given time. The rate of change in potential versus time is the sweep rate (ν) (scan rate). By sweeping between a potential window surface alternations can occur, by formatting irreversible species and prevent re-solvation of these species. The potentials in voltammograms must be jR-corrected as a result of resistance in the system caused by e.g. transport processes between the working and counter electrode. This correction are usually set at 85 %.[13]

3.2 Linear Sweep Voltammetry (LSV)

To examine a catalyst's activity, linear sweep voltammetry (LSV) is useful. Compared to CV, there is no cycling between two potentials, as the scan is done after maximum potential is reached. The potential window is set to give the polarisation curves. It is by LSV that Tafel plot and ESCA can be calculated.[25]

Experimental set-up for LSV is the same as for CV, and the voltammograms have to be jR-corrected as well. This is previously described in Section 3.1.

3.3 X-ray Diffraction (XRD)

X-ray diffraction (XRD), is a useful method to decide if the sample is crystalline or not, calculating particle size and for estimating spacing between each atomic layer in a crystalline structure.[52] XRD is a non-destructive method where the sample is beamed with monochromatic light typically between 0.7-2 Å.[28] For an ordered structure, elastic scattering of electrons happens (diffraction), and the scattered light is recorded by a diffractiometer. From the diffractiogram, peak spacing can be calculated, by using Bragg's law[52](Eq. (32)):

$$n\lambda = d_{hkl}sin\Theta + d_{hkl}sin\Theta \tag{32}$$

Wavelength of X-rays is λ and Θ is the incident beam angle, normal to the reflecting lattice plane. In the crystalline phase d_{hkl} is the spacing between the atomic planes, and is characteristic for a given species.[28] The spacing, d_{hkl}, can be calculated, as it is a function of Miller indices and the lattice parameters.[52] n is a positive integer (n = 1, 2, 3,..,n), and the order of reflection. Single phases can be determined if scattered light is coherent.

Coherent light results in even values of n.[53]

A perfect, infinite crystal shows single, narrow peaks in the diffractogram. For non-perfect crystals, peak broadening occurs as a result of impurities due to increased internal stress in the structure. Furthermore, for structures below 100 nm, destructive light scattering may happen resulting in further peak broadening.[53] Assuming there is no inhomogenous strain in the structure, Scherrer's formula can be used to estimate the crystallite size, D, from the peak broadening[28,53,54](Eq. (33)):

$$D = \frac{K\lambda}{\beta cos\Theta_B} \tag{33}$$

Where K is the Scherrer's constant, that depends heavily on the shape- and size distribution of the particles,[54] and β is the peak broadening at half of the maximum intensity (FWHM). It is given in terms of radians. The wavelength of the X-rays is denoted λ, and Θ_B is the diffraction angle. Peak position gives certain information about homogeneous and inhomogenous strains in the structure. While the intensity of the diffraction pattern says something about the crystalline phases, and can be used to measure structural properties, as a function of the diffraction angle $n\Theta$, from Eq. (32)), where n is usually equal to two.[28] Unit cell size and geometry can be experimentally found from the angle of the diffraction peaks.[52]

3.4 Electron Microscopy (EM)

Electron microscopy (EM) is an important characterisation method, that utilises a high energy electron beam to study a material's topography trough imaging structures down to nanoscale.[28] An indication of chemical composition of the sample specie may also be estimated. EM can be done by different approaches, where Scanning Electron Microscopy (SEM) and Transmission Electron Microscopy (TEM) is two highly utilised methods today. A combination of those two methods, called Scanning Transmission Electron Microscopy (S(T)EM), can achieve clear images of single atoms.[55]

3.4.1 Scanning Electron Microscopy (SEM)

Scanning electron microscopy (SEM) is a microscopy technique able to produce topographical information down to a resolution of a few nanometers.

The technique functions by focusing a source of electrons into a beam, which is then rastered over the surface of a sample.[28] Various interactions occur between electrons and sample, resulting in photons and electrons emitted from the sample. A cathode ray tube collects emitted electrons, allowing for the generation of SEM images. There are three types of images generated: inelastically scattered secondary electron (SEs) images where the electron energy is less than 50 eV, elastically backscattered electron (BSEs) images where electron energy is more than 50 eV, and elemental X-ray maps.[28,56] The specific technique for obtaining elemental X-ray maps are typically referred to as energy dispersive X-Ray (Spectroscopy), or EDX for short, and is described in Section 3.4.3.

As a characterisation method, SEM offers the ability to generate 3D images of the sample's surface. Resolution of images is determined by the wavelengths of the electron beam, and the objective of the instrument's ability to gather electrons. The topographical contrast appears as the probability for electrons to reach the detector increases for surface features which are tilted towards the detector.[28]

No special sample preparation is required for a SEM analysis, as bulk samples also can be characterised. However, if the sample is not electrical conductive it must be sputtered with a conductive species before analysis in order to avoid charging effects.[57] The analysis is done under low to high vacuum, 10^{-3}-10^{-7} bar, with a dry sample.[55]

3.4.2 Transmission Electron Microscopy (TEM)

Transmission electron microscopy is a technique offering exceptional image magnification capabilities, ranging from 50 to 10^6, as well as diffraction information for a sample. Electrons from a source are accelerated to 100 keV, or even as high as 1 MeV, and projected onto a sample thinner than 200 nm.[28] The electrons travel through the sample, either undeflected or deflected.

Elastic collisions between projected electrons and sample electrons give rise to diffraction patterns. Inelastic collisions at structural heterogeneities, e.g. grain boundaries, defects, density variations etc., lead to variations in the intensity of transmitted electrons due to absorption and scattering effects.[28] Transmitted electrons are captured by an objective, and an image can be generated.

Sample preparation may be difficult for TEM analysis, as the sample needs to be thin enough to allow for transmission of electrons. Increasing the electron beam energy leads to slightly weaker interactions between electrons and matter, and thicker samples may be analysed.[28] However, for NPs sample thickness is generally not an issue.

3.4.3 Energy-dispersive X-ray Spectroscopy (EDX)

Energy-dispersive X-ray spectroscopy is a characterisation technique which allows for elemental identification. When a sample is irradiated by an electron beam or photon source, electron collisions may lead to excitation of core electrons in the irradiated atom, or even ejection of core electrons. For EDX, the ejection of electrons from an inner shell of an atom leaves an electron vacancy, which is subsequently filled by an electron from an outer shell of a higher energy level. In this relaxation process the excess energy is emitted as an X-ray photon. The chemical composition of a sample can be determined by the energy level of the X-rays.[28]

4 Experimental

The different approaches used for preparation and synthesising various iridium oxide catalysts for OER are given in this chapter. Descriptions for each method are given in the order of: anodically formed iridium films (AIROF), IrO_2 nanoparticles formed by hydrolysis, electrochemically dealloyed $A-IrNi_x$ NPs and core-shell $CS-IrNi_x$ nanoparticles (CS-NPs) synthesised without and with tri-n-octylphosphine (TOP) T_y-IrNi_x.

Subsequently, each method utilised to characterise the samples is described. These are: CV, LSV, XRD, SEM, TEM and EDX. Necessary information on preparation of electrodes and inks for electrochemical dealloying and oxidation, and electrochemical characterisation are described here as well.

4.1 Synthesis

4.1.1 Anodically Formed Iridium Oxide Films (AIROF)

The Iridium bulk electrode was prepared by mechanically polishing until the electrode showed a glassy finish (described in Appendix B). Anodically formed iridium oxide films (AIROF) on the bulk Ir-electrode were obtained using CV in a potential interval of 0.05-1.5 V, for a minimum of 50 cycles. A sweep rate of $150\,mV\,s^{-1}$ was used. To calculate outer "accessible surface" the electrode was cycled up to 400 times, with results recorded at every 50 cycles.[17] Macroscopic surface area of the Ir-electrode was of $1.95\,cm^2$.

A reversible hydrogen electrode (RHE) was used as reference electrode and Pt as counter electrode. The electrodes were immersed in a $0.5\,mol\,dm^{-3}$ sulphuric acid electrolyte solution (H_2SO_4)(96%, Sigma Aldrich), in a five necked glass cell. To carry out the CV, a Biologic VMP3 potentiostat was used, together with a Pine instrument. Cycling was done in N_2-atmosphere.

4.1.2 Hydrolysis of IrO_2 Nanoparticles

The procedure for synthesising IrO_2 NPs was based on the hydrolysis routine done by Ingrid A. Lervik *et al.*[58]

Potassium hexachloroiridinate(IV) (K_2IrCl_6)(99.99%, Sigma Aldrich), DI water (Millipore Direct-Q3 18.2 MΩ cm) and 0.5 mol dm^{-3} potassium hydroxide (KOH)(85%, Merck) was added to a conical beaker with a teflon stirrer. The chosen volume of KOH was such that KOH was in excess for the reaction, keeping pH>9. Thereafter, the solution was heated up by water bath to 80 °C and held there for 1 hour, giving a "cobalt blue" solution. After cooling the solution down to room temperature, yielding a violet solution, 1 mol dm^{-3} nitric acid (HNO_3)(69%, Sigma Aldrich) was added drop wise until pH=9 was reached, and the formation of black precipitate of IrO_2 was observable. The solution was again heated up to 80 °C and held there for 30 minutes, before it was cooled down to room temperature.

The precipitate and solvent were centrifuged for 5 minutes at 5000 rpm, after which the solvent was carefully removed using a glass pipette. To wash the precipitate DI water was added. The precipitate was then sonicated until fully redispersed, before centrifuging for 7 minutes at 5000 rpm. The cleaning process was repeated 4 times.

After washing the product, it was dried for 20 hours at 110 °C, ground and annealed for 30 minutes at 500 °C. The annealed product was then finely ground and characterised by XRD, SEM, TEM, EDX, LSV and CV.

4.1.3 $IrNi_x$ Core-Shell Nanoparticles

Synthesis without TOP

Preparation of $IrNi_x$ core-shell nanoparticles (NPs) without tri-n-octylphosphine (TOP) present wAS done by a two-step successive synthesis routine. In total 4 powders were synthesised, with molar ratios of Ni to Ir of $x = 2.0$, 3.0 and 5.0, where two powders had a mass ratio of 2.0. One $x = 2.0$ sample was synthesised with oxygen present, denoted Ox-CS-$IrNi_2$. The other three samples were synthesised without oxygen present, and are named CS-$IrNi_2$, CS-$IrNi_3$ and CS-$IrNi_5$, respectively.

For sample Ox-CS-$IrNi_2$, 40.5 mg of Nickel precursor Nickel(II)nitrate hexahydrate ($Ni(NO_3)_2 \cdot 6\,H_2O$) (Sigma Aldrich, 99.999%) was added to a three necked round bottom flask together with 10 mL oleylamine (OAm) (Sigma Aldrich, 70%) and a teflon stirrer. A schematic overview of the set up can been seen in Fig. 7.

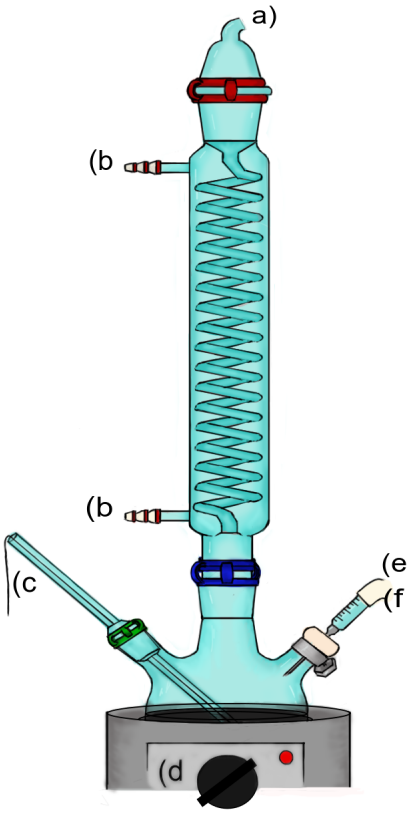

Figure 7: Schematic overview of the set up for all $IrNi_x$-NPs syntheses. The set up consisted of a) Schlenk line that included outlet for Ar-gas to bubbler. b) inlet/outlet for the water refluxer, c) thermocouple, coupled to temperature programmer and d) heating mantle that were coupled to the temperature programmer. Two syringes were placed in the septum, where the first one e) was coupled to a second bubbler for better gas-flow, and the second one f) was for transferring precursors.

At point a) in the temperature profile shown in Fig. 8, air was evacuated from the system using a Schlenk line, point a) in Fig. 7. Pressure in the system was measured to roughly 1.4 mbar. After ten minutes, shown as point a) in the profile, the vacuum pump was turned off and Argon-gas (Ar) was added to the system. No control of pressure was done from here on. However, two bubblers were coupled to the system shown in point a) and e) in the set-up, to control the Ar-flow, and to prevent excessive pressure in the system during synthesis. A schematic overview of temperature profile for core-shell synthesis is shown in Fig. 8. At point c) the Ni-seeds were cooled down to 80 °C, and 20.5 mg Iridium(III)-chloride hydrate, $IrCl_3 \cdot H_2O$ (Sigma Aldrich,

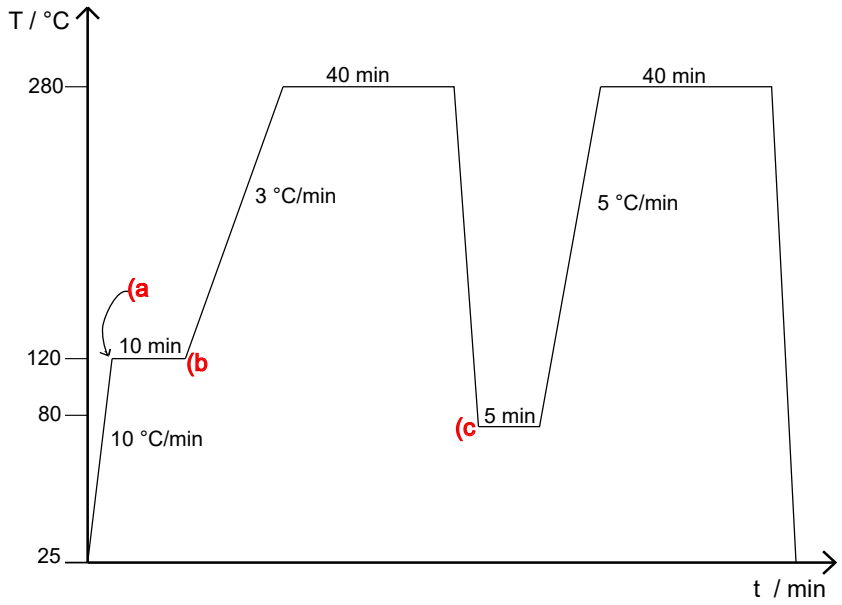

Figure 8: Schematic overview of temperature profile for core shell synthesis. Ramp rates for temperature elevation is given in [°C min^{-1}] and shown by slanted lines. Rest periods are the horizontal lines [min] at a given temperature [°C] indicated at the y-axis. At point a) vacuum pump is turned on, at b) vacuum pump is turned off and Argon gas turned on. Iridium precursor is added at point c).

99.9%) together with 10 mL OAm was added through a septum point f) in Fig. 7. The product was thereafter washed as described in Section 4.1.5. For powders synthesised without oxygen present, all precursors were prepared in a glove box in N_2-atmosphere. The experimental set-up and OAm were initially flushed with Ar-gas to be sure no oxygen was present. Transferring dispersed precursors (suspended in OAm) was done using syringes and septa. When the Ni:Ir ratio was varied, the amount of OAm was changed accordingly such that the concentration of precursor in solvent remained constant at 13.9 mmol dm^{-1} for the Ni-precursor, and 6.87 mmol dm^{-1} for the Ir-precursor. Supersaturation level was kept equal for all samples.

Synthesis with TOP

CS-NPs synthesised with TOP followed the same routine as those without TOP present, with the exception of the addition of TOP together with OAm. TOP was added in an expectation that further reduction of NP size and

control of morphology would promote further growth of Ir. TOP was added together with OAm at point a), shown in Fig. 8. The molar fractions of xOAm and yTOP were $x = 0.8$ and $y = 0.2$, $x = 0.9$ and $y = 0.1$, and $x = 0.95$ and $y = 0.05$ (see Fig. 9).

For samples with TOP added, a molar ratio of Ni:Ir of 2.0 was used, and samples are named T_y-$IrNi_2$. Hence, a total of three samples were made with TOP added. The total concentrations of OAm and TOP were held constant for all five samples.

4.1.4 $IrNi_x$ Alloy Nanoparticles

A one-pot co-reduction synthesis routine was used to produce $IrNi_x$ alloy NPs. A total of four powders were synthesised. One was synthesised with oxygen present, and three in a glove box in N_2-atmosphere. The one made with oxygen present, named $Ox{-}A{-}IrNi_2$, was synthesised with a Ni:Ir ratio of 2.0. The remaining powders had ratios of x = 2.0, 3.0 and 5.0, and are named $A{-}IrNi_2$, $A{-}IrNi_3$, $A{-}IrNi_5$, respectively.

For sample $Ox{-}A{-}IrNi_2$, 40.5 mg of $Ni(NO_3)_2x_6H_2O$ (Sigma Aldrich, 99.999%), 20.5 mg of $IrCl_3{\cdot}\ H_2O$(Sigma Aldrich, 99.9%) and 20 mL OAm (Sigma Aldrich, 70%) were added to a three necked round bottom flask. For $Ox{-}A{-}IrNi_2$ the precursors were added directly to the flask at point a) in Fig. 9. The remaining three samples were prepared without oxygen present in the same manner as in the CS-synthesis (Section 4.1.3). When the Ni:Ir precursor ratio was varied, the total concentration of precursors in the solvent was kept constant. The temperature profile for a $IrNi_x$ NP synthesis is shown in Fig. 9, and follows the same principles as in CS-synthesis. Products were cleaned according to Section 4.1.5.

4.1.5 Cleaning Procedure of $IrNi_x$ Nanoparticles

Synthesis without TOP

CS and alloy-NPs synthesised without TOP followed the same cleaning procedure, as they were much easier to separate from the solvent than the products with TOP present. While CS products were harder to separate from solvent than the alloy NPs, they were still magnetic such that a strong magnet was

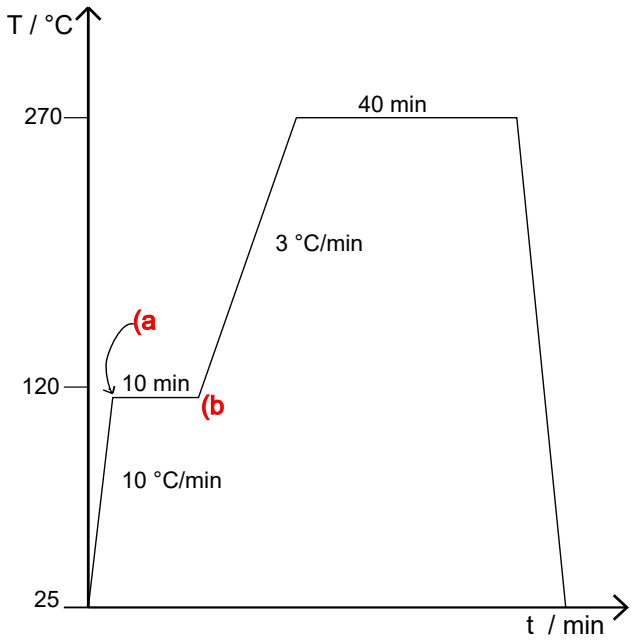

Figure 9: Schematic overview of the temperature profile for alloy NP synthesis. Ramp rates for temperature elevation is given in [°C min^{-1}] and indicated by slanted lines. Rest periods are the horizontal lines [min] at a given temperature [°C] indicated at the y-axis. At point a) the vacuum pump is turned on, at b) the vacuum pump is turned off and Argon gas turned on.

used to help with the cleaning procedure.

Products were washed three times: the first time with 10 mL toluene (Merck KGaA, ISO) and 15 mL isopropanol (IPA) (Sigma Aldrich, 99.999%), and the second and third time with 5 mL toluene and 20 mL IPA. The samples were centrifuged at 7500 rpm for 30-45 minutes after each wash. To separate product (especially CS-products) and solvent from each other, a strong magnet was placed underneath the centrifuge tubes during pipetation. Cleaned products were then dispersed and stored in toluene. The CS NPs were easily re-dispersed, hence the usage of pipette rather than decanting the solvent.

Synthesis with TOP

For samples containing TOP, a different washing routine was used. Each sample was divided equally into three centrifuge tubes, and added 4 mL toluene (Merck KGaA, ISO), 15 mL EtOH (Sigma Aldrich, 95.0%), 4 mL IPA (Sigma

Aldrich, 99.999%) and 4 mL acetone (Sigma Aldrich, ≤99.5%). There was no phase separation between all of the solvents. Directly after the addition of toluene the samples were sonicated for circa 10-15 minutes, and thereafter the rest of the solvents were added. Thereafter the samples were centrifuged at 13500 rpm for 10-20 minutes. This was done circa 10 times until the product started to feel and look like a powder and not like "oily cement".

With the addition of TOP the samples were no longer magnetic, hence they were far more difficult to separate from solvents compared to those without TOP. If a sample did not separate properly, more EtOH was added until some separation occurred. This was repeated until the first full separation took place. Finished cleaned samples were dispersed and stored in toluene.

4.1.6 Catalyst Ink Preparations

CS- and A-$IrNi_x$ catalyst inks, except A-$IrNi_3$, were loaded on a 0.196 cm^2 glassy carbon electrode, which was polished to mirror finish. Each ink consisted of 50 µL Nafion®(2.4 vol%) and 2 mL EtOH (97.6 vol%) and was sonicated for 30-60 minutes before application onto the electrode. 5 µL ink was dropcasted twice (to a total of 10 µL) onto the electrode in a N_2-saturated atmosphere. Catalyst loading for all samples are presented in Table 1

No stabiliser was added due to interference of carbon for the OER. A-$IrNi_3$ was prepared with 1500 µL EtOH, 500 µL IPA and 50 µL Nafion®, as the ink was difficult to disperse properly without any stabiliser. TOP-samples were all dispersed in 2 mL IPA

4.1.7 Electrochemical Dealloying of $IrNi_x$ Alloy Nanoparticles

Voltammetric response of $IrNi_x$ alloy catalysts before dealloying was tested with three initial CV-scans of 100 mV s^{-1}, between 0.05 V to 0.8 V in a CO-atmosphere. Dealloying was done by setting a voltage interval of 0.05 V to 1.2 V and a sweep rate of 500 mV s^{-1}, with a total of 200 cycles. During dealloying the CO-gas was purged though the system to achieve CO-oxidation of the alloy and the formation of core-shell structures.

Table 1: List of catalyst loading for all samples applied on a GC-electrode with area equal to $0.196\,\mathrm{cm}^2$.

Sample	**Loading** $\mu\mathrm{g\,cm}^{-2}$
$hIrO_2$	31
$Ox-A-IrNi_2$	31
$A-IrNi_2$	25
$A-IrNi_3$	25
$A-IrNi_5$	31
$Ox-CS-IrNi_2$	26
$CS-IrNi_2$	27
$CS-IrNi_3$	27
$CS-IrNi_5$	26
$T_{0.05}-IrNi_2$	25
$T_{0.1}-IrNi_2$	26
$T_{0.2}-IrNi_2$	30

4.1.8 Oxidation of $IrNi_x$ Nanoparticles

Oxidation of all $IrNi_x$ NPs was done by cycling between 0.05 V to 1.5 V with a sweep rate of $500\,\mathrm{mV\,s}^{-1}$ for 50 cycles. For A-$IrNi_x$ this was done right after dealloying.

4.2 Characterisation

A short description on how each method was implemented and carried out is given in this section. In total 12 samples were characterised by XRD, SEM, TEM, EDX, LSV and/or CV. XRD, SEM, TEM and EDX were done before oxidation and dealloying (alloys) of $IrNi_x$-samples. With the exception of sample $A-IrNi_2$, which was characterised before and after dealloying. Table 2 gives an overview over these samples with respective names and characterisation methods for the given sample.

Table 2: Overview over synthesis methods with respective sample names and characterisation methods utilised on each sample. Sample A−$IrNi_2$ is denoted with "*", for TEM, SEM and EDX, as this sample was tested before and after dealloying, yielding before- and after-images. T_y are core-shell-NPs synthesised with TOP present, where y is the molar fraction of TOP. This gives sample names such as $T_{0.2}$−$IrNi_2$

		Characterisation Method				
Synthesis	**Sample**	**XRD**	**TEM/SEM***	**EDX***	**CV**	**LSV**
AIROF	bIr				X	
Hydrolysis	$hIrO_2$	X	X	X	X	X
CS	Ox-$IrNi_2$	X	X	X	X	X
	$IrNi_2$	X	X	X	X	X
	$IrNi_3$	X	X	X	X	X
	$IrNi_5$	X	X	X	X	X
A	Ox-$IrNi_2$	X	X	X	X	X
	$IrNi_2$	X	X*	X*	X	X
	$IrNi_3$	X	X	X	X	X
	$IrNi_5$	X	X	X	X	X
T_y	y=0.2 $IrNi_2$	X	X	X	X	X
	y=0.1 $IrNi_2$	X	X	X	X	X
	y=0.05 $IrNi_2$	X	X	X	X	X

4.2.1 Microscopic and Spectroscopic Characterisation

XRD

Sample $hIrO_2$ was prepared in a Si cavity holder in powder form. Other nanopowders were dispersed in toluene before application on a flat Si-holder, and subsequently dried by evaporation in a fume hood.

Diffractograms were obtained using a Bruker D8 A25 DaVinci X-ray diffractometer with CuKα radiation and LynxEye™ SuperSpeed Detector, 90 position sample changer. For all samples fixed slits were used. Theoretical peak values for all diffractograms were collected from PDF−$_4^+$.

TEM/SEM/EDX

Copper TEM-grids with 300 mesh were used for TEM, SEM and EDX-measurements. A Jeol JEM 2100 - LaB6 microscope was used for BF/DF-TEM, SEM and EDX measurements. Samples synthesised with TOP present were irradiated by laser for 20 seconds to remove solvent residues.

Particle sizes and size distributions for TEM images were calculated using software DigitalMicrograph™ . All EDX projects were retrieved from and analysed with AZtec. For calculations of particle size and average area of SEM and/or TEM images after retrieving them with AZtec, ImageJ was used.

TEM, SEM and EDX measurements were performed by Bjørn G. Solheim, senior engineer at TEM Gemini Centre NTNU.

4.2.2 Electrochemical Characterisation

CV and LSV

Preparation of inks has already been described in the previous Section 4.1.6. The same cell system was used for all measurements, except for the analysis of Ir coverage of catalysts. For the Ir coverage analysis, $0.1\,\mathrm{mol\,dm^{-3}}$ KOH (85%, Merck) was used as electrolyte instead of the normal $0.5\,\mathrm{mol\,dm^{-3}}$ H_2SO_4(96% , Merck). The cell system was composed of a three compartment glass cell with a rotating disk electrode (loaded with catalyst)(RDE, Pine instrument) of glassy carbon (GC), a Pt counter electrode and a reversible hydrogen electrode (RHE) as reference electrode. The GC-electrode had a surface area of $0.196\,\mathrm{cm^2}$. Two different potentiostats (Biologic and NOVA) were used. Biologic was used for electrochemical measurements. NOVA Autolab (ver. 1.11) was used for dealloying and electrochemical experiments, as this experiment required a fume hood due to CO usage. A bulk Ir-electrode was used as the working electrode for the formation of AIROF, with a surface area of $1.95\,\mathrm{cm^2}$.

5 Results

Results are presented in two different sections: characterisation of catalysts and electrocatalytic testing. Characterisation of catalysts is further divided into XRD, SEM, TEM and EDX, while in electrocatalytic testing results from CV and LSV are presented.

5.1 XRD

5.1.1 $hIrO_2$

The background subtracted diffractogram for $hIrO_2$ can be seen in Fig. 10: This pattern is almost identical to the one obtained by Lervik *et al.*[58], synthe-

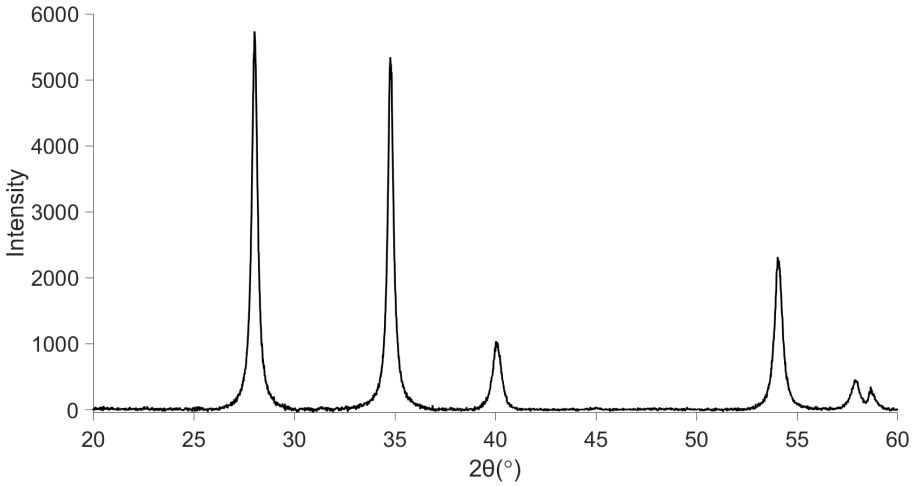

Figure 10: XRD pattern of IrO_2 NPs synthesised by hydrolysis, and calcined at 500 °C for 30minutes.

sised by the exact same synthesis routine. The only difference in the pattern is that we achieved a higher intensity. We can tell that the particles were highly crystalline, because of the high intensity and the narrow peaks.

The pattern fits a rutile type structure with tetragonal crystal system. Where the highest peak value are equal to 5731, at an angle of 28.05°, and the second highest equal to 5344 at an angle of 34.78°. For $hIrO_2$ that angle results in [110] and [101] planes, respectively.[27,58] As the particles were of nano-size,

some peak broadening occurred. No shifts were observed. We can assume full oxidation of Ir, as we can not observe any peaks for Ir-metal in the pattern.

5.1.2 $IrNi_x$ Alloy Nanoparticles

XRD pattern for A−$IrNi_x$-samples are presented as an all-in-one stacked diffractogram, and can be seen in Fig. 11. Horizontal dotted lines shows theoretical angles for $Ir_{0.5}Ni_{0.5}$ and Ni(0) that were best fitted species for these peaks in the diffractograms. Both $Ir_{0.5}Ni_{0.5}$ and Ni(0) have an fcc-crystal structure. In Fig. 11, the peak at 76.93° is not visible for non-Ox-samples due to low intensity, but it can be seen in the non-stacked XRD spectra in Appendix C.1.3, Fig. 44. Lowermost sample Ox−A−$IrNi_2$, obtained the highest

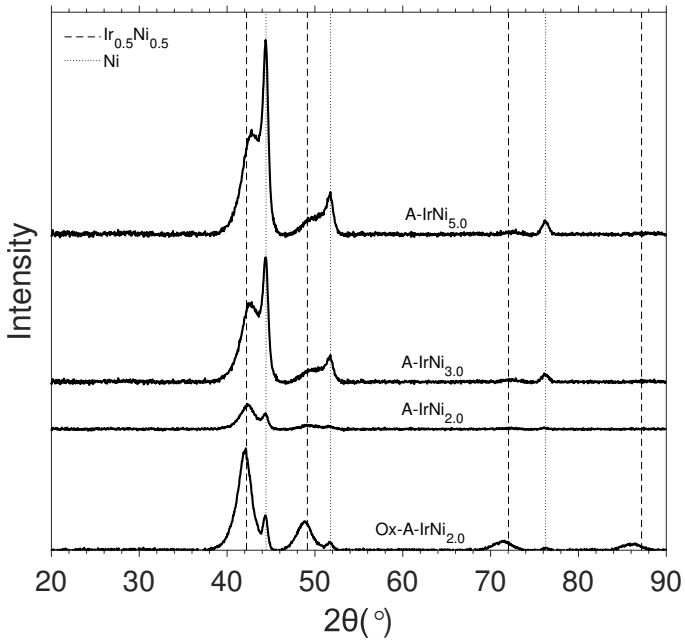

Figure 11: Stacked XRD pattern of all alloy-samples, before dealloying and oxidisation. With Ox-A-$IrNi_2$ as lowermost sample, and the following samples have increasing amount of nickel. Vertical dotted and dashed lines stands theoretical fitted angle values for $Ir_{0.5}Ni_{0.5}$ and Ni(0), respectively.

intensity along with narrowest peaks. The peaks are also better defined than the samples above. This can be seen better by comparing stand alone diffractograms of e.g. Ox−A−$IrNi_2$ and Ox−A−$IrNi_2$, shown in Appendix C.1.3, Fig. 44a. Furthermore, the samples that were synthesised inside the glove

box, the peaks follow a trend; with an increase in the amount of Ni, there is an increase in peak intensity, including a simultaneously reduction of $Ir_{0.5}Ni_{0.5}$ with increasing Ni-peaks. There were no visible Ir-peaks. Even thought there is an overlap between the fitted assumed peaks and nickel oxides, we could assume no formation of nickel oxide due to not observing any peak at $\sim 62^{\circ}$ (cf. PDF-4+).

5.1.3 $IrNi_x$ Core-Shell Nanoparticles

Synthesised without TOP

XRD-spectra for all core-shell IrNi nanocatalyst before being oxidised, can be seen as stacked in Fig. 12. The first and lowermost pattern labelled Ox-CS-$IrNi_2$ was synthesised with oxygen present, and the rest in a glovebox. Dotted, vertical lines denotes best fitted species, with theoretical values for Ni and $Ir_{0.5}Ni_{0.5}$-alloy crystal structures. All samples show presence of IrNi-alloy and Ni-phase, but no pure Ir phase. Peak intensities for Ox-CS-$IrNi_2$

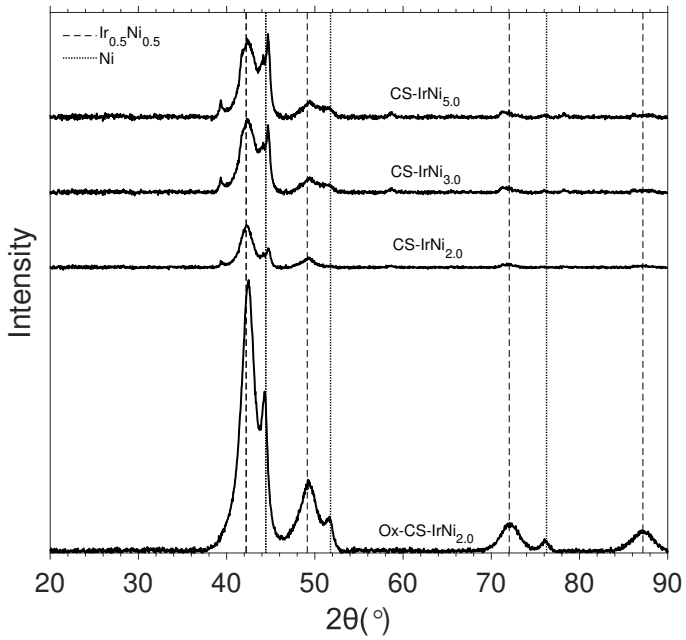

Figure 12: Stacked XRD pattern of all CS−$IrNi_x$-samples, before oxidisation. With Ox-CS-$IrNi_2$ as lowermost sample, and the following samples have increasing amount of nickel. Vertical dotted and dashed lines stands theoretical fitted angle values for $Ir_{0.5}Ni_{0.5}$ and Ni(0), respectively.

is of greater values than the samples that were synthesised without oxygen present. Difference in intensity between Ox-CS-$IrNi_2$ and the rest might be due to an increase in crystallinity because of oxygen. However, no prominent peak at around 62° can be seen for any samples, and so no formation of nickel oxide occurred. Given the theoretical peak values, it can be assumed that the samples have identical facets as reported by Hong Nhan Nong *et al.*[5] An overall increase in peak intensity is consistent with Hong Nhan Nong *et al*[5] results. We can see an greater increase in peak intensity with increased Ni content, due to purer Ni-phase and an increase in crystallinity.

A possible hcp phase of Ni was formed with increasing Ni content. The slightly right shifted peaks at 39.59°, 58.81° and 71.62° in Fig. 13 are compatible with garutiite phase of Ni (hcp). Some database reflections are not included due to overlap and too low peak intensity to be visible in Fig. 13. Nickel Hydride (Ni_2H), could also fit into this pattern, however this phase

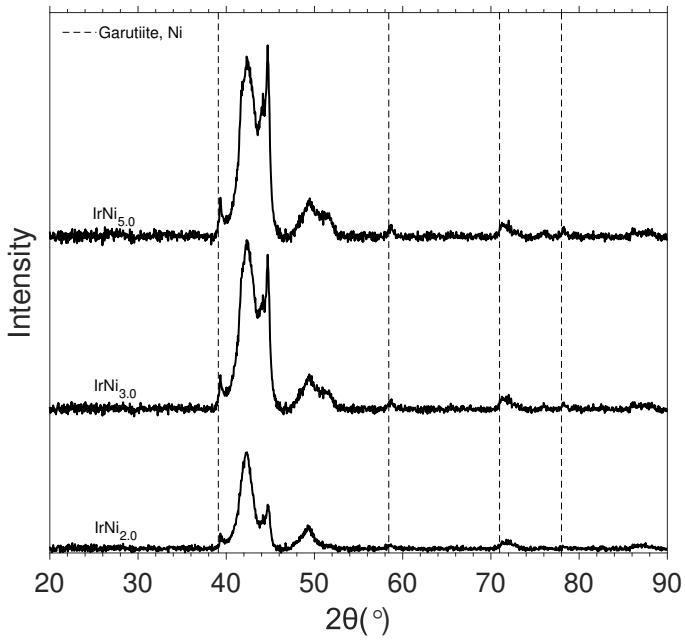

Figure 13: Stacked XRD pattern of all CS-samples, before oxidisation. With Ox-CS-$IrNi_2$ as lowermost sample, and the following samples have increasing amount of nickel. Vertical dashed lines denotes theoretical peak values for hcp-packed Ni structure (Grautiite).

had most likely not formed as it is unstable with the presence of oxygen. There has been reported hcp phase synthesised by OAm at high temperatures, $T > 240\,^{\circ}\mathrm{C}$.[59] Thus, it can be assumed that the catalysts contain some Ni with hcp packed structures.

Synthesised with TOP

Stacked diffractograms for samples synthesised with TOP are presented in Fig. 14. All samples show low intensity, and only one out of three visible peaks are suggested to be a definite peak. The one suggested can be observed at ∼40.78°, for all 4 samples.

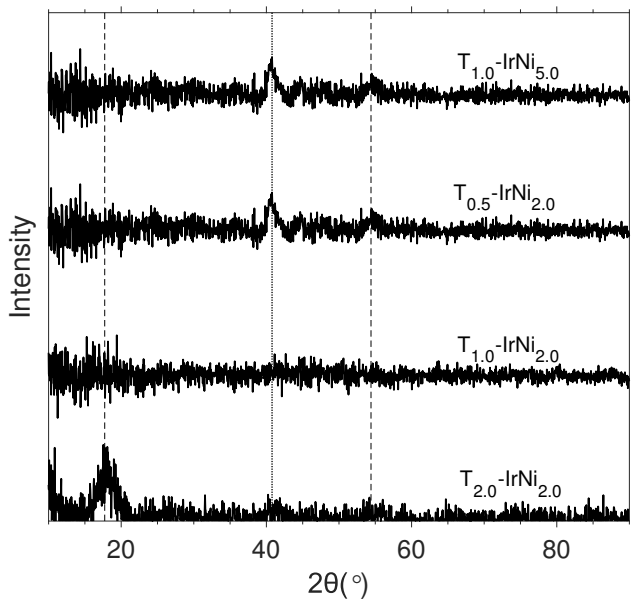

Figure 14: Stacked XRD pattern of all T_y−$IrNi_2$-samples, before oxidation. Vertical dashed dotted line denotes present peak, and dashed vertical lines denotes possible peaks.

For sample $T_{0.2}$−$IrNi_2$, a peak at 17.73° can be observed. This peak might be due to nickel phosphide, with empiric formula NiP_3, considering that this structure has a cubic crystal structure as well as Ni. The theoretical value for NiP_3 is at 16.06°, thus some right shift is present if the peak belongs to nickel phosphide. Another possible structure is NiO, however, there is no peak at ∼63°. Therefore we assume no NiO, but we can not confirm without XPS. Other assumed elements and crystal structures present (such as Ir, Ni, IrNI, NiH etc.) can only be fitted into one of the peaks, the one at 40.78°. All considered structures result in right shift. In the final two topmost samples $T_{0.05}$−$IrNi_2$ and $T_{0.1}$−$IrNi_5$ there might be a peak at 54.41° as well. If this is the case, then iridium phosphide (IrP_2) might be present as well. No pure Ni(0) or Ir(0) phases can be observed.

5.2 TEM, SEM and EDX

5.2.1 $hIrO_2$

BF-TEM images of sample $hIrO_2$ formed by hydrolysis are presented in Fig. 15, below: Needle like shaped crystals formed by anisotropic growth

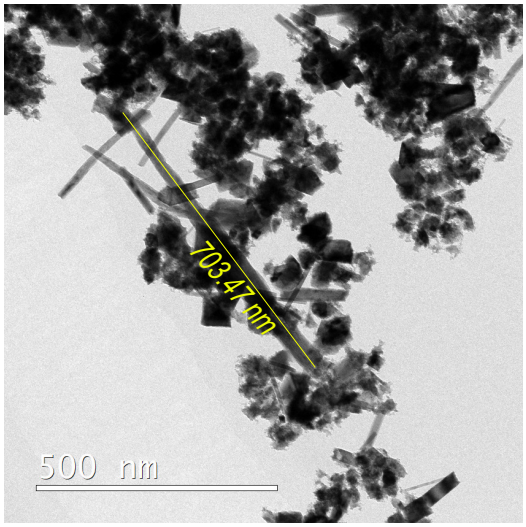

Figure 15: BF-TEM image of sample $hIrO_2$, showing measured length of longest needle shaped NP for the given site. Displayed as an yellow line, with respective length, 703.5nm, below.

can be seen in the BF-TEM image shown in Fig. 15. As shown in 15, the longest needle is measured to be 703.5 nm. Shorter ones had lengths ranging between 188.8±41.4 nm. The crystals were of a broad variety of shapes and sizes.

5.2.2 $IrNi_x$ Alloy Nanoparticles

$Ox-A-IrNi_2$

All figures showing EDX, SEM and TEM results for sample $Ox-A-IrNi_2$ are presented in Appendix C.1. A BF-TEM image with overview and histogram of sample $Ox-A-IrNi_2$, which was synthesised with oxygen present, is presented in Fig. 35a. In Fig. 35b a SEM-EDX image of the same area as in Fig. 35a is shown.

In the overview, Fig. 35a, the sample is shown to consist big dendrite shaped particles around ∼30-40 nm. It was difficult to identify size distribution due to ambiguous particle boundaries, a result of rapid particle growth. Overall, the particles did not form spherical-like clusters, but instead stayed together as long chains. The map scan in Fig. 35b shows alloy particles with higher concentration of Ni in the middle. However, no line scans showed core-shell structures.

A−$IrNi_2$

In Fig. 16a, BF-TEM image of sample A−$IrNi_2$ is shown together with respective histogram for that given site. A DF-TEM image of a particle from that particular site is presented in Fig. 16b. Resulting particles in Fig. 16a showed

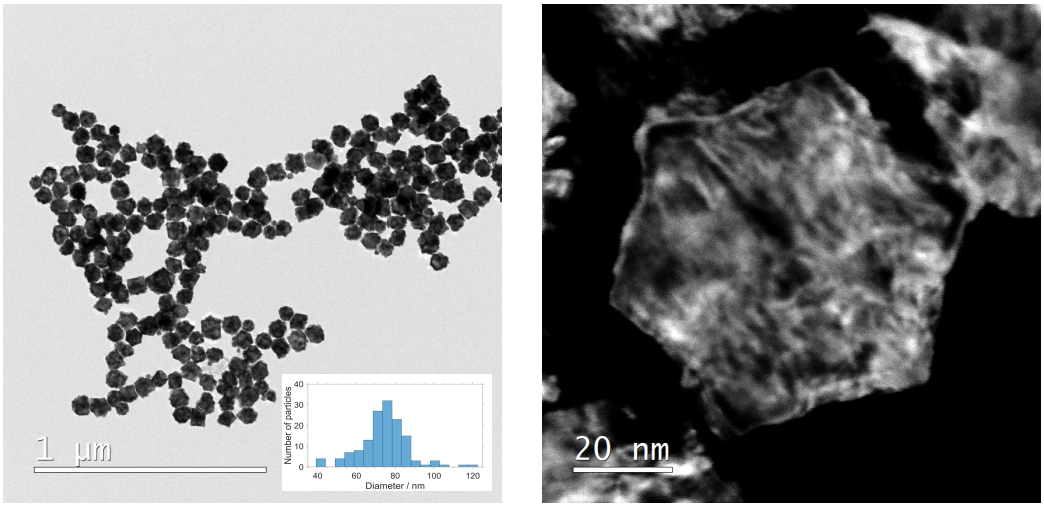

(a) **(b)**

Figure 16: BF and DF-TEM results for sample A−$IrNi_2$. a) Shows BF-TEM image with overview over catalyst clusters for a given site, including the respective histogram. b) Close up DF-TEM image of particle from the same site as in a).

much more defined particle surfaces than the previous sample, Ox−A−$IrNi_2$. No formation of dendrites could be seen, but irregularities in the shapes were present. Majority of particles had star (as seen in Fig. 16b), irregular and pentagonal shapes, and had an overall broad particle size distribution. They ranged between ∼38-125 nm, with the majority between ∼60-80 nm. Overall, the sample did not appear to agglomerate or aggregate much.

Regarding SEM-EDX for this sample, no sign of core-shell-formation could be seen, as both the map scan and linear-scan showed homogeneously spread Ir and Ni atoms throughout the particles, resulting in an alloy structure. After dealloying, new TEM and SEM-EDX imaging were done on A$-IrNi_2$. DF-TEM image and SEM-EDX map scan are shown in Fig. 18. The corresponding normalised EDX-line scan for map scan are shown in Fig. 17

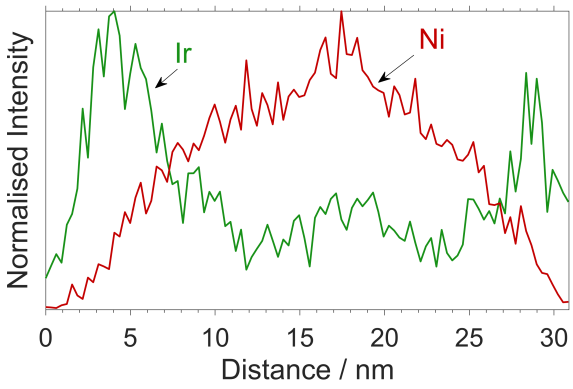

Figure 17: Normalised line scan for A$-IrNi_2$ after dealloying. Red line represents Ni-core and green line represents Ir-shell.

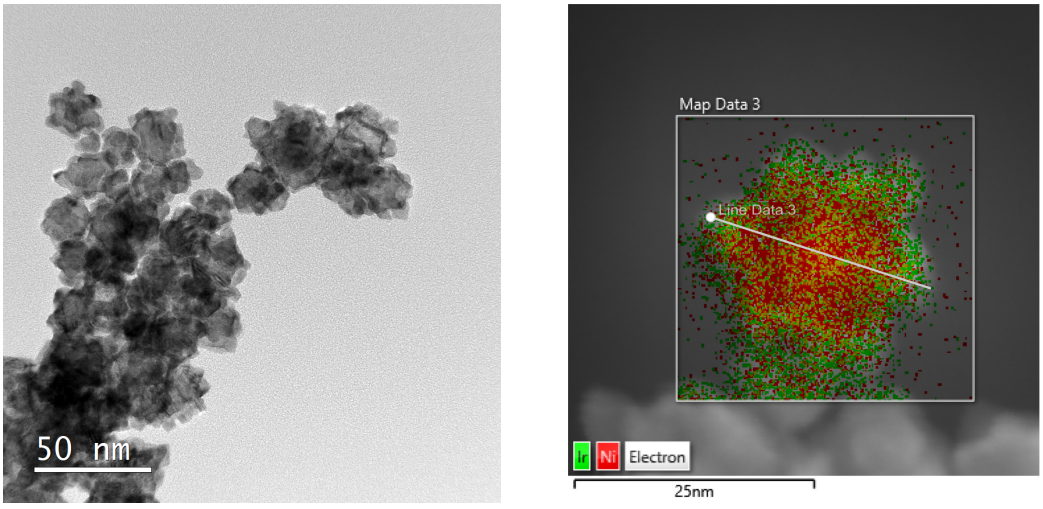

(a) **(b)**

Figure 18: BF-TEM results for sample A$-IrNi_2$ after dealloying. a) Shows BF-TEM image with overview for a given site and b) shows SEM-EDX map scan. Corresponding EDX-line normalised scan are shown in Fig. 17

After dealloying, the surfaces of the particles became less uniform and controlled, as seen in Fig. 18a. There was also formation of dendrites and non-distinctive shapes. Nevertheless, Ir had segregated to the surface through dealloying and formed CS-structures, as is seen for both the map and normalised line scan Figs. 18b and 17. Other mappings at this site showed structures constructed with mainly Ir and small amount of Ir in core. From the line scan we can tell that the Ir-shell thickness achieved were at ∼4 nm and ∼7 nm.

A−$IrNi_3$

With lower Ir to Ni ratio, less dendritic growth occurred. Smaller particles were formed, but size distribution was still broad, where the particles ranged between ∼6-33 nm Agglomerates and clusters were more prevalent in this sample compared to the previous $IrNi_2$-samples before and after dealloying. Images for this sample are presented in Fig. 36 in Appendix C.1. Element mapping showed formation of alloy and cluster-structures. There was no observation of CS-structures in the SEM-EDX images before dealloying.

A−$IrNi_5$

For A−$IrNi_5$ bigger clusters were formed, with less stand alone particles compared to latter alloy-samples. Thus, a size distribution was difficult to acquire. An overview of the sample including a size histogram is displayed in Fig. 19c.

The shape of particles of sample A−$IrNi_5$ were smaller, and achieved more defined shapes than the previous A−$IrNi_x$-samples. Some formation of big particles were observed (not shown in this image). Star shaped particles were formed, but with no well defined surface lines. Multiple line scans for this sample showed formation of CS-structures. An example is presented in Fig. 19. The line scan (Fig. 19b) includes a SEM image of the scanned particle (Fig. 19a):

As seen in Fig. 19a, we were able to synthesise CS-morphology for the A−$IrNi_5$-sample. The last one showed an equal distribution of both metals. The SEM image shows star shaped particles (concave octahedrons) as well.

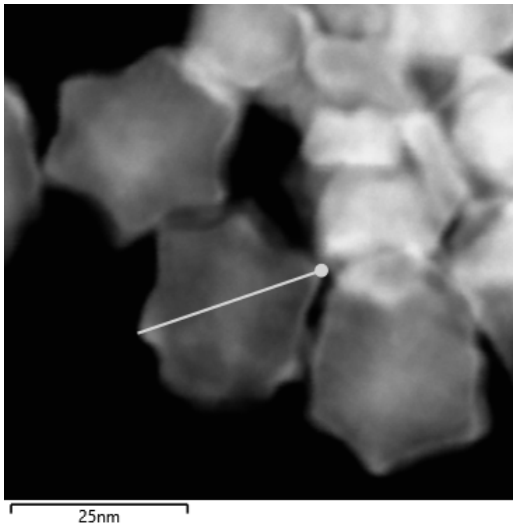

(a) SEM image of scanned particle.

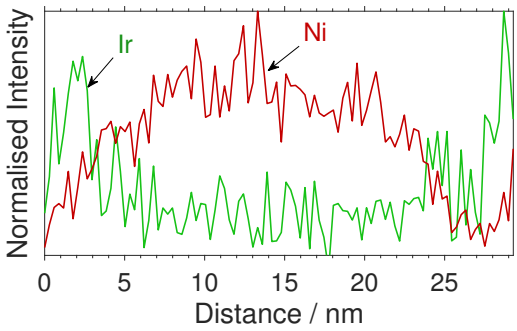

(b) Line scan of scanned particle

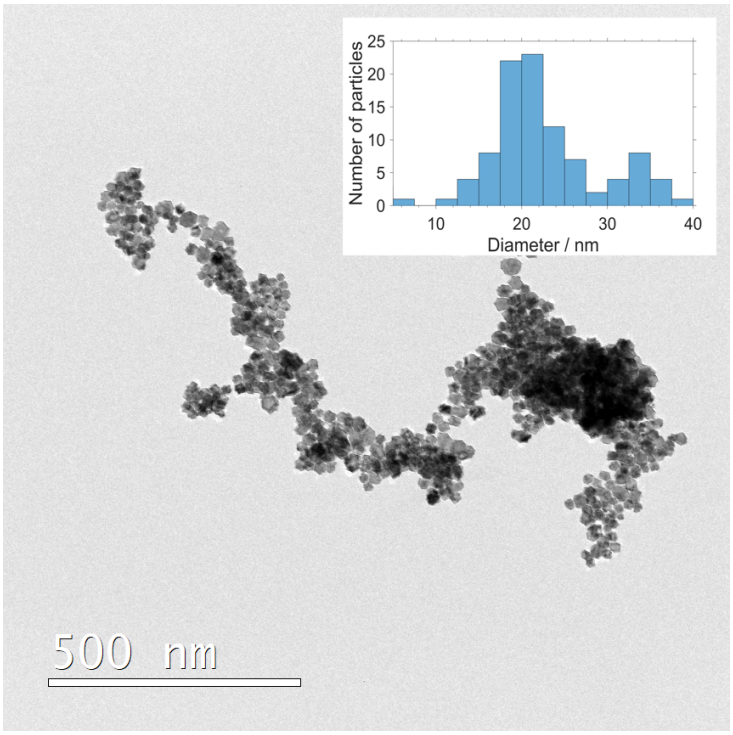

(c) BF-TEM image of sample A−$IrNi_5$ including respective histogram for the given site.

Figure 19: SEM image of scanned particle from sample A−$IrNi_5$ is shown in a), including line drawn. b) Normalised line scan for the scanned particle. Green line is expresses as Ir, and red as Ni-metal.

5.2.3 $IrNi_x$ Core-Shell Nanoparticles

CS−$IrNi_x$-Nanoparticles without TOP

Ox−CS−$IrNi_2$

The particles in sample Ox-CS-$IrNi_2$ clumped together into big clusters. Their shapes were irregular, often seen as stars, or with non-distinctive shapes and agglomerates. The star-shaped particles can be described as concave octahedrons[10], with an example of the shape in Fig. 20b. An overview of the given site in Fig. 20b with the respective size distribution histogram is presented in Fig. 20a. As expected, with uncontrolled growth the BF-TEM image and histogram showed a broad size distribution ranging between 10-72 nm sized particles. SEM-EDX map scans were also taken, which showed no distinct core-shell structure, as Ir had placed itself at edges and corners.

CS−$IrNi_2$

Poor control of shape, morphology and size could also be seen for CS−$IrNi_2$, synthesised without oxygen present. Concave octahedrons and octahedrons with hollow or near-hollow structures were obseved. A near-hollow octahedron can be seen in the SEM image, shown in Fig. 21a, and the corresponding EDX-line scans in Fig. 21b for this sample. We can observe both Ir and Ni at the surface, with declining amounts toward the centre. Few particles had core-shell structures.

An overview of a given site for this sample is presented in Appendix C.1.1 Fig. 37, including a histogram of particle size distribution for that site. It shows a fairly broad distribution with particles ranging between 4-43 nm, where a majority of particles lie in range of 15-25 nm. Other shapes which can be observed are triangular shapes and nanocubes.

CS−$IrNi_3$

With increasing Ni:Ir molar ratio, more defined shapes and a narrower size distribution were obtained. For samples with 2:1 ratio, the particles clustered

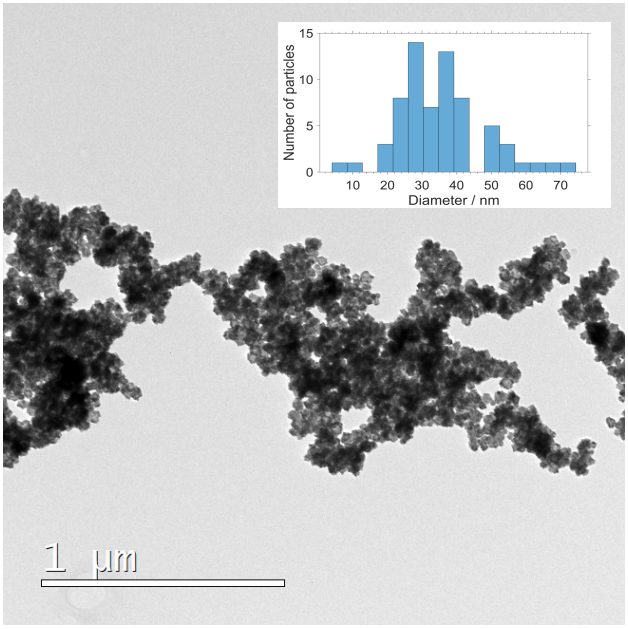

(a)

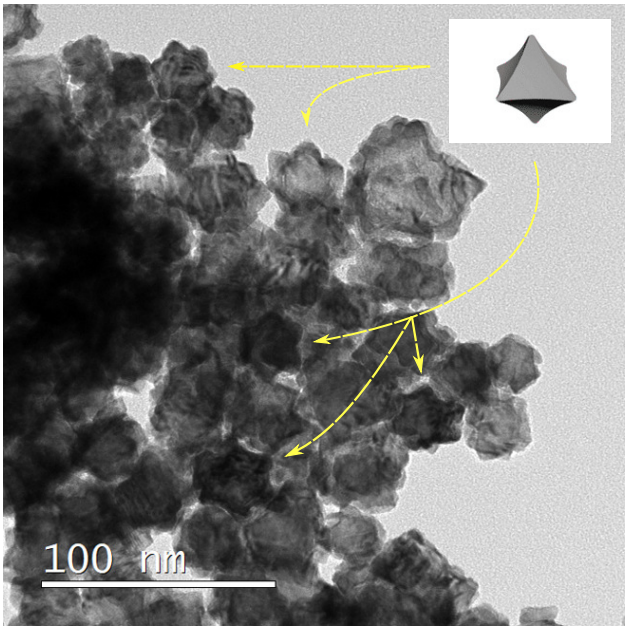

(b)

Figure 20: BF-TEM overview images for sample Ox−CS−$IrNi_5$ with including histogram in a), and concave octahedrons denoted with yellow dashed arrows in b). Both images are taken at the same site.

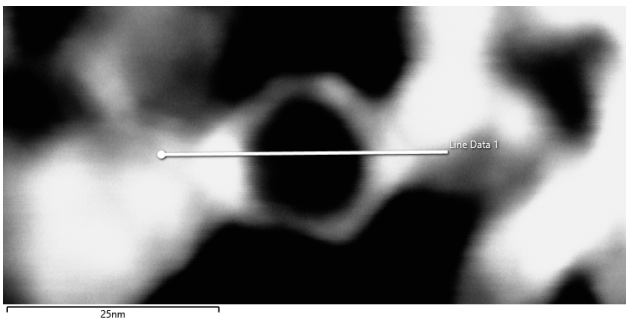

(a) Line drawn for line scan of CS−$IrNi_2$ NPs. Overview of particles can be seen in Figure (XX).

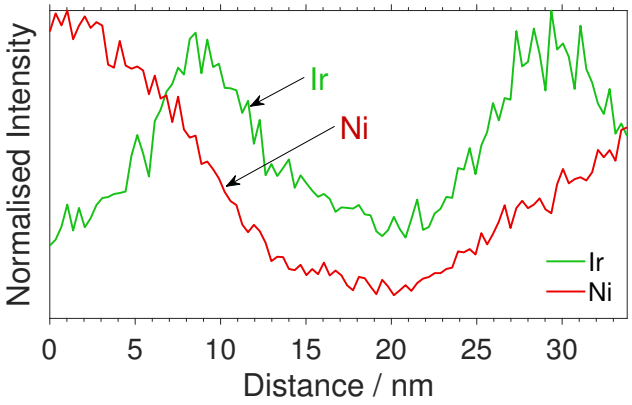

(b) Normalised line scan diagram for sample CS−$IrNi_2$.

Figure 21: SEM image of near-hollow sample CS−$IrNi_2$ is shown in a) The drawn line corresponds to the normalised EDX-line scan in b). is s Overview of particle from sample CS−$IrNi_2$ with line drawn for SEM-EDX line profile with corresponding normalised line scan.

themselves together into big clusters, while for CS−$IrNi_3$, the particles were more separated with stand alone particles. Particle sizes, shown in Fig. 22c, ranges between 5-23 nm in diameter. Formation of large irregular coalesced particles are shown in the figure, together with smaller more well defined hexagonal ones. The SEM image in Fig. 22a, we can see a close up of the hexagonal shaped CS−$IrNi_3$. The line drawn corresponds to the normalised EDX-line scan in Fig. 22. The hexagonal particles shown in the SEM image is a truncated octahedron morphology, and respective line scans presented show a an almost CS-structure. Other sites and particles from the CS−$IrNi_3$-sample, did show CS-morphologies.

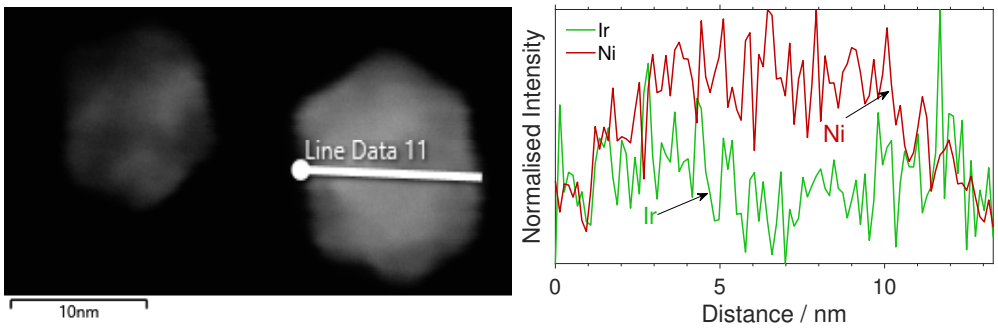

(a) **(b)**

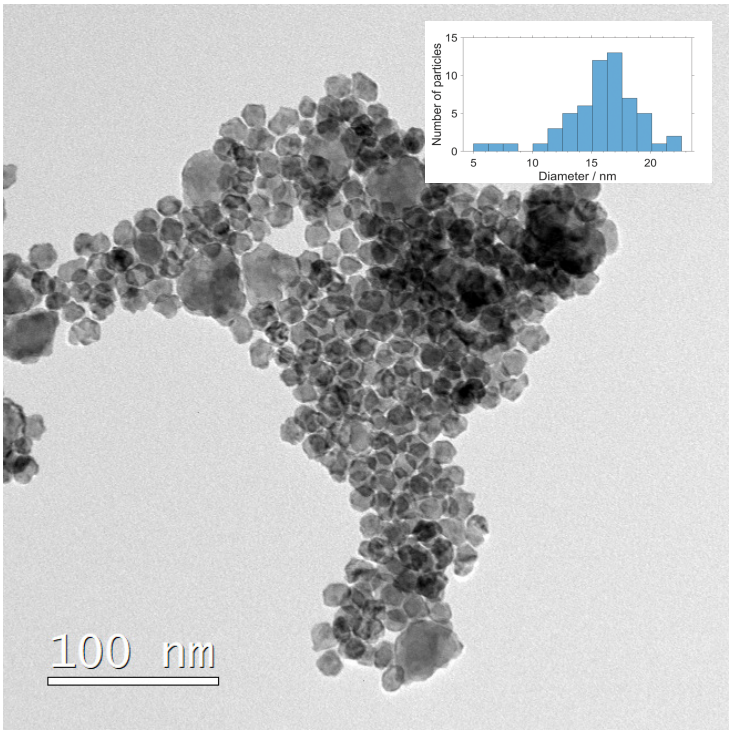

(c) BF-TEM image of sample CS−$IrNi_3$ showing with including histogram over given site.

Figure 22: SEM-image in a) shows particles from sample CS−$IrNi_3$ with line drawn for corresponding normalised SEM-EDX line profile shown in b)

CS−$IrNi_5$

According to TEM and SEM images of CS−$IrNi_5$, the particles tend to place themselves in small clusters, compared to the previous CS−$IrNi_x$-samples. The site presented in BF-TEM Fig. 23, shows one of few sites with a large amount of particles that we were able to find in in one cluster. The histogram

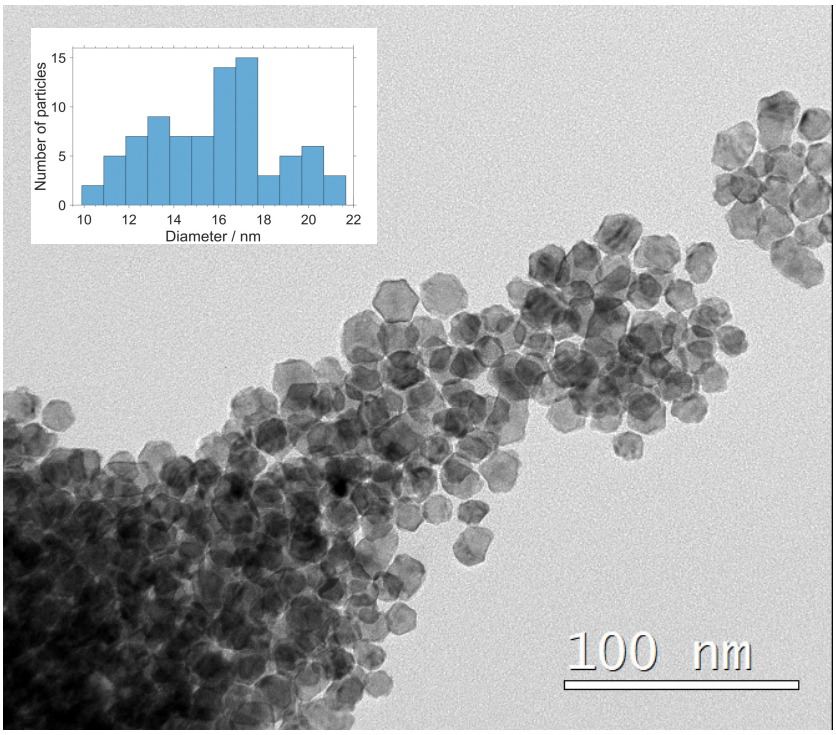

Figure 23: BF-TEM image of sample CS−$IrNi_5$ showing cluster with particles. Including histogram over given site.

shows a broad size distribution, with particle diameters between 10-22 nm. One particle had a diameter down to 8 nm and two up to 24 nm at other sites. Particles were quite uniform and had defined shapes, however as in the previous sample agglomeration and formation of big particles. From the BF-HRTEM-image shown in Appendix C.1, Fig. 38, see formation of hcp phased Ni. SEM-image for sample CS−$IrNi_5$ with corresponding line scans can be seen in Fig. 24. The figure shows a particle scanned with line drawn (Fig. 24a) and the given normalised line scan (Fig. 24b). Scale bar is shown to be 25 nm, whereas the particle diagonal is measured to be 20.54 nm. Each side of the particle had a length between 9.3-10.5 nm. The particle in this figure shows an even more defined truncated octahedron shape, and the

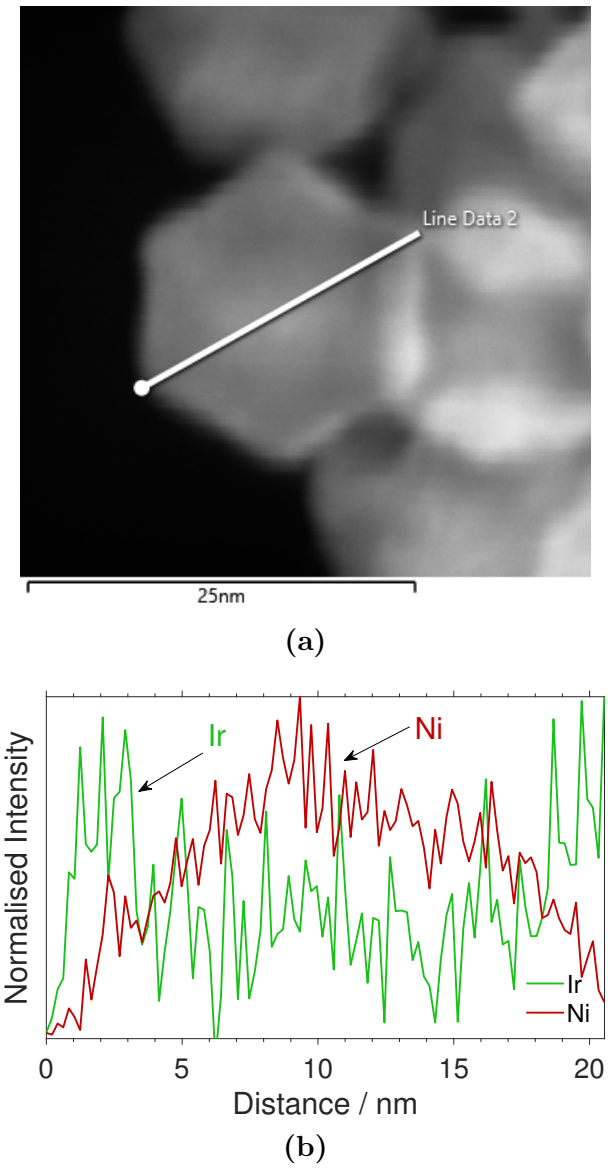

Figure 24: SEM-image of CS−$IrNi_5$-sample is shown in a), with corresponding normalised EDX linecan in b). With green line that is denoted as Ir and red line as Ni.

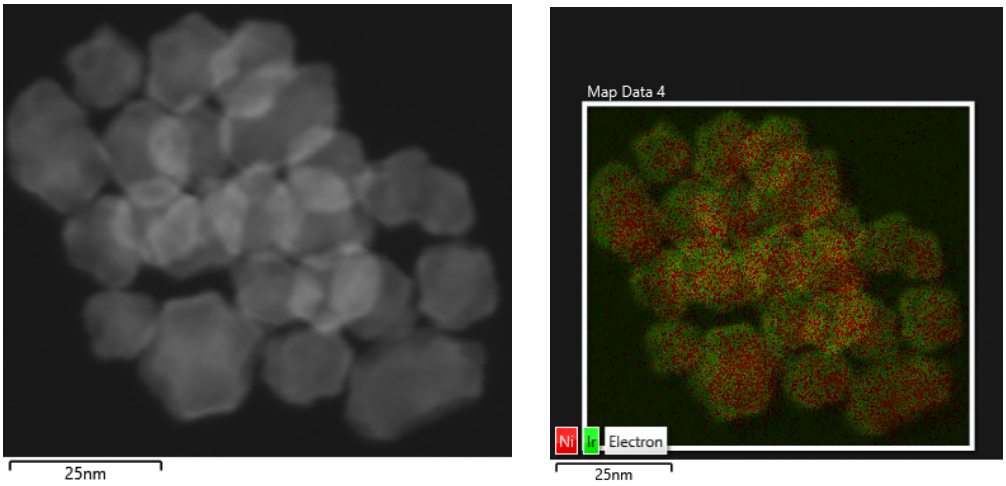

(a) An overwiev of cluster for map scan. **(b)** Map scan. Red dots are Ni and green are Ir. The scan shows some drifting.

Figure 25: SEM-EDX profile for sample CS−$IrNi_5$, including an overview of the cluster.

diagonal line scan reveals the particle had achieved a core shell structure. Ir-shell thickness was approximately 3 nm on each side, and a Ni-core of circa 15-16 nm. Ni content increases into the centre of the particle. EDX mapping with a close up of the same area as in Fig. 24, resulted in the scans shown in Fig. 26.

The EDX-map scans in Figs. 26b, 26c and 26c shows that the particle obtained a core-shell structure, as Ni and Ir can easily be discerned from each other by the red and green colours respectively. An overview of particle cluster including corresponding EDX-map scan can be seen in Fig. 25.

The images were taken at a different site than the particle shown in Fig. 26a. There were some difficulties with drifting and charging effects as shown in the map profile in Fig. 25b, with some drifting south-eastwards. However, the overall view shows that the particles in the cluster were are all of core-shell structure.

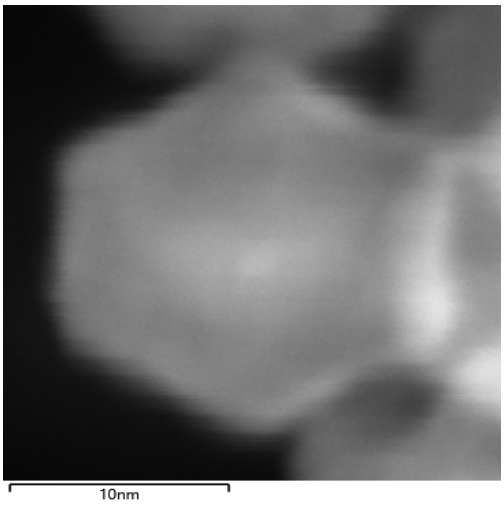

(a)

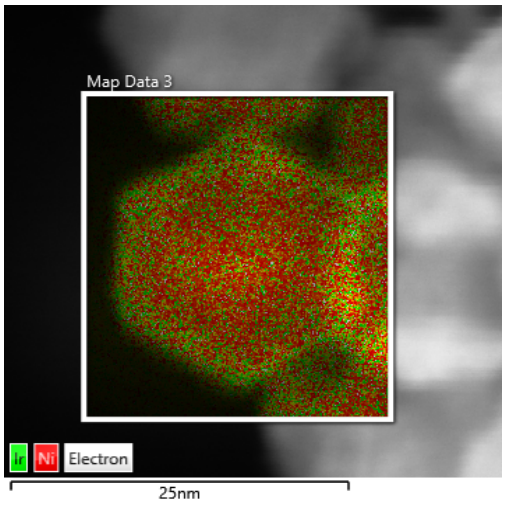

(b) EDX-map scan of CS−$IrNi_5$

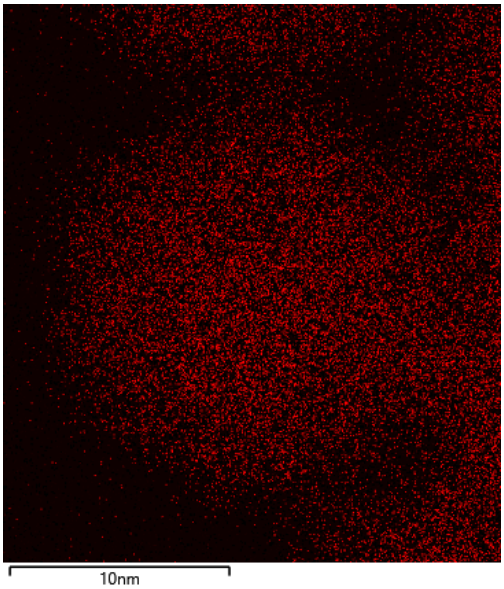

(c) Separate scan for Ni.

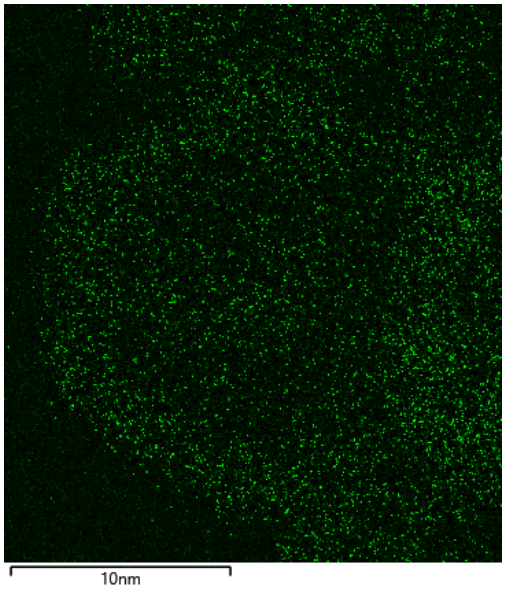

(d) Separate scan for Ir.

Figure 26: SEM-image of sample CS−$IrNi_5$ is shown in a) with the corresponding SEM-EDX map profile for Ir and Ni in b). Separate scans of Ir and Ni are shown in c) and d), respectively. Red maps is denoted as Ni and green as Ir.

CS−$IrNi_x$-Nanoparticles with TOP

$T_{0.2}$−$IrNi_2$

A BF-TEM image of sample $T_{0.2}$−$IrNi_2$ is shown in Appendix C.1.1, Fig. 39. The TEM image shows an overview of the particles, which have a size distribution of ∼2-8 nm, with a majority at ∼6 nm. By comparing the size distribution with the corresponding CS−$IrNi_2$ sample synthesised without TOP, it was observed that the size distribution was reduced drastically. Even for the low TOP:OAm ratio. The shape of the $T_{0.2}$−$IrNi_2$-particles was as expected more controlled than the other $IrNi_x$-samples, with narrow shape distribution close to spherical surface.

Due to small particle sizes, the shapes of particles are difficult to discern. Regarding EDX scan, almost no Ir can be observed either in map scans or line scans. Because of small particle sizes the sample had problems with charging effects and drifting during characterisation, both before and after washing the sample with laser.

$T_{0.1}$−$IrNi_2$

No significant changes in structures compared to $T_{0.1}$−$IrNi_2$, regarding shape and size distribution. could be observed when reducing the TOP:OAm molar ratio to 1:9. SEM-EDX images showed low to almost no amount of Ir on surfaces.

$T_{0.05}$−$IrNi_2$

Compared to the previous two samples synthesised with TOP, the particles were more irregular shaped, and the size distribution broader. The particles ranged between 4-9 nm in diameter. DF-TEM image of $T_{0.05}$−$IrNi_2$ can be seen in Appendix C.1, Fig. 40. The reduced amount of TOP added lead to poorer growth control, but the amount of the capping agent was enough to also inhibit Ir growth to some degree. No great changes in structures, only some particles are deviating from thermodynamic shape and are less controlled as the TOP-samples with higher ratio of TOP to OAm. As the previous samples with TOP, only low amount of Ir can be observed from

EDX map and line scans.

5.3 CV and LSV

All electrochemical measurements were proceeded in 0.5 mol dm^{-3}H_2SO_4, in an N_2-atmosphere. LSV measurements were proceeded with a rotation speed of 1600 rpm and sweep rate of 5 mV min, for all samples. All CVs were measure at a sweep rate of 150 mV s^{-1} The GC-electrodes had a geometrical surface area of 0.196 cm^2.

5.3.1 AIROF and hIrO$_2$

Oxide growth on the bulk Ir-electrode (AIROF) was done as described in Section 4.1.1, resulting in the cyclic voltammogram shown in Fig. 27.

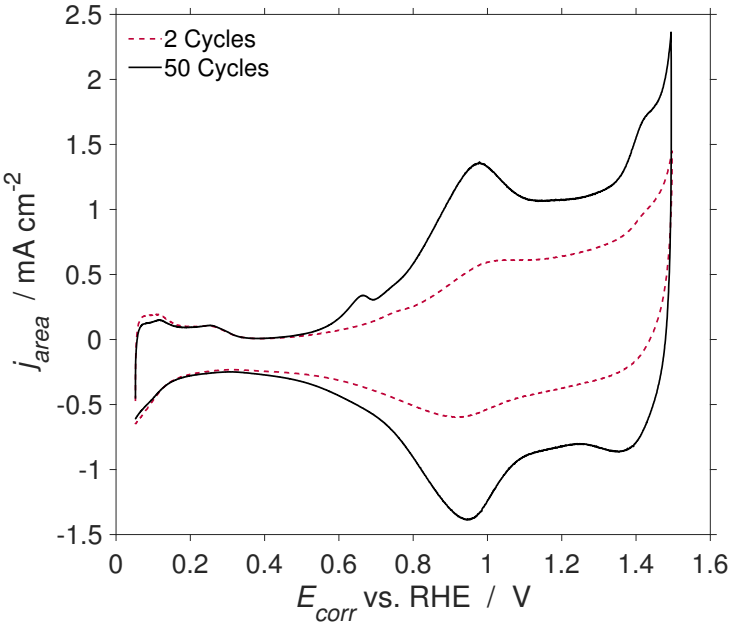

Figure 27: jR-corrected CV of bulk Ir-electrode after 2 and 50 cycles. The sweep rate was set to be 150 mV s^{-1}.

After two cycles no prominent peaks can be seen, as no irreversible oxide multi-layer had yet been formed.[60] However, after 50 cycles, anodic peeks in oxide area can be seen at ∼0.77 V and ∼0.99 V, in which OER begins at

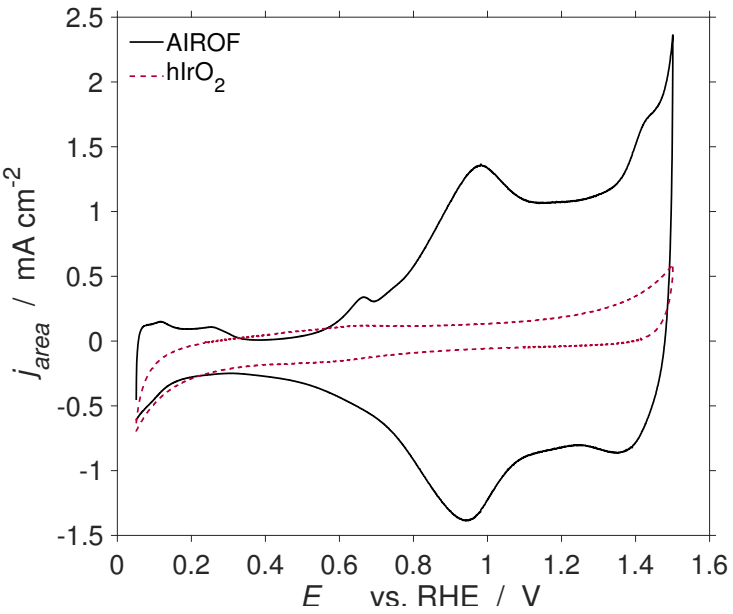

Figure 28: jR-corrected CV of AIROF after 50 cycles, compared to 1.st. cycle for $hIrO_2$, with a loading equal to $31\,\mu g\,cm^{-2}$. A sweep rate of $150\,mV\,s^{-1}$ was used. AIROF is noted with black solid line, and $hIrO_2$ is noted with red dashed line.

around 1.45 V, with a pre-peak at 1.38 V. The resulting voltammogram for AIROF is in agreement with previous results found by others.[61]

By cycling further until at least 200 cycles, formation of hydrated IrO_x-layers could be observed by the colour change from a transparent metallic colour into a blue-black colour. Transparent colour corresponds to lower oxidation states of Ir [Ir(II) or Ir(III)], while the coloured state shows a higher oxidation state [Ir(IV)].[61] By sweeping the electrode between 0.05-1.4 V, and preventing further growth or reduction of the thickness, the same colour change could be observed. A comparison between the CVs of AIROF after 50 cycles and non-cycled rutile structured $hIrO_2$ catalyst can be seen in Fig. 28. The CV are presented with $hIrO_2$ as red, dotted line and AIROF with black solid line. $hIrO_2$ shows less defined peaks than AIROF, with only one anodic peak that appears at 0.68 V, which is not consistent with the anodic peaks of AIROF. However, on-set potential for OER begins at the same potential as for AIROF. This indicates that AIROF and $hIrO_2$ had a different surface morphology.[62]

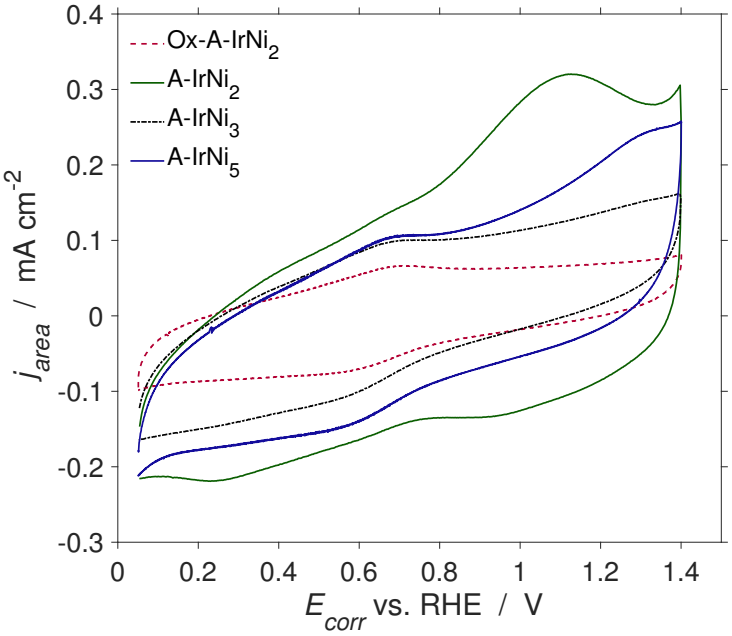

Figure 29: jR-corrected CVs of all Alloy-samples combined, after dealloying and oxidation of catalysts. Red dashed line is equal to Ox−CS−$IrNi_2$, green solid as CS−$IrNi_3$, black dotted as CS−$IrNi_3$ and blue solid line as CS−$IrNi_5$. The CVs were measured at 150 m V s^{-1}.

5.3.2 $IrNi_x$ Alloy Nanoparticles

CVs for all alloy NPs are presented in Fig. 29. All CVs were sampled at 150 mV s^{-1} and had a loading equal to ∼25 µg cm^{-2}. Loading for each sample is presented in Section 4.1.6, Table 1. All samples gave similar CVs with the exemption of A−$IrNi_2$, therefore indicating a different structure than rest of the dealloyed catalysts. Ox−A−$IrNi_2$, A−$IrNi_3$ and A−$IrNi_5$ all have quite similar CVs as hIrO_2, where Ox−A−$IrNi_2$ is the most similar. Only difference that can be observed is a higher current density, including no H-adsorption peak. With reduction of Ir, an increase in current density can be seen for A−$IrNi_3$ and A−$IrNi_5$. The anodic peak at 1.08 V seen for A−$IrNi_2$ can be assumed to be the irreversible formation of porous oxides, IrO_2. With a possible IrO_2 stripping peak at 0.98 V, with low current density compared to the adsorption peak.[63] Cathodic peak right above 0.23 V can be possible dissolution of Ni.[63] Corresponding polarisation curves for A−$IrNi_x$-samples can be seen in Fig. 30. Polarisation curves for alloy samples do not follow any trend. Where mass activity for A−$IrNi_2$ is higher than A−$IrNi_5$ after 1.5 V. We can see for the charge activity for A−$IrNi_2$ is further increased compared

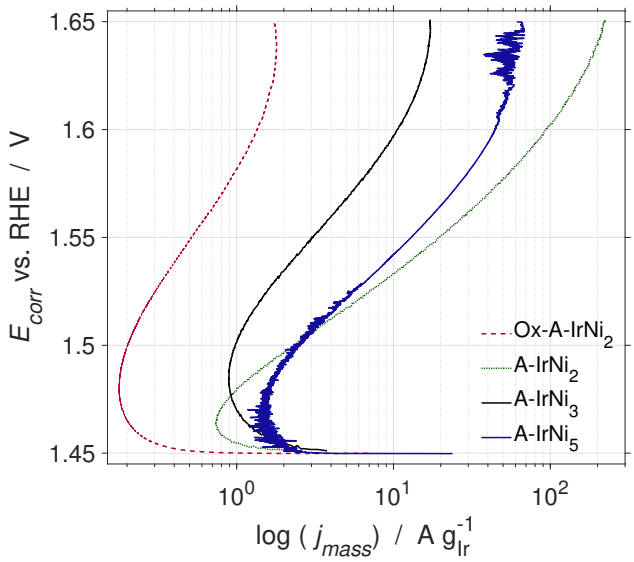

(a) Normalised with regards on mass Ir

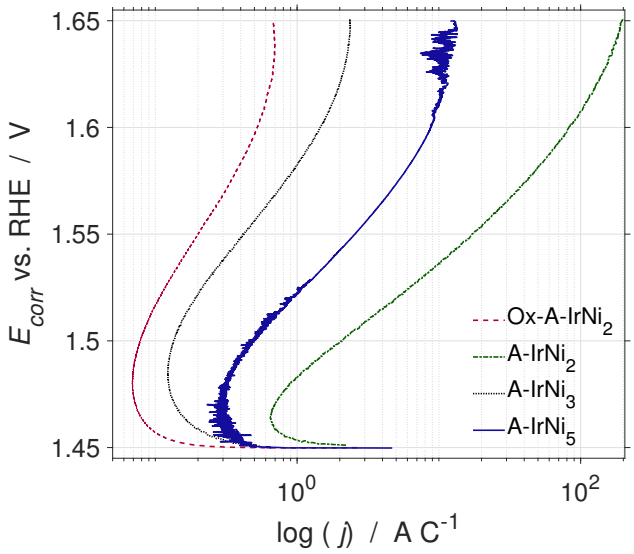

(b) Normalised with regards on charge

Figure 30: Combined, normalised and jR-corrected polarisation curves for A$-$IrNi$_x$-samples. A sweep rate of 5 mV min were used.

to A−$IrNi_5$, and achieved the highest activity for all of the samples. In Table 3 values for the Tafel slope are presented for the slopes normalised with regards to mass in Fig. 30b. Together with Tafel slopes the mass activities and charge activities for each A−$IrNi_x$-samples are presented. The activities were found at 1.525 V. The electrochemically active surface area ECSAwas also found at this potential value.

Table 3: Tafel slopes for all A−$IrNi_x$samples. Ir mass and charge activities were measured at 1.525 V. From the normalised activities ECSA could be found.

Sample	**b** $mVdec^{-1}$	**Mass Activity** Ag_{Ir}^{-1}	**Charge Activity** AC^{-1}	**ECSA** $m^2g_{Ir}^{-1}$
Ox−A−$IrNi_2$	102	0.3	0.12	26
A−$IrNi_2$	69	7.12	6.27	33
A−$IrNi_3$	91	1.57	0.22	39
A−$IrNi_5$	79	5.71	1.10	43

From table 3 we can see that mass activity for A−$IrNi_2$ was lower at 1.525 V than for A−$IrNi_5$, as the slopes had not crossed each other yet. A−$IrNi_2$ achieved the highest activity with regards on charge, but not the highest specific active surface area. The sample with highest active surface area was A−$IrNi_5$.

5.3.3 $IrNi_x$ Core-Shell Nanoparticles

Without TOP

Before oxidising the catalysts, they were cycled in 0.1 mol dm^{-3} KOH to see if there was any Ni present on the surface of the particles. All samples except CS−$IrNI_5$ showed initial respons for Ni-β-OOH.[64] Resulting in better coverage of Ir for CS−$IrNI_5$-sample. Combined voltammogram recordings for all the CS−$IrNi_x$-samples, after being oxidised, can be seen in Fig. 31. All samples had a catalyst loading between 25-31 µg cm^{-2}, with their exact values presented earlier in Section 4.1.6, Table 1. Both CS−$IrNi_2$ and CS−$IrNi_3$ have similar voltammograms, with only higher current density for CS−$IrNi_3$. Two possible overlapping, broad anodic peaks can be seen beginning from 0.3 V and ends at circa 0.73 V. In H-region, region below 0.7 V, the peaks might consist of H-desorption peak. Because of visible H-adsorption peak

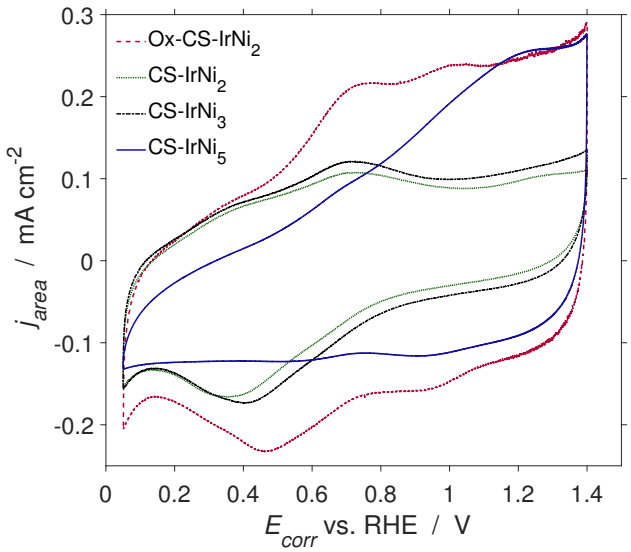

Figure 31: jR-corrected CVs of all CS−$IrNi_x$-samples combined, after oxidation of catalysts. Red dashed line is equal to Ox−CS−$IrNi_2$, green dotted as CS−$IrNi_3$, black dotted as CS−$IrNi_3$ and blue solid line as CS−$IrNi_5$.

below 0.2 V. Furthermore, the cathodic peaks at 0.43 V signifies stripping of surface hydroxide or oxide ($Ir(OH)_x$ or IrO_x).[63]

No well defined peaks can be seen for CS−$IrNi_5$, even in the low potential region for H-adsorption and desorption. Between 0.6-1.37 V there may be a combination of more peaks, with two possible discernible peaks at 0.69 V and 1.16 V. The 1.16 V can be due to irreversible formation of porous IrO_2, with no cathodic peak signifying stripping of porous IrO_2.[63] By comparing the four CS-samples, only CS−$IrNi_2$ and CS−$IrNi_3$ had similar CVs, indicating similar same surface composition and morphology.

Polarisation curves for CS−$IrNi_x$-samples can be seen in Fig. 32. The red dashed line represents Ox−CS−$IrNi_2$, green dotted line is CS−$IrNi_2$, black solid line is CS−$IrNi_3$ and blue solid line as CS−$IrNi_5$.

LSV for CS−$IrNi_x$-samples show that the activity of samples synthesised inside the glove box follow a trend; by reducing the ratio of shell-metal Ir to core-metal Ni, the mass activity increases. For charge activity this is also the case. However, CS−$IrNi_2$ are close to CS−$IrNi_3$ in activity. All samples had almost identical values for Tafel slope. The values for Tafel slope, including mass and charge activities at 1.525 V, and electrochemical active surface area (A_{ECSA}) are presented in Table 4

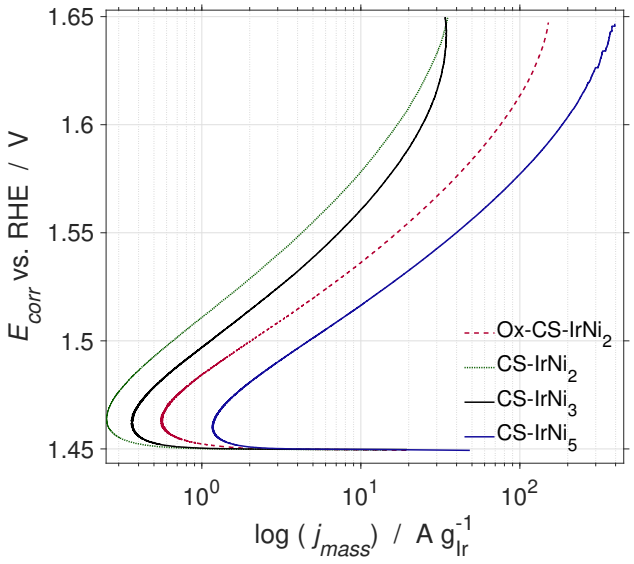

(a) Normalised with regards on mass Ir

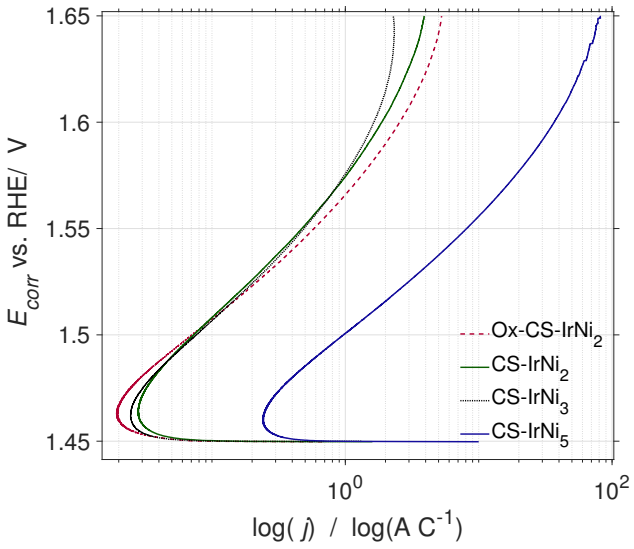

(b) Normalised with regards on charge

Figure 32: Combined, normalised and jR-corrected polarisation curves for CS−IrNi$_x$-samples. A sweep rate of 3 mV min and rotation of 1600 rpm was used.

Table 4: Tafel slopes for all CS−$IrNi_x$-samples. Including Mass and specific activities and ECSA, that were found at 1.525 V

Sample	b $mVdec^{-1}$	Mass Activity Ag_{Ir}^{-1}	Charge Activity AC^{-1}	ECSA $m^2g_{Ir}^{-1}$
Ox−CS−$IrNi_2$	51	6.28	0.22	31
CS−$IrNi_2$	64	1.74	0.21	21
CS−$IrNi_3$	64	3.09	0.19	54
CS−$IrNi_5$	61	14.23	2.28	64

All CS−$IrNi_x$-samples achieved a Tafel slope of around 50-60 $mV\,dec^{-1}$, implying similar reaction mechanisms. CS−$IrNi_5$ achieved the highest activity, both with regards on mass and charge, with 14.23 $A\,g_{Ir}^{-1}$ and 2.28 $A\,C^{-1}$, respectively measured at 1.525 V. It also achieved highest value for active surface with 64 $m^2\,g_{Ir}^{-1}$.

With TOP

Results from electrochemical measurements for CS-syntheses with TOP present can be seen in Appendix C.1.2, where Fig. 42 shows the cyclic voltammograms and Figs. 43a and 43b presents the normalised polarisation curves.

From the EM results we could see poor to almost no coverage of Ir on the Ni-particles. Nevertheless, for electrochemical measurements we can see some response of Ir for all TOP samples. All CVs show similar responses, whereas it is $T_{0.05}$−$IrNi_2$, shown as red dashed line in Fig. 42, that achieved highest current density. The voltammetric responses for TOP samples were low in terms of current densities, but shape of the voltammogram were quite similar to all alloy-samples except A−$IrNi_2$, and similar to CS−$IrNi_2$ and CS−$IrNI_3$. Implying that there were Ir at the surface.

Regarding activity, the sample synthesised with highest content of TOP, $T_{0.2}$−$IrNi_2$, acquired highest mass activity. The same goes for charge activity. In Appendix C.1.2 Table 9, Tafel slopes for each sample are shown, where all samples gave different values. Sample $T_{0.2}$−$IrNi_2$, that achieved highest activities had lowest value for Tafel, with 88 $mV\,dec^{-1}$. Sample $T_{0.1}$−$IrNi_2$ achieved highest A_{ECSA}, but lowest value for both mass and charge activities, compared to all samples overall.

Table 5: Summary of Tafel slopes, Ir mass and specific activities and A_{ECSA} for all synthesised samples. Values were found at 1.525 V

Sample	b $mVdec^{-1}$	Mass Activity Ag_{Ir}^{-1}	Charge Activity AC^{-1}	ECSA $m^2g_{Ir}^{-1}$
$hIrO_2$	48	2.68	0.05	40
$Ox-A-IrNi_2$	102	0.3	0.12	26
$A-IrNi_2$	69	7.12	6.27	33
$A-IrNi_3$	91	1.57	0.22	39
$A-IrNi_5$	79	5.71	1.10	43
$Ox-CS-IrNi_2$	51	6.28	0.22	31
$CS-IrNi_2$	64	1.74	0.21	21
$CS-IrNi_3$	64	3.09	0.19	54
$CS-IrNi_5$	61	14.23	2.28	64
$T_{0.05}-IrNi_2$	381	0.29	0.12	20
$T_{0.1}-IrNi_2$	381	0.54	0.05	138
$T_{0.2}-IrNi_2$	88	1.19	0.16	32

5.3.4 $hIrO_2$, $A-IrNi_2$ and $CS-IrNI_5$

A comparison of polarisation curves of samples achieving highest activity from the three different syntheses routines, can be seen in Figs. 33a and 33b. Due to poor results for the TOP-synthesis, they are not included in this presentation. Black dotted line denotes polarisation curve for $hIrO_2$, blue solid line as $A-IrNi_2$ and red dashed line as $CS-IrNi_5$.

In 33a we can see that $CS-IrNi_5$ obtained highest mass activity throughout the whole potential window. The sample with highest charge activity by all samples were $A-IrNi_2$. A comparison with $A-IrNi_5$ was also done because of its core-shell structure, and the polarisation curve is presented in Appendix C.1.2, Fig. 41. Sample $CS-IrNi_5$ achieved highest mass activity for all potentials, and $A-IrNi_5$ achieved highest charge activity for all potentials.

In Table 5 a summary of Tafel slopes, catalytic activities and ECSA, measured at for all samples is presented. Because of too low values for catalytic activities. Highlighted rows in the table are values for the samples presented in Fig. 33. Tafel slope for $hIrO_2$ is equal to 48 mV dec^{-1}, as expected for rutile structured IrO_2, but much lower expected value for mass activity. Overall, the core-shell $CS-IrNi_5$-sample obtained highest activity, both mass and charge

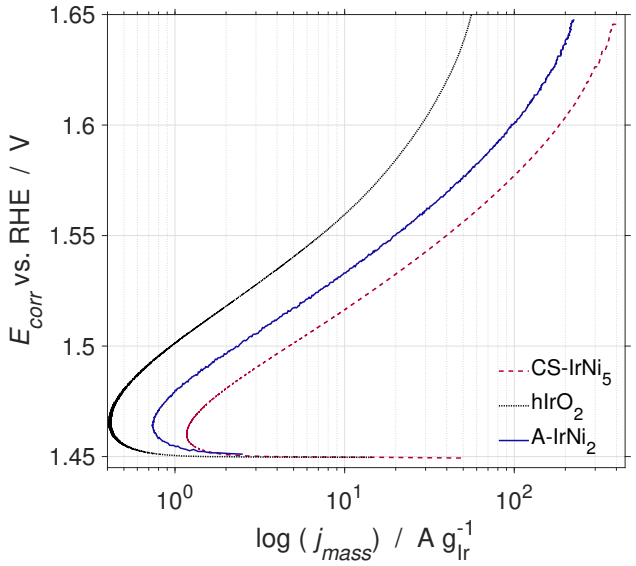

(a) Normalised with regards on mass Ir

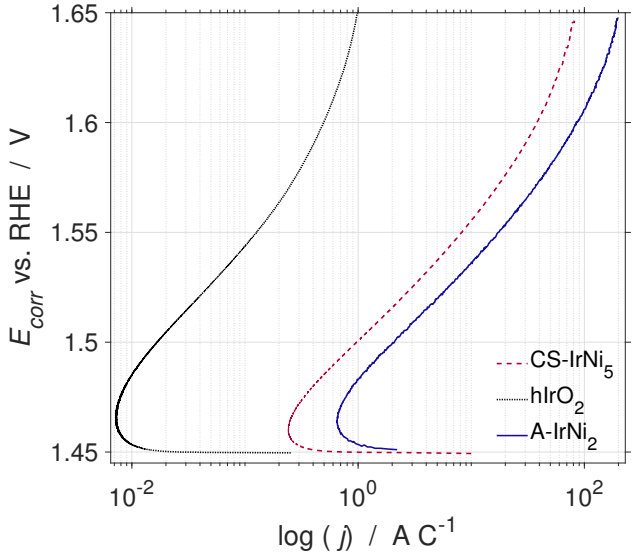

(b) Normalised with regards on charge

Figure 33: Combined, normalised polarisation curves for $hIrO_2$, $CS-IrNi_5$ and $A-IrNi_2$. A sweep rate of 3 mV min were used, and the potentials were corrected. A rotation of 1600 rpm was used.

normalised activity, and highest electrochemically active surface area. Highest values for the A−$IrNi_x$-samples were obtained by A−$IrNi_2$, even though A−$IrNi_5$ had a CS-structure. CS−$IrNi_x$-samples followed a trend with increasing overall activity along with reducing amount of Ir-precursor. This was not the case for the alloy-synthesis routine.

Tafel slope of the polarisation curves could be found by finding the slope of the polarisation curves, and values for all CS are presented in Table 5. In the table it can be seen that CS−$IrNi_x$-samples have values around $\sim$60 mV dec^{-1}. The slope decreased with reduced amount of Ir to Ni, for CS synthesised without oxygen present. Samples Ox−CS−$IrNi_2$ and CS−$IrNi_5$ have the lowest values of 51 mV dec^{-1} and 61 mV dec^{-1} respectively for the alloys and core-shell samples, but CS−$IrNi_5$ achieved a higher activity for OER than Ox−CS−$IrNi_2$

Fig. 41 shows a comparison between sample $hIrO_2$, A−$IrNi_5$ and CS−$IrNi_5$. Samples A−$IrNi_5$ and CS−$IrNi_5$ were chosen as they had highest mass activity of their respective category of syntheses. Measured Tafel slope for $hIrO_2$ was equal to 48 mV dec^{-1} (Table 5). TOP samples all had low activity for OER, and thus are not presented. In the figure it can be seen that all three samples had similar steepness of slope. Activity for OER can be ranged as: CS−$IrNi_5$ > A−$IrNi_2$ > $hIrO_2$, as CS−$IrNi_5$ achieved highest current at given voltage.

6 Discussion

From the TEM, SEM, EDX and XRD results, we could see an overall morphological and structural trend with reduction of Ir-precursor concentration compared to Ni. The uncontrolled growth of both the $IrNi_2$-samples, and the presence of dendrites indicated a kinetic process; otherwise the appearance would be close to the Wullf constructed hybrid shape, truncated octahedron.[10] Furthermore, the CS−$IrNi_2$-sample's hollow structure (Kirkendall effect) seen in the SEM-images (Fig. 21a), confirmed the high diffusion rates of deposits ($V_{depo}/V_{diff} >> 1$).[65] In line with the nucleation and growth theory, by reducing the Ir to Ni ratio we managed to narrow the size distribution and obtain more uniformly shaped particles.[10,28,48] Thus, producing truncated octahedron shaped particles for both CS−$IrNi_5$ and A−$IrNi_5$.

As a result of the controlled growth process by reducing the Ir:Ni ratio, we managed to achieve not only the thermodynamic predicted shape, but also core-shell structures for both synthesis methods. The reduced deposition rate of Ir ($V_{depo}/V_{diff} << 1$) promoted layer-by-layer growth, yielding shell formation of Ir. The CS-structures were confirmed by the EDX line and map-scans, and by performing CV in KOH for CS−$IrNi_x$-samples. Our results thus proved that by controlling the deposition rate of Ir-metal (shell), we are able to obtain core-shell structures for a on-pot colloidal bimetallic NP synthesis, for both co-reduced and successive reduced synthesis routines. Additionally, as expected, the subsequent segregation of A−$IrNi_x$-samples by electrochemically dealloying, were also able to form core-shell structures.

The reason why CS−$IrNi_5$ and A−$IrNi_2$ achieved highest catalytic activity for OER was possibly due to better overall coverage of Ir, thus a greater formation of the catalytic active porous IrO_2. By comparing the CVs of CS−$IrNi_5$ and A−$IrNi_2$ (Figs. 31 and 29) with the CV of AIROF in Fig. 27 we can discern a possible high anodic peak above 1.0 V, and no identical cathodic IrO_2-stripping peak at ∼0.96 V. This implies irreversible formation of porous IrO_2.[63] Tafel plot for both CS−$IrNi_5$ and A−$IrNi_2$ of respective 61 mV dec^{-1} and 69 mV dec^{-1}, might further confirm better coverage as these samples might undergo same reaction mechanism for OER, as other IrO_2-based catalysts. Furthermore, a cathodic peak at ∼0.23 V might indicate dissolution of Ni. This peak is visible for A−$IrNi_2$ and not for CS−$IrNi_5$. We can therefore from the CVs assume that these samples had different morphology and surface compositions.

By selecting one sample from each synthesis routine, mass activities could be therefore ranged as CS−$IrNi_5$>A−$IrNi_2$>$hIrO_2$. The successive core-shell-samples, collectively named CS−$IrNi_x$, increased in mass activity, CS−$IrNi_5$>CS−$IrNi_3$>CS−$IrNi_2$, with the reduction of the Ir-precursor compared to the Ni-precursor. Reducing the shell thickness gave a greater activity per mass Ir. This can be seen in Fig. 34. These trends were assumed

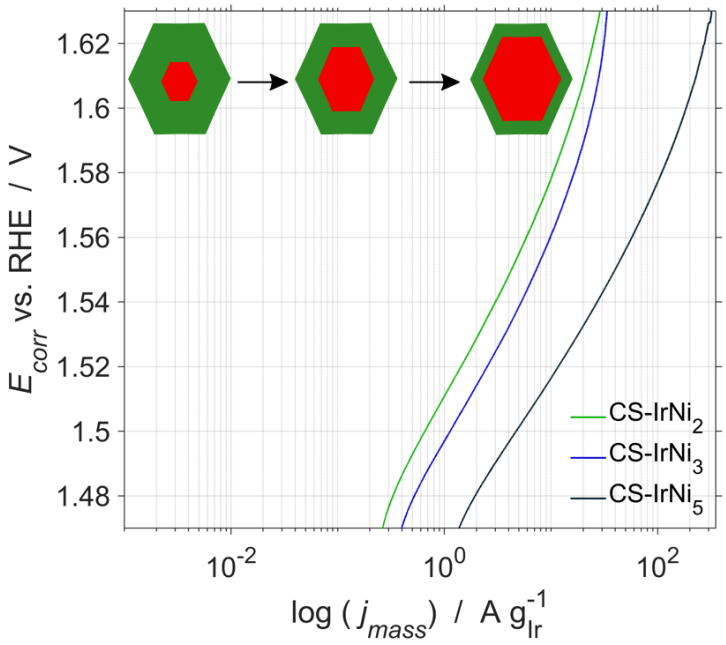

Figure 34: Mass activity for the core-shell CS−$IrNi_x$-catalysts. By reduction of shell thickness a corresponding trend with increase of activity occur. With the black line as CS−$IrNi_5$; that is the sample corresponding to the thinnest shell thickness.

to be followed by the A−$IrNi_x$-samples as well, especially because A−$IrNi_5$ also achieved a thermodynamic controlled core-shell structure, even before dealloying. In lieu of images of the dealloyed A−$IrNi_5$-sample, we can not visually tell any changes in surface morphology. However, as there were no significant changes in the CV during the dealloying process, there were most likely no great alterations of morphology either. Compared to A−$IrNi_5$, the size distribution of A−$IrNi_2$ was greater and broader. Along with the initially observed EDX-scans, A−$IrNi_2$ was more homogeneously mixed with a higher Ni content at surface. Thus, leading to the assumption that the A−$IrNi_2$-sample underwent leaching and surface roughening, forming porous and dendritic shaped particles.[5,20,66]

The higher activity may be a result of the surface roughening and different surface composition. As A−$IrNi_5$ and A−$IrNi_2$ gave visibly different CVs, and polarisation curves (specific and charge) did not overlap completely, the surface structure alone was not the only contribution to the different activities, but also the surface composition.[63] Furthermore, from the Tafel analysis ECSA was found, and it showed a greater value for A−$IrNi_5$, together with a higher charge activity of $1.10\,\mathrm{A\,C^{-1}}$. If A−$IrNi_2$ had a porous surface structure then this catalyst should in theory have achieved greater value for ECSA and charge activity, giving a larger surface area and more active sites. The low value for ESCA were most likely caused by either deactivation of active sites, i.e. blockage of pores, or different surface composition than A−$IrNi_5$.[27] Different surface morphology and composition can further be confirmed by the different values of Tafel slopes $69\,\mathrm{mV\,dec^{-1}}$ and $79\,\mathrm{mV\,dec^{-1}}$, for A−$IrNi_2$ and A−$IrNi_5$, respectively.[25] Without other characterisation methods available, such as XSP, we can not tell exact compositional differences.

Nevertheless, mass activity for the A−$IrNi_x$-samples deviated from the trend CS−$IrNi_x$-samples obtained. with the reduction of the molar ratio of Ir to Ni, the mass activity for CS-samples was increased because of a thinner shell. The inconsistent results for the A−$IrNi_x$-samples lead us to the assumption that synthesising bimetallic core-shell structures by co-reduction and subsequent dealloying, is difficult to control, for both morphological (e.g. size dependent) and compositional changes. Furthermore, by comparing our results with Nong *et al.*'s[5] we could see that their results for dealloyed samples deviated from the expected trend as well, where the sample with the second highest ratio of Ir to Ni (out of three samples) achieved the highest mass activity. Thus leaving even more inconsistent results compared to the expected, and already observed trend for CS−$IrNi_x$-samples. It is evident from our and the reported results in the literature, that for this type of synthesis it is especially difficult to control the outcome of the product. Successive reduction is therefore an easier way to synthesise bimetallic core-shell structures.

In terms of activity, the successive synthesised CS−$IrNi_5$ sample achieved highest catalytic activity for OER, for both mass and charge. At an overpotential measured at $\eta = 295\,\mathrm{mV}$ (1.525 V), CS−$IrNi_5$ achieved a mass and charge activity of $14.23\,\mathrm{A\,g_{Ir}^{-1}}$ and $2.2\,\mathrm{A\,C^{-1}}$, respectively. By comparing these results with previous benchmarked rutile-structured IrO_2 reported by Abbot *et al.*[27], our sample has one third of the mass activity and value of ESCA. Moreover, at $\eta = 250\,\mathrm{mV}$ our sample achieved a mass activity of $1.98\,\mathrm{A\,g_{Ir}^{-1}}$, which is on par with Marshall *et al.*'s[67] rutile structured IrO_2, of $\sim 2\,\mathrm{A\,g_{Ir}^{-1}}$. However, for the previous mentioned dealloyed IrNi-sample

reported by Nong *et al.*[5], our sample achieved 60 times less activity, at η =250 mV. Thus leaving our CS−$IrNi_5$ catalyst at the lower region in terms of the reported samples' catalytic efficiency.

Reducing the size alone for $IrNi_x$-samples will have a great effect on the OER activity. Regardless of the lower mass activity for our CS−$IrNi_5$-sample compared to the benchmarked IrO_2 and IrNi@IrO_2 catalysts mentioned above, our catalyst obtained on par results with Marshall *et al.*'s[67] rutile structured IrO_2, with 10 times the particle size. Where CS−$IrNi_5$ had a particle size distribution between 10-20 nm, and all reported above had particles ranged between 1.7-5 nm.[5,27,67] As is known from the theory, particle size and surface area do not alone decide the catalytic activity, but they are known to have a great effect.[5,10,27] For ffc phased metallic NPs such as $IrNi_x$, reducing the the size further will induce growth of the {111} facet (see Wulff plot, Section 2.4.2)) that has lower surface energy than the mix of {100} and {111}. Reducing the particle size would have given a lower binding energy, and given a further increase of OER activity for our samples.[6]

From the XRD and EDX-results we can assume that phosphorous were incorporated into the structure by adding TOP. This was confirmed by the no longer magnetic $IrNi_x$-samples and the increase in stabilisation, which resulted in no more formation of agglomerates and particles size down to 2 nm. Characterising the TOP-samples was difficult due to drifting and charging effect, resulting in poor EDX images where particles were damaged or erased by the electron beam, thus giving high uncertainties in particle composition. Nevertheless, the electrochemical measurements implied presence of Ir at surface as we had a IrO_2 response in both the CV and LSV-measurements. The cyclic voltammograms and the polarisation curves gave similar responses as previous $IrNi_x$-samples, but with much lower current density and mass and charge activity. All Tafel slopes for TOP-products were above 80 mV dec^{-1} implying different surface compositions than the samples synthesised without TOP. Although we were able to achieve growth of Ir in the presence of TOP, it seems like as expected, the capping agent inhibited the growth. From the Tafel calculations, the TOP-samples showed a weak trend with the activities of: $T_{0.2}$−$IrNi_2$>$T_{0.1}$−$IrNi_2$>$T_{0.05}$−$IrNi_2$, but without any other characterisation methods such as XPS, we can not say any further what caused this result.

Due to poor stabilisation of the particles synthesised without TOP, possible bi-products of hcp phased Ni were formed in the CS-syntheses. The XRD spectra for CS−$IrNi_x$-samples (see Fig. 13) show possible formation

metastable garutiite phase of Ni (hcp-crystal structure). Taking the TEM and EDX-mapping into account: with the increased Ni:Ir ratio, there was formation of big particles with no coverage of Ir. This phase could also be detected through BF-HRTEM-image of CS−$IrNi_5$, showing (both fcc and) hcp structured Ni. Due to the poor coverage of Ir and further lattice mismatch between Ir and Ni, we can therefore assume that this may have had an impact on the OER activity. This proves that both $IrNi_x$-routines might need better stabilisation of the nanoparticles.

7 Conclusion

In this master's thesis we managed to successfully synthesise core-shell structures of IrNi@IrO_x nanoparticles by two different one-pot synthesis routines, with only oleylamine present as reducing and stabilising agent. The first method consisted of adding the precursors in two steps (successive reduction), by first reducing the core material of Ni with the following growth of an Ir-shell. Subsequently, nanoparticles were electrochemically oxidised. The second synthesis was performed through a one-step co-reduction of the precursors, followed by electrochemically dealloying in a CO-atmosphere, and thereafter oxidising. By controlling the growth of the particles by reducing the ratio of Ir-precursor to Ni-precursor, we were furthermore able to obtain core-shell structures with the second synthesis routine even before dealloying. Hence, we also managed to synthesise bimetallic core-shell structures through a one-pot, one-step synthesis.

The successive core-shell synthesis gave an activity that can be fully rationalised by the composition of the catalyst; the thicker the shell the less efficient the catalyst per mass of iridium for a given surface area and shell composition. Therefore the activity of the CS$-IrNi_5$ was higher per mass iridium than the CS$-IrNi_2$, with an intermediate activity for the CS$-IrNi_3$. No clear trend was apparent in the samples synthesised by dealloying, where sample A$-IrNi_2$, i.e. the sample with highest iridium content, obtained the highest mass activity compared to A$-IrNi_5$, even with lower value of ECSA. Resulting in the conclusion that the dealloying process yields poor surface growth control, with (deactivated) porous and roughened surface.

EDX and electrochemical measurements may indicate that the composition of the surface of the A$-IrNi_2$ was different than A$-IrNi_3$ and A$-IrNi_5$. In which the difference in surface composition may explain the high mass activity of A$-IrNi_2$ compared to the other dealloyed samples, and why the A$-IrNi_x$ did not follow the trend that CS$-IrNi_x$ did. This supports the conclusion that the successive core-shell synthesis represented a more reproducible method for manufacturing segregated iridium-metal structures.

These catalysts displayed an OER mass activity corresponding to typically $14.23\,\mathrm{A\,g_{Ir}^{-1}}$ measured at an overpotential of 289 mV or $1.98\,\mathrm{A\,g_{Ir}^{-1}}$ at 250 mV, for CS$-IrNi_5$. Resulting catalysts were thermodynamically less efficient per noble metal mass content compared to novel IrNi-based nanocatalysts reported in the literature, but on par with earlier bench-marked IrO_2-catalysts.

With that in mind, the presented CS−$IrNi_5$ catalyst had up to 10 times the particle sizes of reported catalysts. If the particle size was reduced the core-shell catalyst may be able to compete with the best reported results in the literature.

TOP was added in different low ratios of TOP to OAm, to observe the effect on the iridium growth, and simultaneously reduce the particle size. The EDX scans showed little to no iridium amount present, however there was some electrochemical response for iridium, where the sample with highest TOP content $y_{TOP} = 0.2$ achieved highest mass activity for OER. Without any further characterisation method such as XPS we can not tell the reason of this trend, due to poor images and XRD patterns. From the results we can ascertain that some growth of iridium occurred, but the presence of TOP was most likely blocking and inhibiting further growth. A different capping agent with weaker affinity for a nickel surface is recommended in future work.

7.1 Future Work

We propose that in-situ, same-site S(T)EM and EDX measurements of the dealloying process should be conducted in the future. By applying the catalysts on a marked TEM-grid, with a thicker stabilising film to withstand the acidic environment, that would function as the working electrode. Thus, one would be able to observe the structural changes during dealloying (and oxidising) process, and perhaps be able to obtain better knowledge in order to help control the process. By obtaining in-situ knowledge of this process one may be able to construct core-shell nanoparticles with controlled rougher and porous surfaces. As the results presented in this thesis and by others suggest for this type of system, one may then be able to achieve an even higher catalytic mass activity for OER. This procedure may also explain why there is no trend with varying molar ratio between the metal precursors for A−$IrNi_x$, as was the case for the successive core-shell synthesis, CS−$IrNi_x$. Surface study, such as XPS should also be included for both syntheses to give an overall better understanding on the surface processes.

One main focus for future work should be on reducing the particle size for both of the syntheses, to increase the mass specific activity. Therefore, to obtain better knowledge on our system, we should proceed the work by doing a parameter study. First without adding other additives into the system, because it is then easier to get an overview of the three component system

rather than a system with more components present. Additionally, adding a capping agent other than TOP might inhibit shell-growth, even for capping agents that are less strongly bonded to nickel surface. We were already able to successfully produce thermodynamic products with narrower size and morphological distribution of core-shell structures, by only changing the precursors ratio. Tuning the particle's size and shapes further can be done by controlling the injection rate of precursors.[10] This might be useful for controlling nickel growth in the first step of the successive synthesis causing an overall size reduction.[10] Changing reaction time might also be a possibility and/or a carefully study on temperature effect.

The produced nanoparticles were prone to agglomeration most likely due to magnetism (poor stabilisation), we would therefore recommend making the inks with stabilisers present to keep the overall surface area stable. This might give a better dispersion and more reproducible electrochemical results. The particles were not easily dispersed and redispersed, and it worsened with increased nickel concentration. Making inks with CS$-IrNi_5$ would therefore be a fast and easy way to see if the stabiliser has any effect on the catalytic activity.

Finally, scaling up the syntheses should be investigated in the future. If a catalyst is to be used for commercial use in the long future; we must know if the synthesis is reproducible after up-scaling.

References

(1) Mazloomi, K.; Gomes, C. *Renewable and Sustainable Energy Reviews* **2012**, *16*, 3024–3033.

(2) M.Letcher, T., *Future Energy, Improved, Sustainable and Clean Options for our Planet*; Elsvier Ltd.: 2014; Chapter 23.

(3) Carmo, M.; Fritz, D. L.; Mergel, J.; Stolten, D. *International journal of hydrogen energy* **2013**, *38*, 4901–4934.

(4) González, A. M.; Lora, E. E. S.; Palacio, J. C. E.; del Olmo, O. A. A. *International Journal of Hydrogen Energy* **2018**, *43*, 7808–7822.

(5) Nong, H. N.; Gan, L.; Willinger, E.; Teschner, D.; Strasser, P. *Chemical Science* **2014**, *5*, 2955–2963.

(6) Rossmeisl, J.; Qu, Z.-W.; Zhu, H.; Kroes, G.-J.; Nørskov, J. K. *Journal of Electroanalytical Chemistry* **2007**, *607*, 83–89.

(7) Trasatti, S. *Croatica Chemica Acta* **1990**, *63*, 313–329.

(8) Cherevko, S.; Geiger, S.; Kasian, O.; Kulyk, N.; Grote, J.-P.; Savan, A.; Shrestha, B. R.; Merzlikin, S.; Breitbach, B.; Ludwig, A., et al. *Catalysis Today* **2016**, *262*, 170–180.

(9) Sneed, B. T.; Young, A. P.; Tsung, C.-K. *Nanoscale* **2015**, *7*, 12248–12265.

(10) Xia, Y.; Xia, X.; Peng, H.-C. *Journal of the American Chemical Society* **2015**, *137*, 7947–7966.

(11) Ishizaki, T.; Yatsugi, K.; Akedo, K. *Nanomaterials* **2016**, *6*, 172.

(12) Allen J. Bard, L. R. F., *Electrochemical Methods, Fundamentals and Applications*; John Wiley & Sons, Inc: 2001.

(13) Keith B. Oldham, J. C. M.; Bond, A. M., *Electrochemical Science and Technology, Fundamentals and Application*; Wiley: 2012.

(14) Teles, J. J.; Faria, E. R.; Franco, D. V.; Da Silva, L. M. *International Journal of Electrochemical Science (Online)* **2017**, *12*, 1755–1773.

(15) Shinagawa, T.; Garcia-Esparza, A. T.; Takanabe, K. *Scientific reports* **2015**, *5*, 13801.

(16) Soderberg, J. N.; Co, A. C.; Sirk, A. H.; Birss, V. I. *The Journal of Physical Chemistry B* **2006**, *110*, 10401–10410.

(17) S. Ardizzone, G. F.; S.Trasatti *Electrochemical Acta* **1990**, *35*, 236–267.

(18) Łukaszewski, M.; Soszko, M.; Czerwiński, A. *Int. J. Electrochem. Sci* **2016**, *11*, 4442–4469.

(19) Chan, H. T.; Kätelhön, E.; Compton, R. G. *Journal of Electroanalytical Chemistry* **2017**, *799*, 126–133.

(20) Erlebacher, J.; Aziz, M. J.; Karma, A.; Dimitrov, N.; Sieradzki, K. *Nature* **2001**, *410*, 450.

(21) Choi, Y.; Kuttiyiel, K. A.; Labis, J. P.; Sasaki, K.; Park, G.-G.; Yang, T.-H.; Adzic, R. R. *Topics in Catalysis* **2013**, *56*, 1059–1064.

(22) Oezaslan, M.; Heggen, M.; Strasser, P. *Journal of the American Chemical Society* **2011**, *134*, 514–524.

(23) Kumar, S. S.; Himabindu, V. *Materials Science for Energy Technologies* **2019**.

(24) Giordano, L.; Han, B.; Risch, M.; Hong, W. T.; Rao, R. R.; Stoerzinger, K. A.; Shao-Horn, Y. *Catalysis Today* **2016**, *262*, 2–10.

(25) Reksten, A. H.; Thuv, H.; Seland, F.; Sunde, S. *Journal of Electroanalytical Chemistry* **2018**, *819*, 547–561.

(26) De Pauli, C.; Trasatti, S. *Journal of Electroanalytical Chemistry* **2002**, *538*, 145–151.

(27) Abbott, D. F.; Lebedev, D.; Waltar, K.; Povia, M.; Nachtegaal, M.; Fabbri, E.; Copéret, C.; Schmidt, T. J. *Chemistry of Materials* **2016**, *28*, 6591–6604.

(28) Cao, G.; Wang, Y., *Nanostructures and Nanomaterials 2nd Edition, Synthesis, Properties, and Applications*; World Science: 2014.

(29) Sau, T. K.; Rogach, A. L. *Advanced Materials* **2010**, *22*, 1781–1804.

(30) Polte, J. *CrystEngComm* **2015**, *17*, 6809–6830.

(31) Thanh, N. T.; Maclean, N.; Mahiddine, S. *Chemical reviews* **2014**, *114*, 7610–7630.

(32) Jiang, Y.; Xu, C.-h.; Lan, G.-q. *Transactions of Nonferrous Metals Society of China* **2013**, *23*, 180–192.

(33) Subhramannia, M.; Pillai, V. K. *Journal of Materials Chemistry* **2008**, *18*, 5858–5870.

(34) Stamenkovic, V. R.; Fowler, B.; Mun, B. S.; Wang, G.; Ross, P. N.; Lucas, C. A.; Marković, N. M. *science* **2007**, *315*, 493–497.

(35) Mourdikoudis, S.; Liz-Marzan, L. M. *Chemistry of Materials* **2013**, *25*, 1465–1476.

(36) Sasaki, K.; Kuttiyiel, K. A.; Barrio, L.; Su, D.; Frenkel, A. I.; Marinkovic, N.; Mahajan, D.; Adzic, R. R. *The Journal of Physical Chemistry C* **2011**, *115*, 9894–9902.

(37) Yu, W.; Porosoff, M. D.; Chen, J. G. *Chemical reviews* **2012**, *112*, 5780–5817.

(38) Kuttiyiel, K. A.; Choi, Y.; Sasaki, K.; Su, D.; Hwang, S.-M.; Yim, S.-D.; Yang, T.-H.; Park, G.-G.; Adzic, R. R. *Nano Energy* **2016**, *29*, 261–267.

(39) Toshima, N.; Yonezawa, T. *New Journal of Chemistry* **1998**, *22*, 1179–1201.

(40) Tsuji, M.; Yamaguchi, D.; Matsunaga, M.; Ikedo, K. *Crystal Growth & Design* **2011**, *11*, 1995–2005.

(41) Lorenz, W.; Staikov, G. *Surface science* **1995**, *335*, 32–43.

(42) Zafeiratos, S.; Piccinin, S.; Teschner, D. *Catalysis Science & Technology* **2012**, *2*, 1787–1801.

(43) Ruban, A.; Skriver, H. L.; Nørskov, J. K. *Physical review B* **1999**, *59*, 15990.

(44) Mehtap Oezaslan, F. H.; Strasser, P. *The Journal of Physical Chemistry* **2013**, *5*, 3273–3291.

(45) Chee, S. W.; Wong, Z. M.; Baraissov, Z.; Tan, S. F.; Tan, T. L.; Mirsaidov, U. *Nature Communications* **2019**, *10*, 2831.

(46) Yin, Y.; Rioux, R. M.; Erdonmez, C. K.; Hughes, S.; Somorjai, G. A.; Alivisatos, A. P. *Science* **2004**, *304*, 711–714.

(47) Yu, Y.; Yang, W.; Sun, X.; Zhu, W.; Li, X.-Z.; Sellmyer, D. J.; Sun, S. *Nano letters* **2014**, *14*, 2778–2782.

(48) Donegan, K. P.; Godsell, J. F.; Otway, D. J.; Morris, M. A.; Roy, S.; Holmes, J. D. *Journal of Nanoparticle Research* **2012**, *14*, 670.

(49) Carenco, S. *The Chemical Record* **2018**, *18*, 1114–1124.

(50) Perego, G. *Catalysis Today* **1998**, *41*, 251–259.

(51) Aylward, G. H.; J.Findlay, T., *SI Chemical Data 6th etd.* John Wiley and Sons Ltd: 2008; Chapter 23.

(52) William D. Callister JR., D. G. R., *Material Science and Engineering 9th Edition*; Wiley: 2015.

(53) A.K.Chatterjee, *Handbook of Analytical Techniques in Concrete Science and Technology, Principles, Techniques, and Applications*; William Andrew: 2001.

(54) M.F.Toney, B., *Metallic Films for Electronic, Optical and Magnetic Applications, Structure, Processing and Properties*; Woodhead Publishing: 2014.

(55) Egerton, R. F., *Physical Principles of Electron Microscopy, An Introduction to TEM, SEM and AEM*; Springer: 2007.

(56) Cazaux, J. *Journal of Electron Microscopy* **2012**, *61*, 261–284.

(57) Shino, D.; Oikawa, T., *Analytical Electron Microscopy for Materials Science*; Springer: 1998.

(58) Lervik, I. A.; Tsypkin, M.; Owe, L.-E.; Sunde, S. *Journal of Electroanalytical Chemistry* **2010**, *645*, 135–142.

(59) McDonald, A. M.; Proenza, J. A.; Zaccarini, F.; Rudashevsky, N. S.; Cabri, L. J.; Stanley, C. J.; Rudashevsky, V. N.; Melgarejo, J. C.; Lewis, J. F.; Longo, F., et al. *European Journal of Mineralogy* **2010**, *22*, 293–304.

(60) V. Birss R. Myers, H. A.-K.; Conway, B. E. *Electrochemical Science and Technology* **1984**, *131*, 1502–1510.

(61) Gottesfeld, S.; McIntyre, J.; Beni, G.; Shay, J. *Applied Physics Letters* **1978**, *33*, 208–210.

(62) Saveleva, V. A.; Wang, L.; Teschner, D.; Jones, T.; Gago, A. S.; Friedrich, K. A.; Zafeiratos, S.; Schlögl, R.; Savinova, E. R. *The journal of physical chemistry letters* **2018**, *9*, 3154–3160.

(63) Touni, A.; Papaderakis, A.; Karfaridis, D.; Vourlias, G.; Sotiropoulos, S. *Molecules* **2019**, *24*, 2095.

(64) Alsabet, M.; Grden, M.; Jerkiewicz, G. *Electrocatalysis* **2014**, *5*, 136–147.

(65) Yin, Y.; Erdonmez, C.; Aloni, S.; Alivisatos, A. P. *Journal of the American Chemical Society* **2006**, *128*, 12671–12673.

(66) Gan, L.; Heggen, M.; Rudi, S.; Strasser, P. *Nano letters* **2012**, *12*, 5423–5430.

(67) Marshall, A.; Børresen, B.; Hagen, G.; Tsypkin, M.; Tunold, R. *Energy* **2007**, *32*, 431–436.

A List of Symbols

Table 6: List of latin symbols used, with their respective meanings. Arranged in alphabetical order.

Symbols	Unit	Meaning
a_{i}	$\mathrm{mol\,m^{-3}}$	Activity of species i
a^*	$\mathrm{mol\,m^{-3}}$	Critical activity
A	$\mathrm{m^2}$	Particle surface area
b	$\mathrm{V\,dec^{-1}}$	Tafel slope
c	$\mathrm{mol\,m^{-3}}$	Concentration
d_{hkl}	m	Spacing between atomic planes
D	m	Mean size of crystalline domains
E_{ap}	V	Anodic peak voltage
E_{cp}	V	Cathodic peak voltage
E_{cell}	V	Potential of cell system
E_{RE}	V	Potential of reference electrode
E_{rev}	V	Reversible potential
E_{WE}	V	Potential of working electrode
E^0	V	Standard electrochemical potential
F	$\mathrm{C\,mol^{-1}}$	Faraday constant
ΔG	$\mathrm{J\,mol^{-1}}$	Change in Gibbs free energy
ΔG^0	$\mathrm{J\,mol^{-1}}$	Change in standard Gibbs free energy
ΔG_{V}	$\mathrm{J\,mol^{-1}}$	Change in volume Gibbs free energy
ΔG_{s}	$\mathrm{J\,mol^{-1}}$	Change in surface Gibbs free energy
ΔG_{hom}	$\mathrm{J\,mol^{-1}}$	Homogeneous nucleation energy barrier
ΔG_{het}	$\mathrm{J\,mol^{-1}}$	Heterogeneous nucleation energy barrier
ΔH^0	$\mathrm{J\,mol^{-1}}$	Change in standard enthalpy
j	$\mathrm{A\,m^{-2}}$	Current density
j_0	$\mathrm{A\,m^{-2}}$	Exchange current
j_a,j_c	$\mathrm{A\,m^{-2}}$	Anodic (a) and cathodic (c) current density
k_{B}	$\mathrm{J\,K^{-1}}$	Boltzmann constant
k_i	Varies	Rate constant for step i
K	-	Scherrer constant

List of latin symbols used, with their respective meanings. Arranged in alphabetical order.

Symbols	**Unit**	**Meaning**
n	mol	Number of moles
q_T^*	C	Total surface charge
q_i^*	C	Inner surface charge
q_s^*	C	Outer surface charge
r	m	Particle radius
r^*	m	Critical particle radius
R	$\mathrm{J\,K^{-1}mol^{-1}}$	Gas constant
R_{cell}	Ω	Resistance of ionic conductor
R_{circuit}	Ω	Resistance of electronic conductor
S	-	Degree of supersaturation
ΔS^0	$\mathrm{J\,mol^{-1}}$	Change in standard entropy
T	K	Temperature
t	s	Time
V	$\mathrm{m^3}$	Volume
V_{m}	$\mathrm{m^3\,mol^{-1}}$	Molar volume
V_{depo}	$\mathrm{m^3}$	Volume of atoms deposited on a surface
V_{diff}	$\mathrm{m^3}$	Volume of atoms diffusing to a surface

Table 7: List of greek symbols used, with its respective meanings. Arranged in alphabetical order.

Symbols	**Unit**	**Meaning**
α	-	Transfer coefficient
β	-	Peak broadening at half maximum intensity
γ	$\mathrm{J\,m^{-2}}$	Surface tension
γ	-	Activity coefficient
η	V	Overpotential
Θ	-	Incident beam angle
Θ_B	-	Diffraction angle
λ	m	Wavelength
η	V	Overpotential
$\eta_\mathrm{act,a}$, $\eta_\mathrm{act,c}$	V	Activation overpot. of anode (a) and cathode (c)
η_conc	V	Concentration overpotential
μ_V	$\mathrm{J\,mol^{-1}}$	Change in volume chemical potential
ν	$\mathrm{V\,s^{-1}}$	Sweep rate
ϕ	-	Wetting factor

B List of Abbreviations

Table 8: List of abbrevations used, with its respective meanings. Arranged in alphabetical order.

Abbrevation	**Meaning**
Ar	Argon
AIROF	Anodically formed iridium oxide film
BF-TEM	Bright field transmission electron microscopy
BSE	Backscattered electrons
BU	Bottum-up approach
CE	Counter electrode
CNT	Classical nucleation theroy
CS	Core-Shell
CS-NP	Core-Shell nanoparticle
CV	Cyclic voltammetry
DF-TEM	Dark field transmission electron microscopy
DI	Deionised
ECSA	Electrochemically active surface area
EDX	Energy-dispersive X-ray spectroscpy
EM	Electron microscopy
EtOH	Ethanol
fcc	Face-centred cubic
GC	Glassy carbon
hcp	Hexagonal close packed
HER	Hydrogen evolution reaction
HHV	Higher heating value
HR-TEM	High resolution transmission electron microscopy
IPA	Isopropanol
LSV	Linear Sweep Voltammetry
MNP(s)	Metal nanoparticle(s)
MONP(s)	Metal oxide nanoparticle(s)

List of abbrevations used, with its respective meanings. Arranged in alphabetical order.

Abbrevation	**Meaning**
NM(s)	Nanomaterial(s)
NP(s)	Nanoparticle(s)
OAm	Oleylamine
OER	Oxygen evolution reaction
ORR	Oxygen reduction reaction
PEM	Proton exchange membrane
PEMFC	Proton exchange membrane fuel cell
PVA	Polyvinyl alcohol
PVP	Polyvinylpyrrolidone
rds	Rate determining step
RHE	Reversible hydrogen electrode
RE	Reference electrode
rpm	Rotations per minutes
SA	Surface area
SE	Secondary electron
SEM	Scanning electron microscopy
SS	Supersaturation
S(T)EM	Scanning transmission electron microscopy
TD	Top-down approach
TEM	Transmission electron microscopy
TOP	Tri-n-octylphosphine
WE	Working electrode
XPS	X-ray photoelectron spectroscopy
XRD	X-ray diffraction

Polishing of Iridium bulk electrode

The electrode was first polished with a dispersion of 0.5 µm monocrystalline diamond paste applied on a MD-Nap-T pad, and thereafter with 5 µm, 0.3 µm and 0.05 µm Alumina dispersions. A nylon pad was used for the 5 µm dispersion, while microcloth were used for the 0.3 µm and 0.05 µm dispersions. The electrode was washed with deionized water (DI water)(Millipore Direct-Q3 18.2 MΩ cm).

C Supplementing Results

C.1 Additional Results: TEM, SEM and EDX

Ox−A−$IrNi_2$

Fig. 35 shows a BF-TEM image and size distribution histogram of a cluster of particles for sample Ox−A−$IrNi_2$.

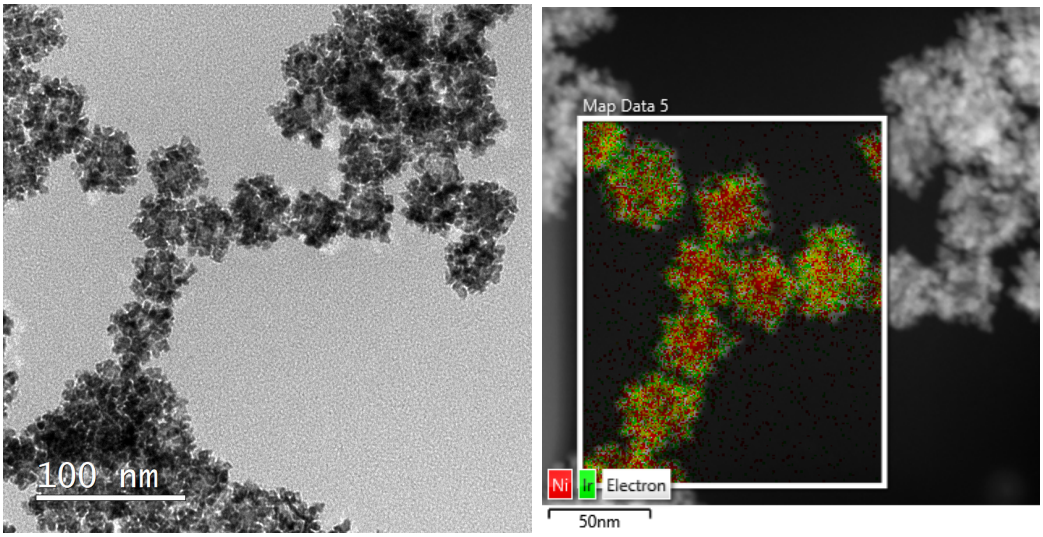

(a) **(b)**

Figure 35: a) BF-TEM image showing dendrite formation of sample Ox−A−$IrNi_2$, and b) SEM-EDX map scan of the same site as in a). Map scan is denoted with Ni in red as core and Ir in green.

A−$IrNi_3$

Fig. 36 shows a BF-TEM image and size distribution histogram of a cluster of particles for sample A−$IrNi_3$.

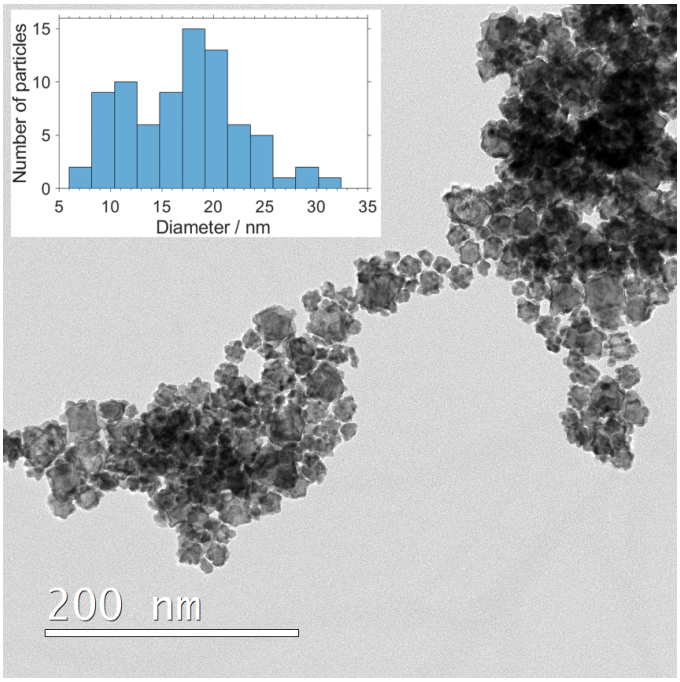

Figure 36: BF-TEM for sample A−$IrNi_3$ showing clusters of alloy NPs. Includes histogram for given site of sample.

C.1.1 $IrNi_x$ Core-Shell Nanoparticles

CS−$IrNi_2$

Fig. 37 shows a BF-TEM image and size distribution histogram of a cluster of particles.

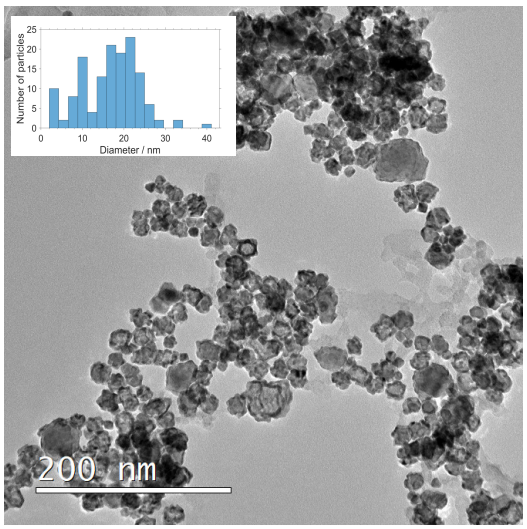

Figure 37: BF-TEM image of sample CS−$IrNi_2$ showing cluster with particles. Including histogram over given site.

CS−$IrNi_5$

Fig. 38 shows closed up area of a Ni particle that has a hcp-phased crystal structure.

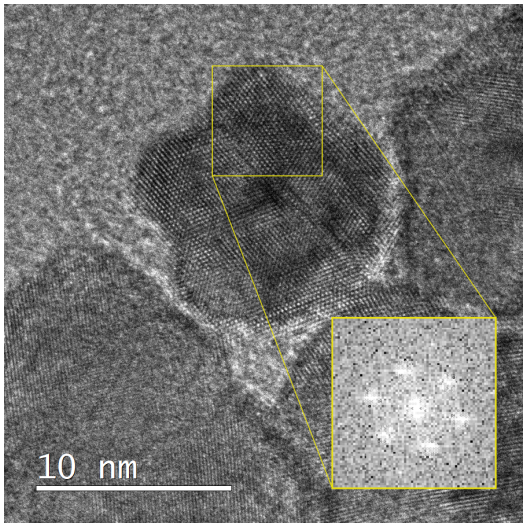

Figure 38: BF-HRTEM image of CS−$IrNi_5$ sample. Showing hcp phased Ni.

$\mathbf{T_{0.2}}$–$\mathbf{IrNi_2}$

In Fig. 39 BF-TEM image of $T_{0.2}$–$IrNi_2$-sample can be seen.

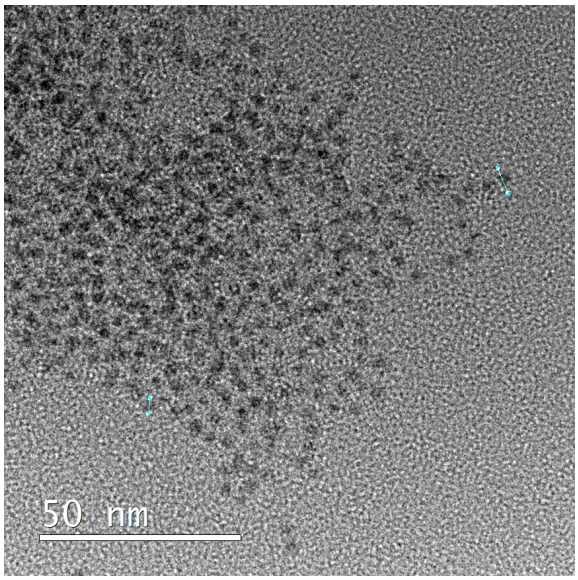

Figure 39: DF-TEM image of $T_{0.2}$–$IrNi_2$-sample

$\mathbf{T_{0.05}}$–$\mathbf{IrNi_2}$

In Fig. 40 BF-TEM image of $T_{0.05}$–$IrNi_2$-sample can be seen.

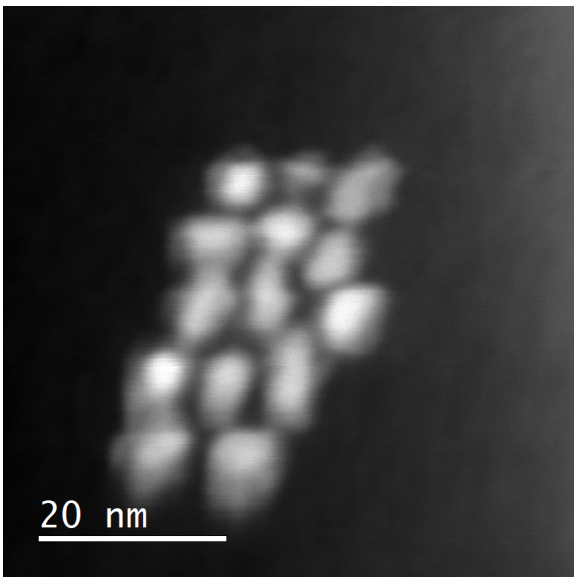

Figure 40: DF-TEM image of $T_{0.05}-IrNi_2$-sample

C.1.2 CV and LSV

Fig. 41 shows a comparison of polarisation curves for sample $hIrO_2$, $CS-IrNi_5$ and $A-IrNi_5$.

Electrochemical measurements for all T_y-IrNi_2-samples are presented in this Appendix. Fig. 42 shows the combined CV-measurements and the following image Fig. 43, shows the combined LSV-measurements.

Table. 9 shows the calculated mass and charge activities. Including ESCA, at a measured overpotential of 1.525 V.

Table 9: Tafel slopes, mass and charge activities, and ECSA for TOP-samples. Measured at 1.525 V

Sample	**b** $mVdec^{-1}$	**Mass Activity** Ag_{Ir}^{-1}	**Charge Activity** AC^{-1}	**ECSA** $m^2g_{Ir}^{-1}$
$A-IrNi_5$	79	5.71	1.10	43
$T_{0.05}-IrNi_2$	381	0.29	0.12	20
$T_{0.1}-IrNi_2$	381	0.54	0.05	138
$T_{0.2}-IrNi_2$	88	1.19	0.16	32

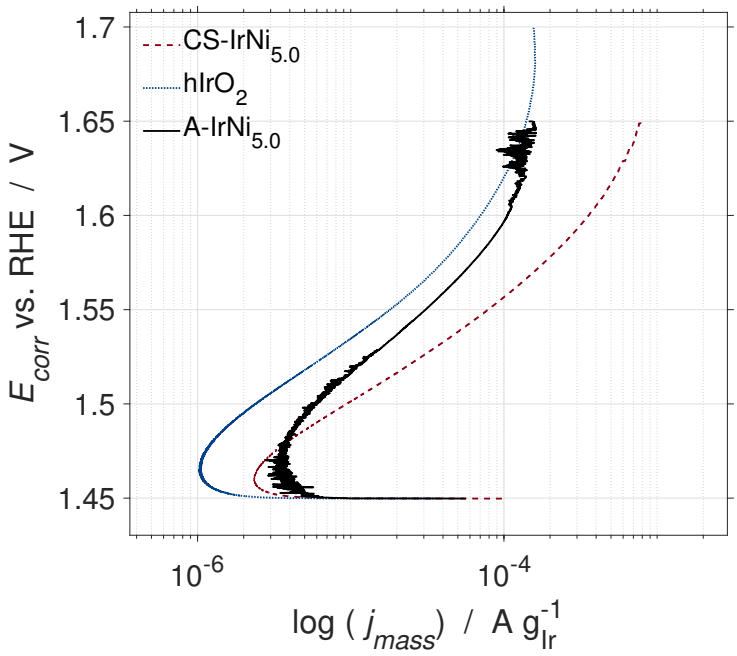

Figure 41: Comparison of polarisation curves for sample: $hIrO_2$, $A-IrNi_5$ and $CS-IrNi_5$. Noted with blue dotted line, black line and red dashed line, respectively. The curves were normalised with regards on mass of Ir, and the voltage was jR-compensated at 85 % and corrected. A rotation of 1600 rpm was used for all samples.

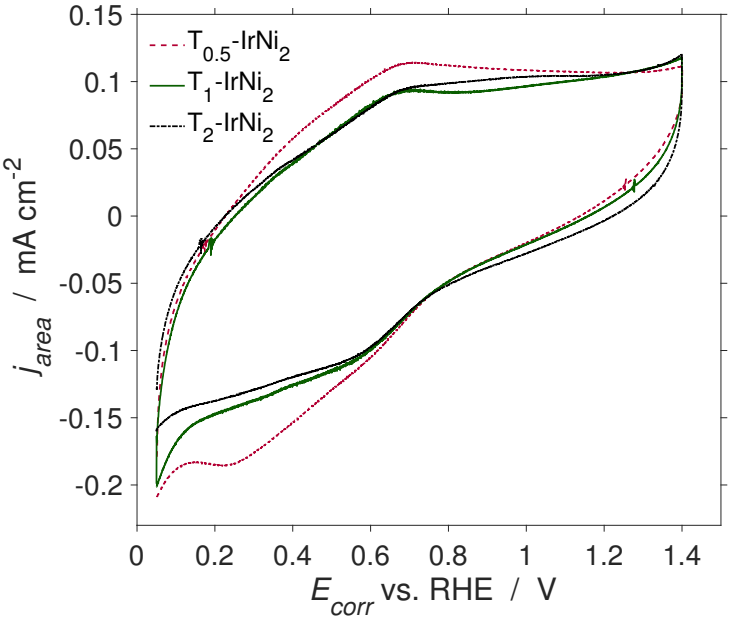

Figure 42: jR-corrected CVs of all TOP-samp les combined, after oxidation of catalysts. Red dashed line is equal to $T_{0.05}$−$IrNi_2$, green solid as $T_{0.1}$−$IrNi_2$ and black dotted as $T_{0.2}$−IrNi. The CVs were measured at 150 m V s^{-1} and 1600 rpm, with a catalyst loading of ∼25 µg cm^{-2}; In 0.5 mol dm^{-3} H_2SO_4 and under N_2 saturated atmosphere.

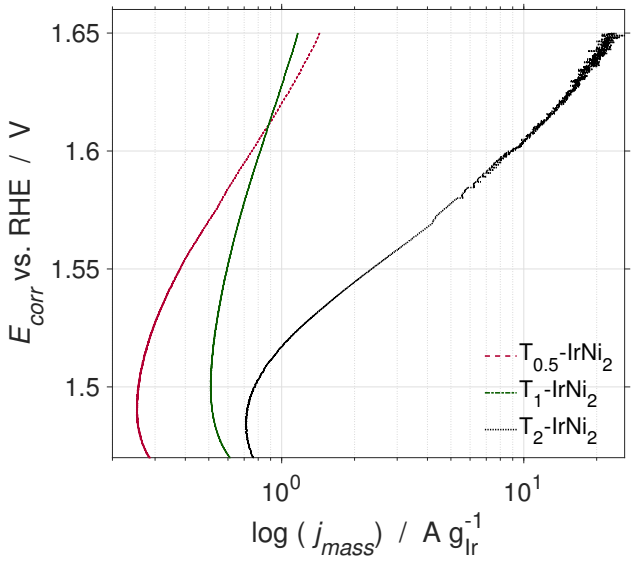

(a) Normalised with regards on mass of Ir.

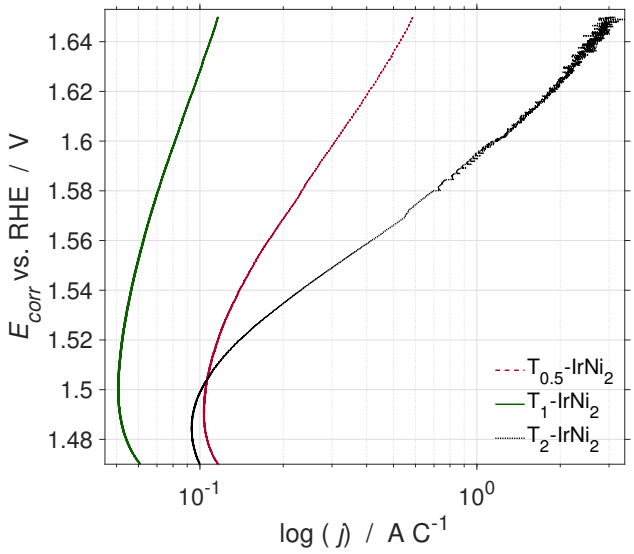

(b) Normalised with regards on charge.

Figure 43: Polarisation curves for samples synthesised with TOP. LSV were recordet with a rotation rate of 1600rpm. Red dashed line denotes sample $T_{0.05}-IrNi_2$, green dotted line as $T_{0.1}-IrNi_2$, and black solid line as $T_{0.2}-IrNi_2$

C.1.3 Results XRD

XRD patterns for sample Ox−A−$IrNi_2$ and A−$IrNi_5$, showing the formation of the peak at 76.93° for A−$IrNi_5$ as well.

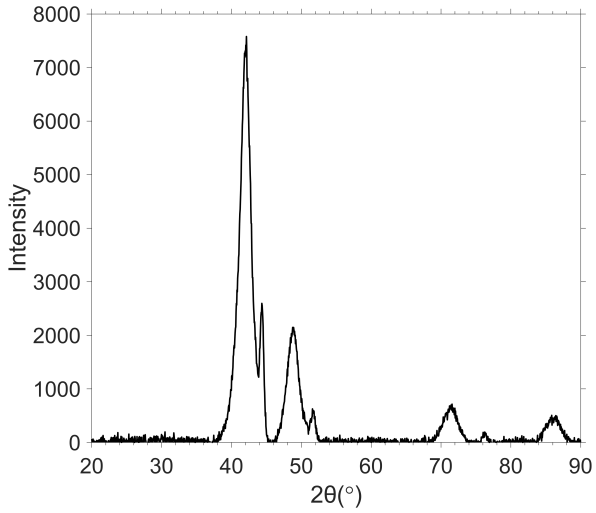

(a) XRD pattern for sample Ox−A−$IrNi_2$

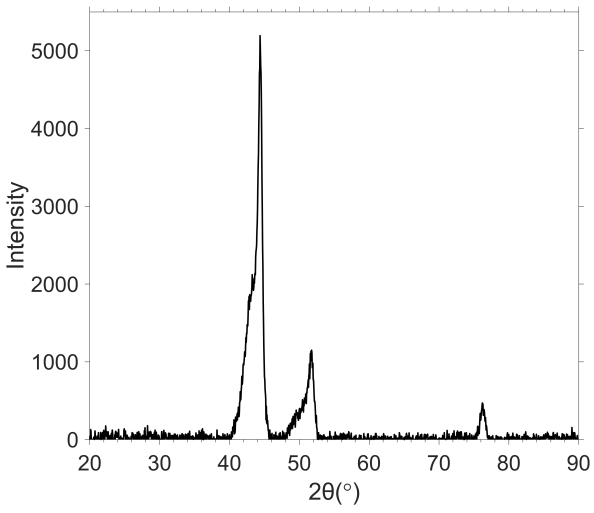

(b) XRD pattern for sample A−$IrNi_5$

Figure 44: XRD pattern for a) sample Ox−A−$IrNi_2$ and b)A−$IrNi_5$. showing the formation of the peak at 86.93° for A−$IrNi_5$.

Ida Wadseng

IrNix Core-Shell Nanocatalysts for the Oxygen Evolution Reaction

NTNU
Norwegian University of
Science and Technology